

Spring 2022

## MMS Observations of the Kelvin-Helmholtz Instability and Associated Ion Scale Waves

Rachel C. Rice  
RICER4@my.erau.edu

Follow this and additional works at: <https://commons.erau.edu/edt>



Part of the [Engineering Physics Commons](#), [Other Earth Sciences Commons](#), [Physical Processes Commons](#), [Plasma and Beam Physics Commons](#), and the [The Sun and the Solar System Commons](#)

---

### Scholarly Commons Citation

Rice, Rachel C., "MMS Observations of the Kelvin-Helmholtz Instability and Associated Ion Scale Waves" (2022). *PhD Dissertations and Master's Theses*. 651.  
<https://commons.erau.edu/edt/651>

This Dissertation - Open Access is brought to you for free and open access by Scholarly Commons. It has been accepted for inclusion in PhD Dissertations and Master's Theses by an authorized administrator of Scholarly Commons. For more information, please contact [commons@erau.edu](mailto:commons@erau.edu).

**MMS OBSERVATIONS OF THE  
KELVIN-HELMHOLTZ INSTABILITY AND  
ASSOCIATED ION SCALE WAVES**

By

Rachel C. Rice

A Dissertation

Submitted to the Department of Physical Sciences

in Partial Fulfillment of the Requirements

for the Degree of

**DOCTOR OF PHILOSOPHY in ENGINEERING PHYSICS**

April 2022

Embry-Riddle Aeronautical University

Daytona Beach, Florida

© Copyright by Rachel C. Rice 2022

All Rights Reserved

**MMS OBSERVATIONS OF THE KELVIN-HELMHOLTZ  
INSTABILITY AND ASSOCIATED ION SCALE WAVES**

By

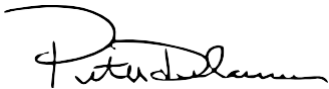
Rachel Christine Rice

This Dissertation was prepared under the direction of the candidate's Dissertation Committee Chair, Dr. Katariina Nykyri, and has been approved by the members of the Dissertation committee. It was submitted to the College of Arts and Sciences and was accepted in partial fulfillment of the requirements for the Degree of Doctor of Philosophy in Engineering Physics



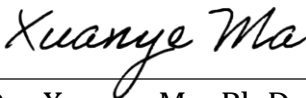
---

Dr. Katariina Nykyri, Ph.D.  
Committee Chair



---

Dr. Peter Delamere, Ph.D.  
Committee Member



---

Dr. Xuanye Ma, Ph.D.  
Committee Member

Edwin Mierkiewicz

Digitally signed by Edwin Mierkiewicz  
DN: cn=Edwin Mierkiewicz, o, ou,  
email=mierkiee@erau.edu, c=US  
Date: 2022.04.21 21:30:45 -05'00'

---

Dr. Edwin Mierkiewicz, Ph.D.  
Graduate Program Chair, Ph.  
D. Engineering Physics



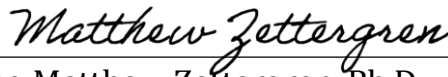
---

Dr. Karen Gaines, Ph.D.  
Dean, College of Arts and Sciences



---

Dr. Kshitija Deshpande, Ph.D.  
Committee Member



---

Dr. Matthew Zettergren, Ph.D.  
Committee Member



Digitally signed by Dr. John Hughes  
Date: 2022.04.22 08:10:31 -04'00'

---

Dr. John Hughes, Ph.D.  
Department Chair, Physical Sciences



---

Lon Moeller, J.D.  
Senior VP for Academic Affairs  
and Provost



## Acknowledgments

The work contained in this dissertation was funded by the National Science Foundation, under grant number 1707521. Additional support was provided by NASA under grants number NNZ17AI50G and NNX16AF89G. Thanks are owed to the entire MMS team, with special gratitude to the FPI, FGM, SCM, EDP, and HPCA instrument working groups. All MMS data is publicly available via the MMS Science Data Center, accessible at [lasp.colorado.edu/mms/sdc/public](http://lasp.colorado.edu/mms/sdc/public). Thanks also to the team at NASA Goddard's Space Physics Data Facility for maintaining the OMNI-Web database, which is accessible at [omniweb.gsfc.nasa.gov](http://omniweb.gsfc.nasa.gov).

## Personal Acknowledgments

First thanks must go to Dr. Katariina Nykyri, my adviser, for her enthusiasm for and guidance of my work. This dissertation is a product of her dedication as much as it is mine; it would not exist without her. An additional thank you to my dissertation committee for their time, encouragement, and insights.

I have been blessed throughout my academic career with many fantastic role models of curiosity and dedication to learning. Starting in second grade with Mrs. Adams, through high school with Ms. King, to undergrad with Dr. Berger, Dr. Waggoner, Dr. Spellerberg, Doc Feller, and Dr. Santos. Thank you for the unique and innumerable ways you've shaped my academic and personal journey to this point.

In addition to my teachers, I must thank my fellow students: the Mustangs of EMHS, everyone in Simpson's vanishingly small physics department, and the amazing GEM student community. You have been constant sources of inspiration and camaraderie. I wouldn't have stayed in school so long if y'all hadn't made it so much fun.

To my parents, thank you for so much more than I can say. I am lucky to be your daughter. You can put this on the shelf next to *Math is Everywhere*.

A final thank you to Brandon, for loving me in all the ways I need.

# Abstract

The detailed mechanisms coupling the solar wind to Earth's magnetosphere are not yet fully understood. Solar wind plasma is heated non-adiabatically as it penetrates the magnetosphere, and this process must span scale sizes. Reconnection alone is not able to account for the observed heating; other mechanisms must be at work. One potential process is the Kelvin-Helmholtz instability (KHI). The KHI is a convective instability which operates at the fluid scale in plasmas, but is capable of driving secondary process at smaller scales. Previous work has shown evidence of magnetic reconnection, various ion scale wave modes, mode conversion, and turbulence associated with the KHI, all of which can contribute to heating and/or plasma transport across the magnetopause boundary.

The launch of the Magnetosphere Multiscale (MMS) mission in 2015 offered a new opportunity to study secondary processes associated with the KHI down to the electron scale. The MMS mission's goal was to study the microphysics of magnetic reconnection at the dayside magnetopause and in the magnetotail. It comprises 4 identical spacecraft, which fly in formation and are equipped with the highest resolution instrumentation available. MMS is the first mission capable of resolving electron scale processes due to its combination of high temporal resolution instrumentation

and its record breaking spacecraft separation. The work presented in this dissertation focuses on the fluid and ion scale behavior of the KHI as a proof of concept for the techniques used. Future work will apply these methods to smaller scales to fully take advantage of MMS's capabilities.

This work uses MMS observations of 45 KHI events between September 2015 and March 2020 to determine the influence of the KHI on magnetosphere dynamics and solar wind-magnetosphere coupling. The observed events are well distributed along the magnetopause, and occur for the full range of solar wind conditions and IMF orientations. The KHI growth rates and the percent of the solid angle unstable to the development of the KHI (which we term the unstable solid angle) are not effected by the solar wind conditions or IMF strength. The observed KHI grow more quickly and in more unstable regions the farther downtail they occur.

Ion scale wave intervals observed within the KHI are consistent with the ion cyclotron, kinetic Alfvén, and kinetic magnetosonic wave modes, all of which can contribute to enhanced ion heating across the magnetopause. These ion scale wave intervals are compared with observations made when the KHI is not active. The KHI is associated with strong increases in quasi-perpendicular (quasi-parallel) ion scale wave activity in the magnetosphere (magnetosheath), consistent with previous studies of data from the Cluster spacecraft. Observations show electron beta is decreased and ion temperature anisotropy is increased in the magnetosheath when the KHI is present, which can help explain a KHI associated increase in quasi-parallel wave activity in the sheath. Additionally, parallel velocity shears are increased when the KHI is active, which may further drive wave activity in all regions.

Ion scale wave intervals show enhanced Poynting flux in all regions and at all wave

angles when the KHI is active, suggesting more energy is available to drive ion heating during the KHI. Increased Poynting flux is also well correlated with larger changes in energy during KH associated ion scale waves. The rate of heating, described by the characteristic heating frequency, also increases for ion scale waves associated with the KHI. These findings suggest that plasma heating is both increased and more efficient in the presence of the KHI.

# Contents

<b>Abstract</b>	<b>vi</b>
<b>List of Figures</b>	<b>xi</b>
<b>List of Tables</b>	<b>xix</b>
<b>1 Introduction</b>	<b>1</b>
1.1 The Plasma State . . . . .	1
1.2 The Sun Earth System . . . . .	4
1.3 The Kelvin-Helmholtz Instability . . . . .	14
1.4 The Magnetosphere Multiscale Mission . . . . .	18
1.5 Motivation . . . . .	21
<b>2 Research Methodology</b>	<b>22</b>
2.1 Data . . . . .	22
2.1.1 MMS Instrumentation and Data Products . . . . .	22
2.1.2 Upstream Solar Wind Observations . . . . .	25
2.2 Data Analysis . . . . .	25
2.2.1 KHI Analysis Tools . . . . .	25
2.2.2 Kinetic Scale Wave Analysis Tools . . . . .	51
2.3 MHD Simulations . . . . .	59
2.4 Conclusions . . . . .	66
<b>3 Statistical Results of KHI Properties</b>	<b>67</b>
3.1 KHI Growth Rates and Unstable Solid Angles . . . . .	67

3.2	Solar Wind and IMF During the KHI . . . . .	71
3.3	KHI Observation Locations . . . . .	76
3.4	Conclusions . . . . .	78
<b>4</b>	<b>Ion Scale Waves within the KHI</b>	<b>83</b>
4.1	Expected Wave Modes . . . . .	83
4.1.1	Ion Cyclotron Waves . . . . .	84
4.1.2	Kinetic Alfvén Waves . . . . .	85
4.1.3	Magnetosonic Waves . . . . .	86
4.2	Example Interval . . . . .	87
4.3	Comparison of KHI and non-KH Observations . . . . .	93
4.4	Statistical Results . . . . .	95
4.4.1	Wave Angle and Ellipticity . . . . .	96
4.4.2	Mean $\delta E/\delta B$ Ratio . . . . .	99
4.4.3	Mean Total Power . . . . .	101
4.4.4	Integrated Poynting Flux . . . . .	102
4.4.5	Characteristic Heating Frequency . . . . .	104
4.4.6	Energy Analysis . . . . .	107
4.4.7	Mean Temperature Anisotropy . . . . .	110
4.4.8	Mean Electron Beta . . . . .	110
4.4.9	Maximum Parallel Velocity Shear . . . . .	113
4.5	Conclusions . . . . .	115
<b>5</b>	<b>Summary and Discussion</b>	<b>118</b>
5.1	Summary . . . . .	118
5.2	Discussion . . . . .	121
5.3	Ongoing and Future Work . . . . .	123
<b>A</b>	<b>Solar Wind Conditions</b>	<b>127</b>
<b>B</b>	<b>Non-KH Observation Details</b>	<b>133</b>
	<b>Bibliography</b>	<b>135</b>

# List of Figures

1.1	Different processes in plasma happen at different scales. Fluid or MHD scale processes occur over a long time and cover large distances, while kinetic scale processes happen quickly and over smaller amounts of space. Image from <i>Nykyri et al.</i> [2021a]. . . . .	3
1.2	The Sun as seen in extreme ultraviolet light (left) and visible light (top right). Visible sunspots develop near active regions in the solar magnetic field (bottom right). Images from NASA’s Solar and Heliospheric Observatory (SOHO). . . . .	5
1.3	The density and velocity of the solar wind which impacts Earth is highly dependent upon processes on the solar surface. In this ENLIL model from NOAA’s Space Weather Prediction Center, a high density, high velocity region is about to impact Earth. . . . .	6
1.4	Schematic illustration of the magnetosphere and current systems from <i>Pollock et al.</i> [2003]. . . . .	8
1.5	Magnetic reconnection is the explosive realignment of magnetic field lines, often from antiparallel to more efficient configurations. The small scale physics driving reconnection remains an open question. . . . .	11



1.6 The basic geometry of reconnection (a) includes inflow regions, the ion (and electron) diffusion region(s), and the exhaust regions where plasma is expelled. The inclusion of Hall currents in the diffusion region (b) was a major break through for reconnection theory. Image from *Burch et al.* [2016]. . . . . 13

1.7 The KHI develops at regions with large velocity shears (red arrows). As the vortex develops, the magnetic field (white lines) will be twisted and compressed, and plasmas with different densities (colorscale) on either side of the boundary can be mixed. . . . . 15

1.8 Magnetic reconnection within a KH vortex, as depicted in *Nykyri and Otto* [2001], leads to plasma heating and transport from the magnetosheath to the magnetosphere. . . . . 17

1.9 MMS orbits for Phase 1 (left), targeting the dayside magnetopause, and Phase 2 (right), targeting tail reconnection, from *Burch et al.* [2016]. Both orbits provide ample opportunity to observe the KHI developing on the flank magnetopause. . . . . 20

2.1 MMS observations of the KHI from 16:35 to 19:07 UT on 26 September 2017. . . . . 29

2.2 Sorting parameters which are expected to be large in the magnetosheath ( $n/T$ ,  $nv_x$ ,  $nv_{tail}/T$ , and  $v_{tail}/S$ ) provide reasonable density results. Parameters which are expected to be small in the magnetosheath ( $S$  and  $S/v_{tail}$ ) yield densities much lower than expected. Overly restrictive and overly relaxed cutoff values can negatively effect results. Sorting parameters are less sensitive to the percent of data used to determine the magnetopause value. . . . . 41

2.3 Sorting parameters which are expected to be large in the magnetosphere ( $S$  and  $S/v_{tail}$ ) produce reasonable density results. Parameters which are expected to be small in the magnetosphere ( $n/T$ ,  $nv_x$ ,  $nv_{tail}/T$ , and  $v_{tail}/S$ ) yield densities much higher than expected. Overly restrictive and overly relaxed cutoff values can negatively effect results. Sorting parameters are less sensitive to the percent of data used to determine the magnetopause value . . . . . 42

2.4 The sorting parameters,  $S$  and  $nv_{tail}/T$  are shown as a time series for the example event on 26 September 2017. Any plasma with  $S$  or  $nv_{tail}/T$  above the cutoff value (colored lines) is sorted in the magnetosphere or magnetosheath, respectively. The results of the automated region sorting method are in good agreement with expectations based on the omnidirectional ion energy and ion density and temperature. . . 44

2.5 A region sorting technique from *Moore et al.* [2017] uses weighted averages of the ion energy to identify magnetospheric, mixed, and magnetosheath regions. Results are in general agreement with the omnidirectional ion energy and ion density and temperature, but identify less mixed plasma than the newly developed method. . . . . 46

2.6 On 26 September 2016, MMS observed the KHI while skimming the magnetopause boundary (bottom). Solar wind density (top) suggests a magnetosheath density  $\approx 30$  /cc, which is only observed at the end of the interval. The new region sorting method developed here selects only the pure sheath, where density  $\approx 30$  /cc, while the method used in *Moore et al.* [2017] includes mixed plasma earlier in the interval (right). 47

2.7 The unstable solid angle is the fraction of the total  $4\pi$  solid angle sphere which can support the growth of the KHI. The directions in which the KHI is able to grow are shown in blue for the September 26 2017 event. 52

2.8 The total magnetic field, ion cyclotron frequency, and filtered wave magnetic field for the example event on 26 September 2017. Dashed lines indicate the upper and lower boundaries of the band pass filter used to isolate the wave field. . . . . 55

2.9 The automated region sorting method yields regions in which measured density (red, dashed lines) agrees well with the known value (black, solid lines) even as the simulations develop and the plasma is mixed. . 64

2.10	The results of the automated region sorting method depend on cut geometry in simulation space. Cuts which spend significant portions of the event on both sides of the boundary produce the best results. The known density value for each region is indicated by the solid black line, the measured densities are indicated by dashed lines with colors corresponding to the cut geometries shown on the right. . . . .	65
3.1	The normalized distributions of IMF strength and normalized IMF components for KHI observations (red) and the full 4.5 year interval from September 2015 to March 2020 (black) are similar, though the KHI occurs more frequently when the $B_Z$ component is positive. . . .	72
3.2	Normalized distributions of solar wind density, temperature, flow speed, and Alfvén Mach number for KHI observations (red) and the full 4.5 year interval from September 2015 to March 2020 (black) are generally similar, though the KHI observations overrepresent solar wind speeds between 350 and 450 km/s. . . . .	74
3.3	KHI growth rate (top), unitless growth rate (middle), and unstable solid angle (bottom) as functions of solar wind density (far left), temperature (center left), flow speed (center), Alfvén Mach number (center right), and IMF magnitude (far right). There is no obvious correlation between KH characteristics and solar wind conditions . . . . .	75

3.4	KHI growth rate (top), unitless growth rate (middle), and unstable solid angle (bottom) with respect to the KHI's observation location in the GSM $X$ - $Y$ (left), $X$ - $Z$ (center), and $Y$ - $Z$ (right) planes. KH events occurring farther downtail tend to grow faster and in less stable regions. . . . .	77
4.1	The trace of perpendicular components (see Section 2.2.2) of the wave field observed from 16:43:03 (green circle) to 16:43:06 (red square) on 26 September 2017. The wave field is right-handed polarized with respect to the background magnetic field (into the page) and propagates quasi-perpendicularly ( $\theta_{kB} = 122^\circ$ ) to the background field. . . . .	89
4.2	The ion distribution function from the FPI instrument aboard MMS1 during the example wave interval is very slightly anisotropic ( $T_\perp/T_\parallel = 1.06$ ). The cold ions are shifted slightly in the negative $B_\parallel$ direction while the hotter ions are more cigar shaped. . . . .	91
4.3	The $H^+$ ion distribution function from the HPCA instrument aboard MMS1 during the example wave interval shows some evidence of shells in the cold ions which could drive a KM wave. . . . .	92
4.4	MMS observations of a quiet magnetopause crossing from 16:00 to 18:00 UT on 01 November 2018 in which no signatures of the KHI were observed. . . . .	94

4.5	The region sorting parameters, $S$ and $nv_{tail}/T$ , automatically sorted regions, omnidirectional ion energy, and ion density and temperature for the example KHI event on 26 September 2017 (left) and the example quiet crossing on 01 November 2018 (right). As expected, the quiet crossing contains much less mixed plasma than the KH event. . . . .	96
4.6	Normalized histograms of wave angle and ellipticity in the magnetosphere (left), mixed region (center), and magnetosheath (right) for KHI (top) and non-KH (bottom) observations. . . . .	97
4.7	Normalized difference histograms comparing mean electric to magnetic wave field ratio and wave angle for the KHI and non-KHI observations in the magnetosphere (top), mixed region (middle), and magnetosheath (bottom). . . . .	100
4.8	Normalized difference histograms comparing mean total wave power and wave angle for the KHI and non-KHI observations in the magnetosphere (top), mixed region (middle), and magnetosheath (bottom). . . . .	101
4.9	Normalized difference histograms comparing integrated total Poynting flux and wave angle for the KHI and non-KHI observations in the magnetosphere (top), mixed region (middle), and magnetosheath (bottom). . . . .	103
4.10	Normalized difference histograms comparing the median characteristic heating frequency and wave angle for the KHI and non-KHI observations in the magnetosphere (top), mixed region (middle), and magnetosheath (bottom). Due to data outages on MMS3 and MMS4, the heating frequency is only available for 28 of the 45 KHI observations and 22 of the 33 non-KH observations. . . . .	106

4.11	Normalized difference histograms comparing the change in average energy across wave intervals and the wave angle for the KHI and non-KHI observations in the magnetosphere (top), mixed region (middle), and magnetosheath (bottom). . . . .	108
4.12	Normalized difference histograms comparing the change in average energy across wave intervals and the total integrated Poynting flux for the KHI and non-KHI observations in the magnetosphere (top), mixed region (middle), and magnetosheath (bottom). . . . .	109
4.13	Normalized difference histograms comparing mean temperature anisotropy, $T_{\perp}/T_{\parallel}$ , and wave angle for the KHI and non-KHI observations in the magnetosphere (top), mixed region (middle), and magnetosheath (bottom). . . . .	111
4.14	Normalized difference histograms comparing mean electron beta, $\beta_e$ , and wave angle for the KHI and non-KHI observations in the magnetosphere (top), mixed region (middle), and magnetosheath (bottom). . . . .	112
4.15	Normalized difference histograms comparing the difference in parallel velocity from MMS1 to MMS2 (left), MMS3 (center), and MMS4 (right) and wave angle for the KHI and non-KH observations in the magnetosphere (top), mixed region (middle), and magnetosheath (bottom). Ion velocity data is not available from MMS3 for 3 (1) KHI (non-KH) events. The MMS1-MMS3 results shown include only the 42 (32) events for which data is available. . . . .	114

5.1 The total magnetic and electric fields, the lower hybrid frequency and band pass filter cutoff frequencies, and the filtered magnetic and electric fields show a clear wave packet around the lower hybrid frequency between 17:54 and 17:55 UT on 26 September 2017. . . . . 126



# List of Tables

2.1	The MMS instruments used in this study, along with their operational modes and observational cadences. . . . .	24
2.2	The date, onset time, duration, GSM location, and estimated wavelength of the 45 KHI events observed by MMS from September 2015 to March 2020. Burst mode data is available for portions of all events.	31
2.3	A summary of the sorting parameters developed here and their relative values in each region. . . . .	38
2.4	Normalization constants for the 2D MHD simulations. . . . .	62
3.1	Growth rates (GR), unitless growth rates (UGR), unstable solid angles (USA), and the relative value of the maximum normal velocity component for each of the 45 KHI events observed by MMS from September 2015 to March 2020. . . . .	68
4.1	Characteristic behavior of the electrostatic and electromagnetic ion cyclotron, kinetic Alfvén, and magnetosonic wave modes. . . . .	87

A.1	The onset IMF orientation and magnitude and average IMF orientation and magnitude of the 45 KHI events observed by MMS from September 2015 to March 2020. OMNI data is not available for the event on 03 June 2019 (event no. 37). . . . .	128
A.2	The average solar wind density, temperature, flow speed and Alfvén mach number during 45 KHI events observed by MMS from September 2015 to March 2020. OMNI data is not available for the event on 03 June 2019 (event no. 37). . . . .	130
B.1	The date, onset time, duration, and GSM location of 33 quiet magnetopause crossings observed by MMS from September 2015 to March 2020. . . . .	134

# Chapter 1

## Introduction

### 1.1 The Plasma State

Despite what science fiction authors would have you believe, space is not a vacuum. The vast distances between planets, stars, and galaxies is filled with plasma. Plasma is a fourth state of matter, often ignored in elementary science classes. In the same way that energy may be added to a solid to melt it to a liquid, energy added to a gas may separate electrons from their atomic nuclei to create a plasma. The free ions and electrons are responsive to electric and magnetic fields, giving rise to unique processes which define the plasma state.

Consider an example: a positive test charge in a vacuum creates an electric potential, which decays with distance. If the same positive charge were placed in a plasma, the electrons of the plasma would be attracted to it, and the positive particles in the plasma would be repelled. The movement of charge particles within the plasma would shield the test charge, and the observed potential would decay exponentially,

rather than as the inverse of distance. This change in the observed electric effect of a test charge is just one of the collective effects defining the plasma state.

In the presence of a magnetic field, charged particles in plasma are subject to several types of motion. A single particle in a constant magnetic field is subject to the Lorentz force and will gyrate about the field lines. In the case of a magnetic field gradient, the particle will bounce between regions of high field strength. Curvature in the magnetic field causes particles to drift perpendicularly to the field lines. The time and spatial scales of any of these movements is dependent upon the mass of the particles within the plasma. In the case of a fully ionized plasma made up of protons and electrons, the much more massive protons will move more slowly and cover much larger distances than the less massive electrons. The different masses of particles within a plasma give rise to different scale sizes, in this case the ion and electron scales.

Scales defined by the movements of single particles are often referred to as kinetic scales. If we now zoom out from single particles to treat the whole plasma like a fluid, as is the case in magnetohydrodynamics (MHD), a much larger scale becomes apparent: the fluid scale. Figure 1.1 demonstrates the different scale sizes common in space plasmas. Physical processes across all plasma scale sizes play an important role in the movement of mass and energy throughout our solar system, and indeed our universe. The work in this dissertation will focus on the physics of space plasmas near Earth and the ability of different physical processes to drive heating and energization across scale sizes.

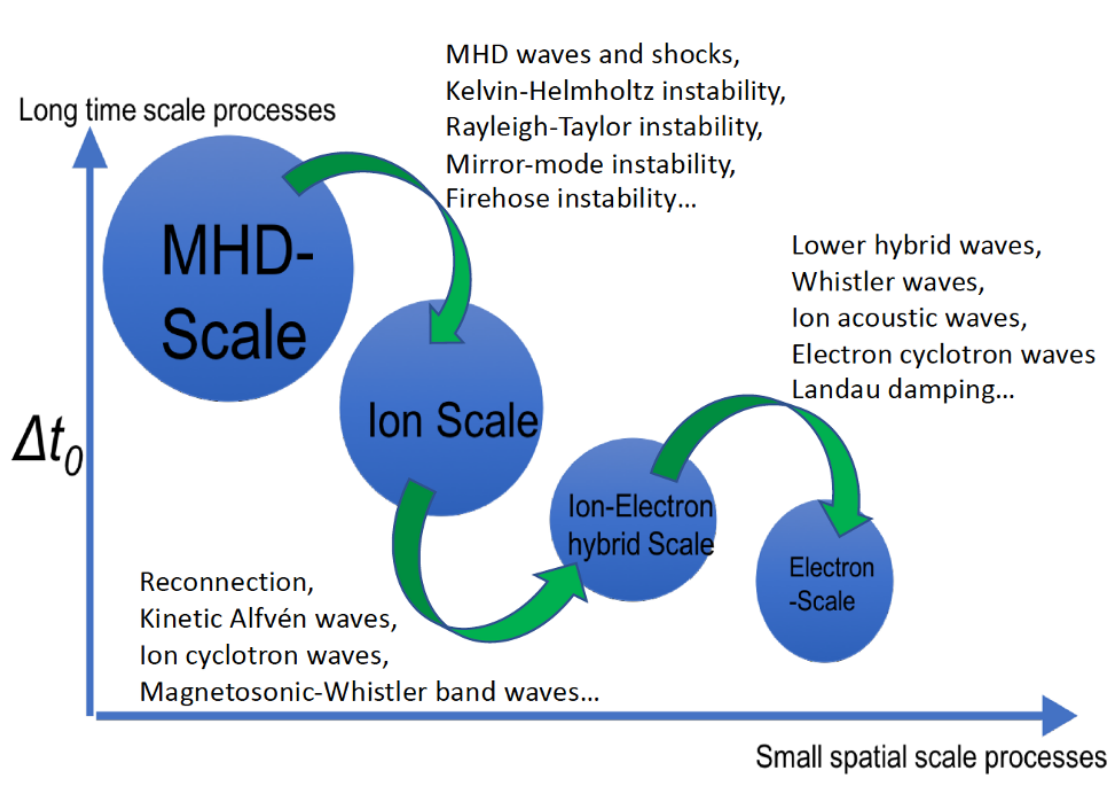


Figure 1.1: Different processes in plasma happen at different scales. Fluid or MHD scale processes occur over a long time and cover large distances, while kinetic scale processes happen quickly and over smaller amounts of space. Image from *Nykyri et al.* [2021a].

## 1.2 The Sun Earth System

Most fourth graders encountering their first lesson of biology will tell you that the sun is the source of all life on Earth. Plants use energy from the sun to grow, animals eat the plants, and so on up the food chain. At the most basic level, the sun is *the* source in biology. This is also true in space plasma physics: the Sun is the driving source of all the phenomena we study.

### The Sun and Solar Wind

As observed by the naked eye, the sun is a boring, albeit, bright blob in the sky. But with just a little assistance, we discover the sun is much more dynamic than our eyes would have us believe. Galileo recorded his observations of dark spots on the sun's surface in the 17th century using his newly invented telescope [*Sakurai*, 1980]. However, Galileo was not the first scientist to observe such sunspots. There is strong evidence of sunspot observations made in the 9th century C.E., with some scholars speculating that sunspots were observed as early as the 5th century B.C.E. [*Sarton*, 1947; *Bicknell*, 1968]. Sunspots are visible evidence of the sun's magnetic field. The solar dynamo drives a complex field, which is further complicated by the sun's differential rotation. The equator of the sun completes a full rotation in about 27 days, while its poles take roughly 31 days to complete a rotation. As field lines are twisted, active regions develop, and are visible as sunspots, as shown in Figure 1.2. These active regions can produce solar flares and coronal mass ejections which release large amounts of mass and energy into the interplanetary space.

In addition to acute processes like flares, the sun is also constantly ejecting plasma in the form of the solar wind. The solar wind is a low density plasma made up

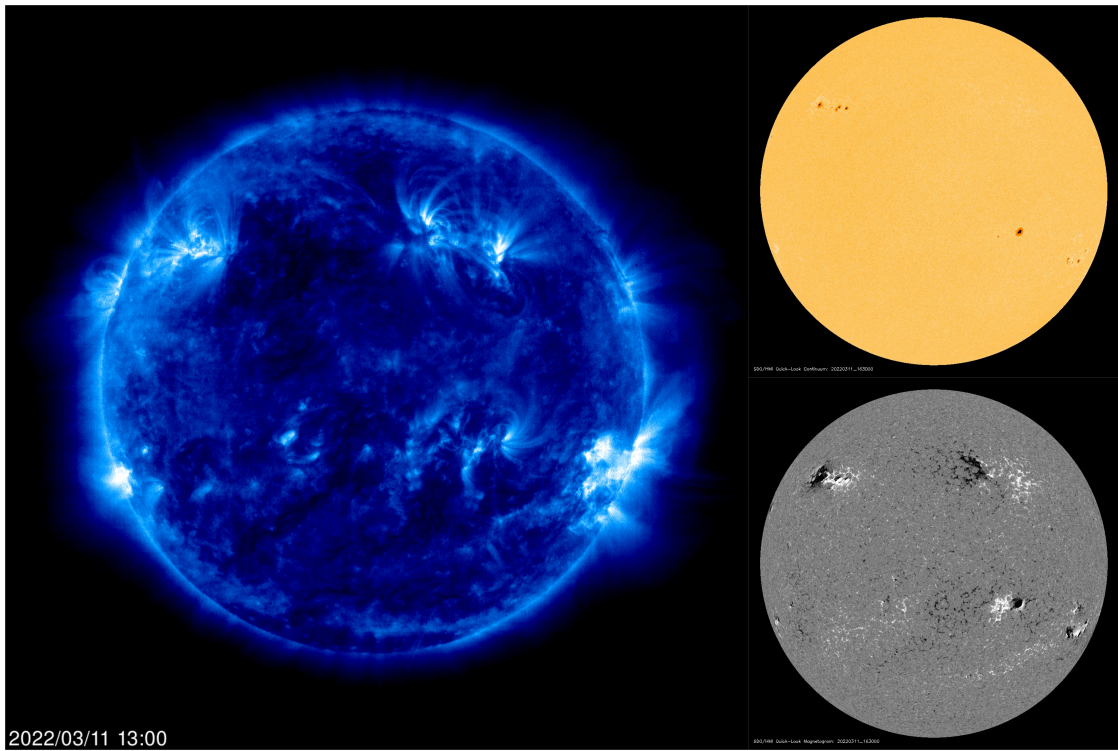


Figure 1.2: The Sun as seen in extreme ultraviolet light (left) and visible light (top right). Visible sunspots develop near active regions in the solar magnetic field (bottom right). Images from NASA's Solar and Heliospheric Observatory (SOHO).

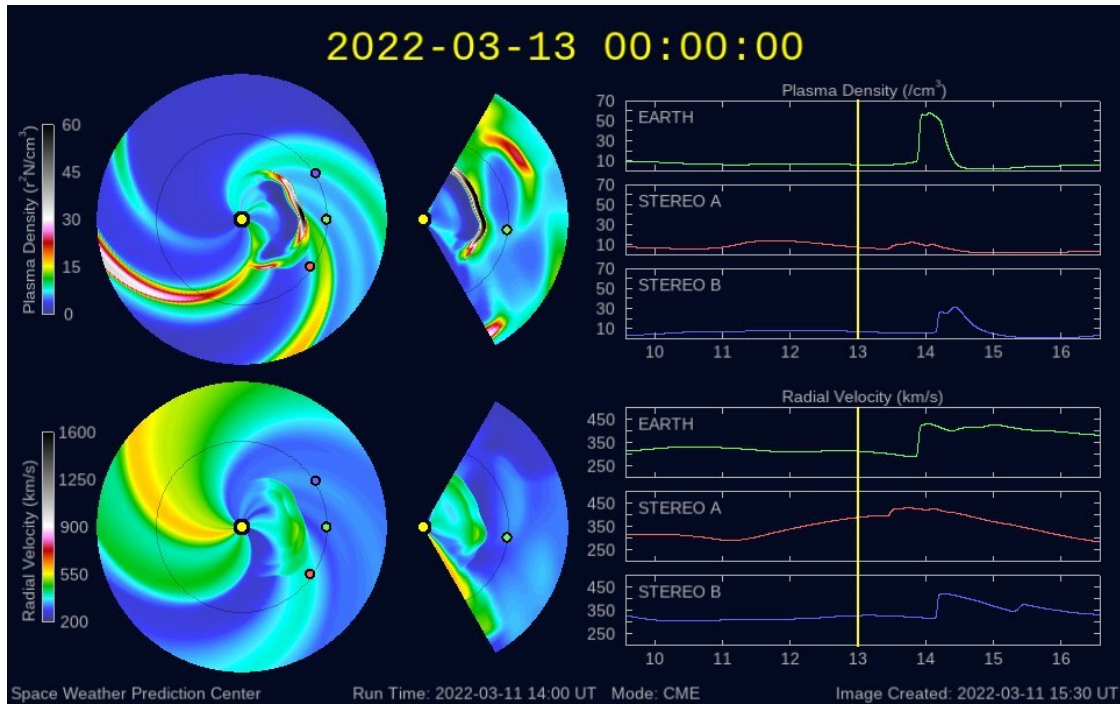


Figure 1.3: The density and velocity of the solar wind which impacts Earth is highly dependent upon processes on the solar surface. In this ENLIL model from NOAA’s Space Weather Prediction Center, a high density, high velocity region is about to impact Earth.

protons, electrons, and the occasional alpha particle. Due to the solar wind plasma’s high electrical conductivity, the solar magnetic field is “frozen” into the plasma as it leaves the sun and is carried to the edge of our solar system. The solar wind and its embedded magnetic field, called the interplanetary magnetic field, were first hypothesized by Eugene Parker [*Parker*, 1958]. The solar wind is constantly flowing, but its speed, density, and the strength and orientation of the embedded field are ever changing. Transient events on the solar surface, such as flares and coronal mass ejections can dramatically affect the solar wind that makes its way to Earth.

Embedded within the solar wind plasma is the interplanetary field (IMF). As solar



wind plasma flows radially away from the sun, high electrical conductivity “freezes” the magnetic field into the plasma while still maintaining a magnetic foot print on the rotating sun. In the simplest models, this results in an Archimedean spiral, known as the “Parker Spiral.” The simple model is, of course, not reality, and the IMF may actually take any orientation. At Earth, we observe the IMF and solar wind conditions with a suite of spacecraft at the L1 Lagrange point between the sun and Earth. IMF is often reported in geocentric solar magnetic (GSM) coordinates. In this coordinate system, the origin is at Earth’s center and the  $X$ -axis points towards the sun. The  $Z$ -axis points north along Earth’s magnetic axis. The  $Y$ -axis completes the right-handed system. IMF orientation is usually described as Parker Spiral ( $B_X$  and  $B_Y$  dominate with opposite signs), ortho-Parker Spiral ( $B_X$  and  $B_Y$  dominate with the same sign), northward (strong positive  $B_Z$ ), southward (strong negative  $B_Z$ ), radial ( $B_X$  dominates), duskward (strong positive  $B_Y$ ), or dawnward (strong negative  $B_Y$ ).

## **Earth’s Magnetosphere**

Earth is protected from the onslaught of the solar wind and IMF by its own magnetic field. Earth’s internal dynamo generates a near dipolar field, similar to a common bar magnet, that forms a bubble of protection called the magnetosphere. As the solar wind flows around the magnetosphere, the dayside closest to the sun is compressed and the nightside is stretched to form a long tail. Thus Earth’s magnetosphere more closely resembles a jellyfish than the typical dipole field. Contained within the magnetosphere is a mostly independent system of magnetized plasma and currents, as can be seen in Figure 1.4. At the boundary of the magnetosphere, called the mag-

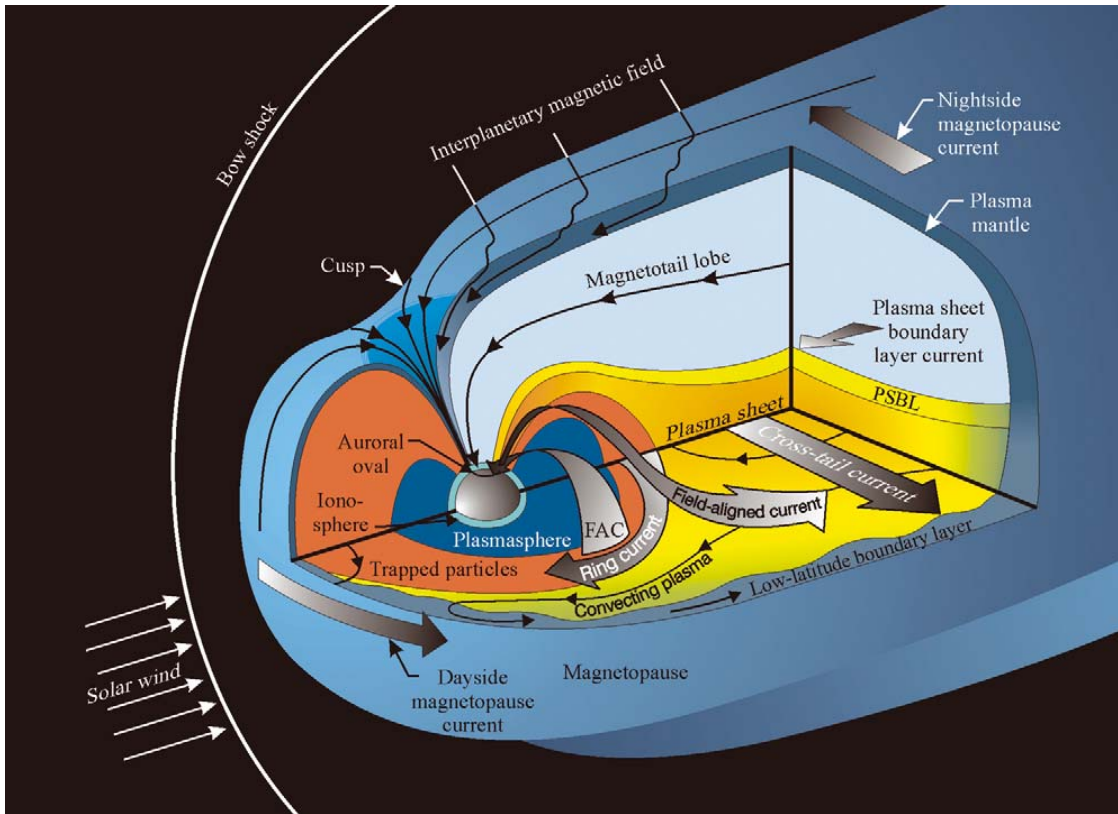


Figure 1.4: Schematic illustration of the magnetosphere and current systems from *Pollock et al.* [2003].

netopause, a variety of physical processes operate to couple the solar wind to the magnetosphere.

The solar wind flows super-Alfvénically: it moves forward faster than information about upcoming obstacles can travel back. Much like an airplane traveling supersonically, this results in shock waves around obstacles. At the Earth, this is known as the bow shock. Just inside the bow shock is a layer of shocked solar wind known as the magnetosheath. Plasma within the magnetosheath is typically colder and denser than the plasma within the magnetosphere. Though the solar wind is slowed immediately after the bow shock, it re-accelerates as it flows around Earth. Thus the

plasma in the flank and tail magnetosheath flows much faster than plasma within the magnetosphere.

The magnetosphere is not a single homogeneous region. Just inside the magnetopause is the low-latitude boundary layer (LLBL). The LLBL is essentially a transition region where plasma parameters change from magnetosheath values, to values in line with the inner magnetosphere. The properties of the LLBL vary with location and IMF conditions. The LLBL is thinner on the dayside magnetosphere than in the tail, and, as the name suggests, is most prominent at low latitudes near the equator [*Eastman and Hones Jr, 1979*].

The magnetotail is separated into northern and southern lobes by the plasma sheet which contains the cross tail current. The plasma sheet is much hotter and more tenuous than the magnetosheath and LLBL, but not uniformly so. Observations from Defense Meteorological Satellite Program (DMSP) and Time History of Events and Macroscale Interactions during Substorm (THEMIS) spacecraft have established that the cold component ions of the plasma sheet are 30-40% hotter in the dawn flank than in the dusk [*Hasegawa et al., 2003; Wing et al., 2005; Dimmock et al., 2015*]. *Dimmock et al. [2015]* conducted a statistical study of the magnetosheath source population as observed by THEMIS spacecraft over seven years which showed ions in the dawn flank are on average 10% hotter than those in the dusk flank. This asymmetry is more pronounced under fast ( $> 400$  km/s) solar wind conditions [*Dimmock et al., 2015*]. However, even for fast solar wind, the asymmetry of the magnetosheath source plasma is insufficient to produce the observed asymmetry in the plasma sheet. MHD simulations are unable to reproduce the observed sheath asymmetry, but it is apparent in hybrid models, suggesting a kinetic scale mechanism

is responsible for asymmetrically driving the heating of cold component ions in the sheath and farther into the magnetosphere [Dimmock *et al.*, 2015]. The exact nature of mechanism has not yet been determined.

## **Solar Wind - Magnetosphere Coupling**

The coupling of the solar wind to Earth’s magnetosphere and its impacts on local space weather are a fundamental question of space physics. Several mechanisms operating at the magnetopause boundary, such as magnetic reconnection [Paschmann *et al.*, 1979; Sonnerup *et al.*, 1981; Gosling *et al.*, 1986; Burch and Phan, 2016] and viscous interactions [Axford and Hines, 1961; Otto and Fairfield, 2000; Fairfield *et al.*, 2000], are responsible for the transfer of mass and energy from the solar wind to the magnetosphere. Understanding the detailed effects of these processes is vital to predict and help prevent negative outcomes from space weather.

In the most simplistic model of magnetic reconnection, antiparallel magnetic field lines very near each other break and reconnect in an explosive process in which energy previously stored in the field is converted to kinetic and thermal energy in the plasma. Figure 1.5 depicts antiparallel field lines before, during, and after reconnection occurs. In practice, magnetic fields in space plasmas are usually not strictly antiparallel. Reconnection occurring for non-antiparallel fields is known as component or guide field reconnection.

We typically assume the magnetic field is “frozen” into the plasma as a result of high conductivity. However this frozen in condition must be violated for reconnection to occur. Historically, several models have been developed which explain how the frozen in condition is violated, and each describes a different “type” of reconnection.

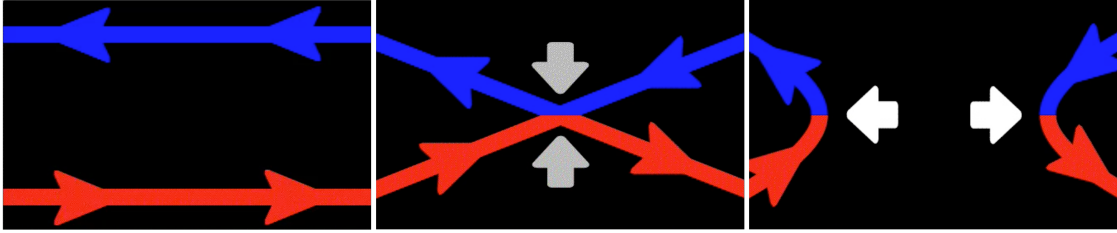


Figure 1.5: Magnetic reconnection is the explosive realignment of magnetic field lines, often from antiparallel to more efficient configurations. The small scale physics driving reconnection remains an open question.

The first, Sweet reconnection, relies on resistivity to break the frozen in condition [Sweet, 1958]. As regions of oppositely directed fields collide, a thin current sheet forms between them. Resistivity in the current sheet dissipates the magnetic field and plasma is ejected through long, thin exhaust regions. Sweet reconnection has been observed in laboratory plasmas, but proceeds too slowly to explain observations of reconnection in space plasmas [Burch and Drake, 2009].

In order to increase the speed of reconnection, Parker [1957] proposed an addendum to Sweet type reconnection. Sweet-Parker reconnection includes strong magnetic field gradients in the exhaust regions which result in faster plasma expulsion [Parker, 1957]. While Sweet-Parker reconnection is faster than Sweet reconnection, it is still not fast enough to explain observations in space plasmas [Burch and Drake, 2009].

In 1964 Petschek [1964] proposed the presence of Alfvén waves leading to shocks at the edges of the exhaust region. Such shocks shorten the exhaust region, and because plasma does not travel as far, the reconnection rate is increased. The presence of waves also helps dissipate the magnetic field faster than resistivity alone [Burch and Drake, 2009]. The Petschek model explains most observations of reconnection in space plasmas, but the expected shocks are not commonly observed [Drake et al.,

2009; *Burch et al.*, 2016].

The final major development in reconnection theory was the recognition that ions and electrons are decoupled from the magnetic field at different points [*Biskamp et al.*, 1995; *Burch et al.*, 2016]. Massive ions, with their larger inertia, are decoupled from the magnetic field before electrons. While the electrons are still bound to the field without ions, Hall currents will develop perpendicular to the reconnecting fields, as shown in Figure 1.6. Such currents help to dissipate the magnetic field at the reconnection site [*Biskamp et al.*, 1995; *Burch et al.*, 2016].

While the exact mechanisms which violate the frozen in condition and trigger reconnection are still debated, the effects of reconnection are well understood: energy stored in the magnetic field is converted rapidly to kinetic energy of the ions and electrons. This is often observed in the form of reconnection jets and crescent shaped distribution functions. Reconnection also allows for mass transport from one region to another. This is particularly important for coupling the solar wind to Earth's magnetosphere and convection within the magnetosphere.

The Dungey cycle, as described by *Dungey* [1961], consists of reconnection at the subsolar magnetopause and in the magnetotail. When the IMF is in a southward orientation, mostly antiparallel to Earth's steady northward field, reconnection occurs near the subsolar point. This results in Earth's magnetic field lines being dragged tailward with the solar wind and a more diffuse boundary region. This causes a buildup of flux in and around the magnetotail, triggering reconnection. Tail reconnection then drives the convection of flux back to the dayside magnetosphere.

The location of reconnection on the dayside magnetopause is highly dependent on the orientation of the IMF. In the case of primarily southward IMF, which is

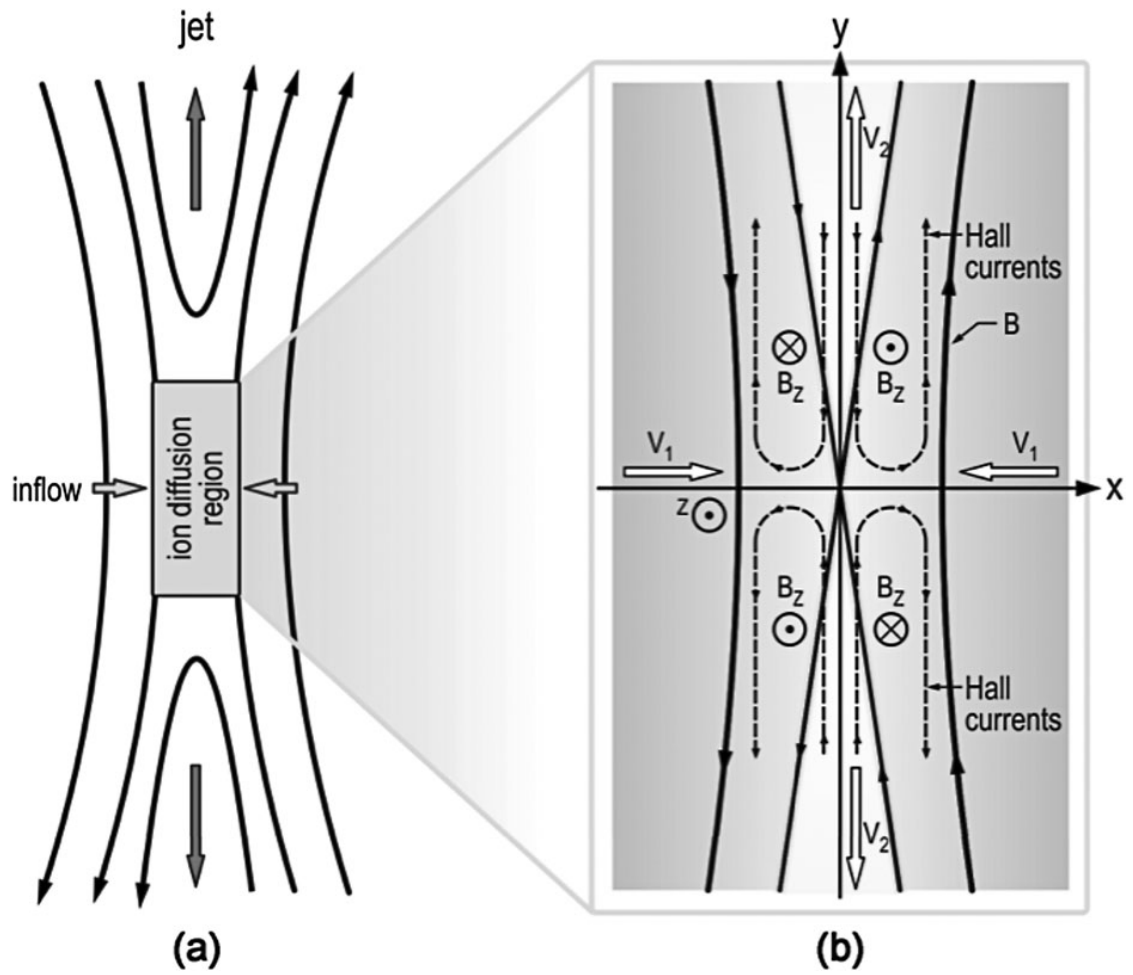


Figure 1.6: The basic geometry of reconnection (a) includes inflow regions, the ion (and electron) diffusion region(s), and the exhaust regions where plasma is expelled. The inclusion of Hall currents in the diffusion region (b) was a major breakthrough for reconnection theory. Image from *Burch et al.* [2016].

antiparallel to the magnetosphere's steady northward field, reconnection will occur at the subsolar point. Additionally, high latitude reconnection at the cusps of the magnetosphere can occur for all IMF orientations. In any case, it is also important to remember the IMF is never purely in a single orientation, and thus reconnection between the solar wind and magnetosphere will often be component reconnection influenced by a guide field.

There are other processes at work at the magnetopause in addition to reconnection. Many transient processes, such as surface waves and foreshock bubbles, are active at the magnetopause boundary. The work presented in this dissertation will focus on just one of these transient processes: the Kelvin-Helmholtz Instability.

### 1.3 The Kelvin-Helmholtz Instability

The Kelvin-Helmholtz Instability (KHI), as first described in the mid 19th century by Kelvin [*Kelvin and Thomson*, 1871] and Helmholtz [*Helmholtz*, 1868], is a convective instability occurring in regions of large shear flow. A small perturbation at the interface of two differentially flowing fluids is acted upon asymmetrically on either side of the boundary. Free energy within the shear flow drives the growth of the instability, as can be seen in Figure 1.7. The KHI may be observed in clouds, river confluences, or even as cream is poured into a cup of coffee. Normal, non-magnetized fluids are unstable to the development of the KHI at any shear flow boundary [*Chandrasekhar*, 1961]. The development of the KHI is not so simple, however, in magnetized fluids like space plasmas.

The KHI occurs in regions of large shear flow [*Chandrasekhar*, 1961], such as the



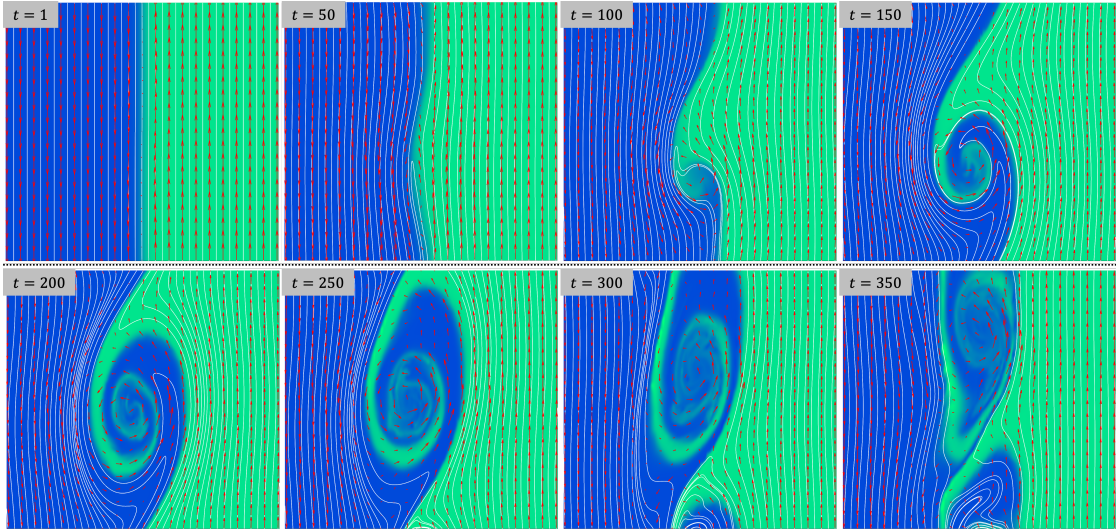


Figure 1.7: The KHI develops at regions with large velocity shears (red arrows). As the vortex develops, the magnetic field (white lines) will be twisted and compressed, and plasmas with different densities (colorscale) on either side of the boundary can be mixed.

boundary between magnetosheath plasma flowing with the shocked solar wind and the relatively stagnant magnetosphere [Miura and Pritchett, 1982]. However, the orientation of the plasma’s background magnetic field can have a stabilizing effect on the KHI [Miura and Pritchett, 1982]. This can be expressed mathematically by the Kelvin-Helmholtz (KH) instability criterium, which will be discussed in more detail in Chapter 2. Despite the stabilizing effects of the magnetic field, the KHI occurs regularly at the magnetopause boundary and plays an important roll in coupling the solar wind and magnetosphere [Otto and Fairfield, 2000; Fairfield et al., 2000; Nykyri et al., 2003a; Hasegawa et al., 2004; Nykyri et al., 2006a; Taylor et al., 2008; Foullon et al., 2008; Merkin et al., 2013; Lin et al., 2014; Ma et al., 2014a,b; Nykyri et al., 2017; Ma et al., 2017; Sorathia et al., 2019].

The KHI was initially understood to be an ideal instability, which could transfer

energy and momentum from the solar wind to the magnetosphere, but not mass [Miura, 1984, 1987]. However, later simulations indicated non-linear stages of the KHI could twist the magnetic field to produce reconnection leading to mass transport [Nykyri and Otto, 2001, 2004; Otto and Fairfield, 2000]. Observations with the Cluster spacecraft [Nykyri et al., 2006a; Hasegawa et al., 2004] confirmed the presence of reconnection within KH vortices. Further, simulations and observations have shown that the KHI can drive several secondary processes in addition to reconnection, such as kinetic Alfvén waves [Moore et al., 2016, 2017], ion-acoustic waves [Wilder et al., 2016], wave mode conversion [Johnson et al., 2001; Chaston et al., 2007], and turbulent heating [Stawarz et al., 2016].

Reconnection in the KHI can occur even when the magnetic field is initially parallel on either side of the boundary. As can be seen in Figure 1.8, initially parallel field lines are twisted within the KH vortex. As the field is twisted, regions of antiparallel field develop and reconnect. The resulting “magnetic islands” of cold, dense magnetosheath plasma are mixed into the hot and tenuous magnetosphere, effectively transferring energy and mass across the magnetopause boundary. Such reconnection has been observed by the Cluster [Nykyri et al., 2006a; Hasegawa et al., 2004], and MMS missions [Eriksson et al., 2016]. In addition to direct plasma entry to the magnetosphere, reconnection within the KHI can produce ion beams which drive smaller scale wave modes (e.g. the fast magnetosonic wave) capable of effectively heating ions within the plasma.

The strongly fluctuating magnetic fields within the KHI can also lead to wave mode conversion [Johnson et al., 2001; Chaston et al., 2007]. Within a KH vortex, magnetic field lines are twisted and compressed, resulting in rapid changes in the

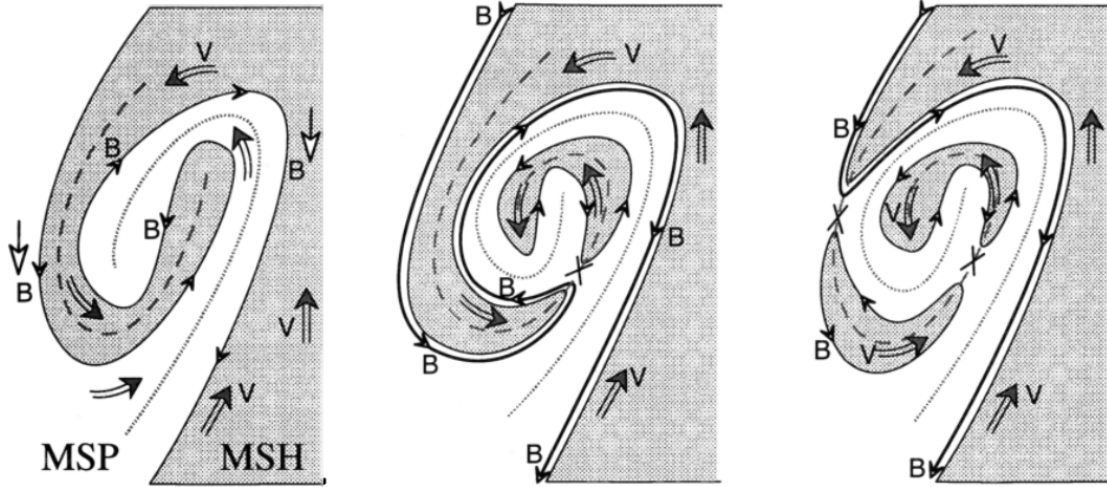


Figure 1.8: Magnetic reconnection within a KH vortex, as depicted in *Nykyri and Otto* [2001], leads to plasma heating and transport from the magnetosheath to the magnetosphere.

magnetic field strength. The Alfvén velocity, which is a function of the magnetic field, will also change rapidly with the field strength. The rapid change in Alfvén velocity can lead to the development of an Alfvén resonance point, where surface mode waves are converted to kinetic Alfvén waves. Kinetic Alfvén waves are capable of heating and transporting plasma across the magnetopause boundary. Recent work by *Nykyri et al.* [2021b] has shown that these can even contribute to parallel electron heating, but in that case did not account for the total observed heating.

Work by *Moore et al.* [2016, 2017] also observed evidence of kinetic Alfvén and fast magnetosonic waves inside KH vortices. The observed KH associated wave activity provided increased energy which could contribute to enhanced ion heating during the KHI but is not available when the KHI is not active [*Moore et al.*, 2017].

Observations have shown the KHI may form on both the dawn and dusk flanks under any orientation of the interplanetary magnetic field [*Kavosi and Reader*, 2015],

but simulations have shown a preference for dawn flank formation when the IMF is in a Parker Spiral (PS) orientation [Nykyri, 2013; Adamson *et al.*, 2016]. Recent work by Henry *et al.* [2017] analyzed the events presented in Kavosi and Reader [2015] and confirmed this preference observationally. Henry *et al.* [2017] also confirmed a preference for KHI formation at the dusk flank for high solar wind speeds under northward IMF (NIMF). As PS is the most statistically common IMF orientation, it follows that the associated preference for dawn-side KHI development would also be statistically more common. Such asymmetry in the formation of KHI, combined with KH-driven secondary processes like reconnection and kinetic scale waves, make the KHI a strong candidate to drive the dawn-dusk asymmetry of cold-component ions in the plasma sheet.

Prior to 2015 observational studies of secondary processes within the KHI had been limited to the ion scale due to spacecraft and technical capabilities. The launch of the MMS mission in 2015 presented a new opportunity to finally investigate KHI associated processes below the ion scale. The work presented in this dissertation takes advantage of the MMS capabilities, described in the next section, to identify ion scale wave modes within the KHI and their contribution to heating (see Chapter 4). The techniques developed in Chapter 2 to analyze the MMS data can, in future work, be used to identify wave modes at smaller scales.

## 1.4 The Magnetosphere Multiscale Mission

Launched in March 2015, the Magnetosphere Multiscale (MMS) mission was designed to “understand the microphysics of magnetic reconnection” [Burch *et al.*, 2016]. In

order to understand the physics which violates the frozen in condition and drives reconnection, MMS must be able to resolve plasma processes down to the electron scale. The design of the MMS mission reflects this goal.

MMS is a constellation of four identical spacecraft, each equipped with the most complete and capable suite of instruments available for observing the details of magnetic reconnection. Spacecraft separations of less than 10 km are an order of magnitude closer than previous missions. The instruments on board MMS also operate with temporal cadences several orders of magnitude faster than previous satellite missions. Four spacecraft flying in close formation allow for the separate identification of temporally and spatially varying phenomena; for example, MMS is capable of distinguishing a moving site of ongoing reconnection from a stationary site of patchy reconnection [Burch *et al.*, 2016]. The high spatial and temporal resolution of MMS may also be employed to identify sub-ion scale processes and waves developing within a KH vortex.

Due to its reconnection specific objectives, the MMS mission's orbits were selected to maximize its time near likely reconnection sites, namely the subsolar dayside magnetopause and the plasma sheet in the magnetotail. These two areas were targeted separately by different phases of the MMS mission. In Phase 1, the dayside magnetopause was observed using a highly elliptical orbit with apogee  $\approx 12$  Earth radii ( $R_E$ ). The apogee was increased to  $\approx 25R_E$  to better observe tail reconnection in Phase 2 [Burch *et al.*, 2016]. Figure 1.9 depicts approximate orbits in both Phase 1 and 2. While the KHI is not expected to be observed at either the subsolar magnetopause or the in plasma sheet, the MMS orbits encounter the flank magnetopause frequently in both Phase 1 and 2. Thus, MMS is expected to observed the KHI with

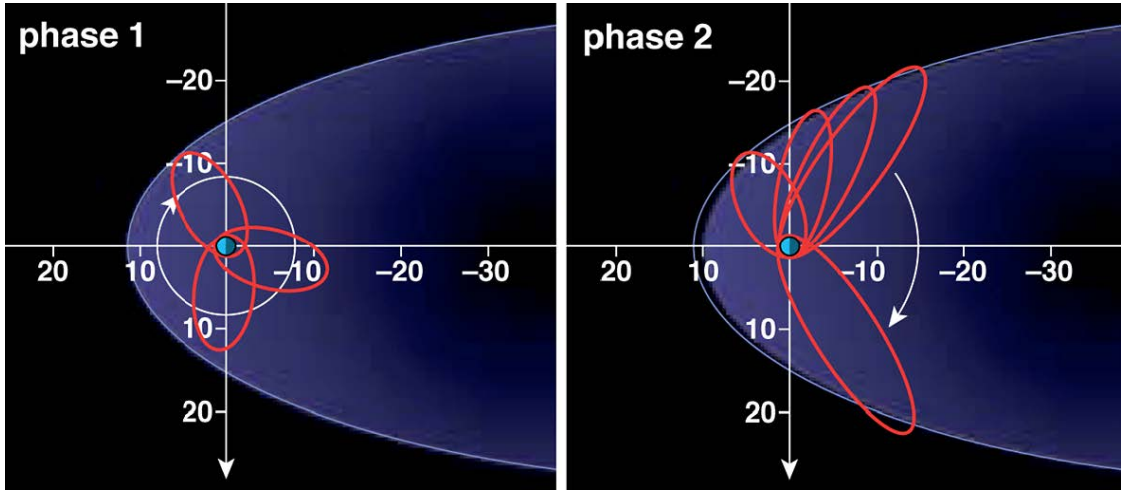


Figure 1.9: MMS orbits for Phase 1 (left), targeting the dayside magnetopause, and Phase 2 (right), targeting tail reconnection, from *Burch et al.* [2016]. Both orbits provide ample opportunity to observe the KHI developing on the flank magnetopause.

some regularity.

The MMS mission’s combination of high cadence measurements and small spacecraft separation allows for the observation of plasma behavior down to the electron scale. While this design was created with magnetic reconnection in mind, it also provides the opportunity to study the influence of the KHI on small scale waves, heating, and plasma transport. The MMS orbit is also excellent for the observation of the KHI. Phase 1 orbits are capable of observing KH waves along the dayside flanks, and the Phase 2 orbit allows the search for KH events to extend into the tail flanks.

Within a year of its launch, MMS yielded an excellent case study of sub-ion scale processes within the KHI. *Eriksson et al.* [2016] reported reconnection within a KH vortex on the dayside dusk flank. Further investigations of the same event showed evidence of ion-acoustic waves [*Wilder et al.*, 2016] and turbulence [*Stawarz et al.*, 2016]. These secondary processes can contribute to ion heating and plasma transfer

across the magnetopause boundary.

## 1.5 Motivation

Case studies, like those done by *Eriksson et al.* [2016]; *Wilder et al.* [2016] and *Stawarz et al.* [2016] are useful in identifying the fine-scale secondary processes associated with the KHI, but statistical studies are necessary to fully understand the role these processes play in driving solar wind-magnetosphere coupling. The work presented in this dissertation gathers MMS observations of 45 KHI events between September 2015 and March 2020 in an effort to determine the influence of small scale waves within the KHI on magnetospheric dynamics.

In order to better understand the role the KHI and its secondary process play in driving solar wind-magnetosphere coupling it is imperative, as a first step, to build a database of MMS encounters with the KHI. The methods and tools used to identify and analyze KH events in MMS data are presented in Chapter 2. In Chapter 3, the large scale characteristics of each event are correlated with solar wind conditions and observation location to establish patterns which may prove informative in understanding the role the KHI plays in magnetospheric dynamics. A statistical study of small scale wave intervals associated with the KHI and a discussion of their generation mechanisms are presented in Chapter 4.

# Chapter 2

## Research Methodology

The methodology presented in this chapter has been published, in part, in *Rice et al.* [2022]. Portions are still in preparation for submission to *Geophysical Research Letters*.

### 2.1 Data

#### 2.1.1 MMS Instrumentation and Data Products

The MMS data used in this work is publicly available via the MMS Science Data Center (SDC). MMS data is classified as either Level 1, Quicklook, or Level 2 data. Level 1 data is the raw, uncalibrated measurements taken directly from instruments onboard the spacecraft; it is not publicly available because it has not been calibrated or processed. Quicklook data has undergone some preliminary processing, and is made available via Quicklook plots within days of receipt from the spacecraft. Level 2 data is science ready data; it has been calibrated and processed for use in detailed



analysis. Level 2 data is made publicly available within 30 days of downlink [*Baker et al.*, 2016]. The work presented here uses Level 2 data, though Quicklook data was also referenced in order to identify large scale features which merited more detailed analysis.

MMS has two main operational modes: burst and survey. In survey mode, data is collected at “low to medium” resolution [*Baker et al.*, 2016]. The low-medium resolution data provided by MMS is in line with previous missions such as Cluster and THEMIS. Burst mode data is the highest resolution data from MMS and provides orders of magnitude better resolution than previous missions. All data collected by MMS must be temporarily stored onboard the spacecraft before it is downloaded. Due to its high measurement cadence, burst mode data is computationally expensive to collect and store. Therefore MMS only operates in burst mode in scientific “regions of interest.” Additionally, data quality values and a Scientist in the Loop (SITL) select only the burst segments with the most promising scientific value for download [*Baker et al.*, 2016]. As the KHI is a fluid scale instability, survey mode observations are more than sufficient to resolve its general structure. Survey mode data is also sufficient to resolve ion scale processes within the KHI, for which time scales are typically on the order of 1 Hz. Much below the ion scale, burst mode data is required.

The MMS instruments used for the bulk of this work are the fast plasma investigation (FPI), which measures ion and electron distribution functions and moments [*Pollock et al.*, 2016]; the flux gate magnetometer (FGM), which measures the 3 dimensional direct current magnetic field [*Russell et al.*, 2016]; the search coil magnetometer (SCM), which measures the 3 dimensional alternating current or wave magnetic field [*Le Contel et al.*, 2016]. The 3 dimensional electric field is measured

Table 2.1: The MMS instruments used in this study, along with their operational modes and observational cadences.

Instrument	Measurements	Modes	Cadence
FPI	Ion and electron distributions and moments	Fast Burst	4.5s 30 ms electrons, 150 ms ions
FGM	3D direct current magnetic field	Slow Survey Fast Survey Burst	8 Hz 16 Hz 128Hz
SCM	3D alternating current (wave) magnetic field	Survey Slow Fast Burst	8 Hz 32 Hz 1024 Hz 8192 Hz
EDP	3D electric field	Survey Slow Fast Burst	8 Hz 32 Hz 1024 Hz 8192 Hz
HPCA	Ion distributions and moments by species	Survey Burst	10-15s

by the spin-plane and axial double probes (SDP, ADP, respectively) and electron drift instrument (EDI), which together make up the Electric Double Probe (EDP) [Lindqvist *et al.*, 2016; Ergun *et al.*, 2016; Torbert *et al.*, 2016a]. The FGM, SCM, and EDP are all part of the larger FIELDS instrument suite [Torbert *et al.*, 2016b]. Data from the hot plasma composition analyzer (HPCA), which measures distribution functions separately for various ion species, is also used to determine the effects and significance of minor ion species to the behavior of the overall plasma population [Young *et al.*, 2016]. Details of the measurements and observation cadences for all of the instruments we use are listed in Table 2.1.

### 2.1.2 Upstream Solar Wind Observations

Solar wind data is taken from the OMNI database, maintained by NASA’s Goddard Space Flight Center. The OMNI database comprises solar wind data from 20 satellites, spanning nearly 60 years of observations [King and Papitashvili, 2005]. High resolution (1 minute) observations of the solar wind near Earth are made using the ACE, Wind, and ISEE-3 satellites [King and Papitashvili, 2005]. These observations include plasma parameters, such as density and flow speed, and measurements of the embedded IMF strength and orientation. As this work primarily uses the IMF and solar wind data to determine average conditions under which the KHI develops, the 1 minute resolution of OMNI data is sufficient.

## 2.2 Data Analysis

### 2.2.1 KHI Analysis Tools

#### Observational Signatures and Detection of the KHI

In the 4.5 years after it began observations in 2015, MMS made thousands of crossings and partial crossings of the magnetopause. In order to narrow down the many magnetopause crossings to those in which KHI is active, we first consult the MMS Mission Event database available as part of the MMS SDC. In that time frame, the SITL responsible for selecting burst mode data for download and noting potential events marked approximately 80 timespans as potentially containing KH activity. Quicklook plots were also searched for unstable boundary crossings not marked in the SITL notes as KHI. In total, around 100 intervals were selected and checked by

eye for the characteristic signatures of the KHI. The six primary signatures used to identify the KHI within MMS data are

1. Quasi-periodic fluctuations in the omnidirectional ion energy spectrogram between magnetosheath and magnetospheric energies,
2. Quasi-periodic, anti-correlated fluctuations in ion density and temperature,
3. Large velocity shears, on the order of 100s of km/s,
4. Fluctuations in the total magnetic field as it is twisted and compressed within the KH vortex,
5. Bipolar signatures in the normal component of the magnetic field,  $B_N$ , and
6. Fluctuations in total pressure, particularly with maxima near the edges of the KH vortex and minima at the center of the KH vortex where the normal component of the magnetic field is near 0.

When MMS crosses a stable magnetopause boundary, we expect to see a smooth transition from plasma with energy typical of the magnetosheath, through a region of intermediate energy plasma, to plasma with typical magnetospheric energy (or vice versa). When the boundary is not stable, this transition will not be smooth, and may show alternating regions of plasma with energies typical of the magnetosheath and magnetosphere, as well as mixed energies. For the case of a boundary disturbed by a periodic instability like the KHI, these alternating regions should be relatively periodic (Signature 1). The periodic observation of magnetosheath and magnetospheric regions will also be evident in the ion density and temperature, as MMS

alternately encounters regions of plasma from the cold, dense magnetosheath and the hot, tenuous magnetosphere (Signature 2).

Large velocity shears are common at the flank magnetopause, where the magnetosphere is relatively stagnant and the magnetosheath plasma is accelerating from low speeds immediately after the shock to “catch up” with the solar wind speed farther downtail [*Dimmock and Nykyri, 2013*]. Velocity shears are also a necessary condition for the development of the KHI [*Chandrasekhar, 1961; Miura, 1984, 1987*] (Signature 3).

As the KHI develops, it begins to twist the boundary and compress the magnetic field lines. The total magnetic field strength will fluctuate as the field lines are compressed (Signature 4). In particular, these fluctuations should appear as bipolar variations in the normal component as the KH vortex twists the field lines (Signature 5). Changes in the normal component and total field strength help distinguish the KHI from a shifting boundary, such as a response to solar wind dynamic pressure variations.

The rotational nature of the KHI creates an outward force which is balanced by a pressure gradient, resulting in a decrease in total pressure at the center of the KH vortex. Thus, observations of the KHI show a lower total pressure near the center of the vortex (where  $B_N$  is zero) and a higher pressure in the spine regions (Signature 6). This signature allows us to distinguish the KHI from a flux transfer event in which total pressure typically increases when  $B_N$  is zero [*Nykyri et al., 2006a; Zhao et al., 2016*].

All six characteristic signatures may be seen in the example observation shown in Figure 2.1. From 16:35 to 19:07 UT on 26 September 2017, MMS1 encountered the

KHI as it crossed the magnetopause on the dusk flank of the tail magnetosphere. MMS1 observed alternating regions of magnetosheath and magnetospheric energy plasma with a periodicity of about 3.5 minutes. Anti-correlated fluctuations in ion density and temperature have a similar periodicity. Velocity shears on the order of 200 km/s are seen primarily in the GSM  $X$ -component, as is expected for a KHI occurring along the tail magnetopause. The total magnetic field strength varies by as much as 10 nT throughout the observations. Bipolar fluctuations in the normal component of the field are present for the duration of the event as well. Decreases in total pressure correspond well with times at which  $B_N$  is near 0.

Ideally, a single KHI will exhibit all six signatures, but real observations are rarely ideal and one or more signatures may not be present. For example, MMS may skim the magnetopause boundary while KHI is operating, without fully crossing the boundary. In this case, MMS may observe quasi-periodic fluctuations in the omnidirectional ion energy, but those fluctuations may not represent typical magnetosheath or magnetosphere energies. Such a skimming encounter may also miss the center of the KH vortex, and thus the changes in total pressure may not be evident or well aligned with times when  $B_N$  is near 0.

Our initial search for KHI observations uses only single spacecraft observations of the magnetic field and proton moments. The fluid scale KHI is much larger than the ion scale and the MMS spacecraft separation, therefore observation of the bulk ion behavior from a single spacecraft is sufficient to identify the KHI and all four spacecraft are expected to observe nearly identical signatures over the several Earth-radii scale of the KHI. Heavier ion species, such as  $\text{He}^+$  and  $\text{O}^+$  are not considered in our initial search for the KHI. At the magnetopause where KHI operates, these

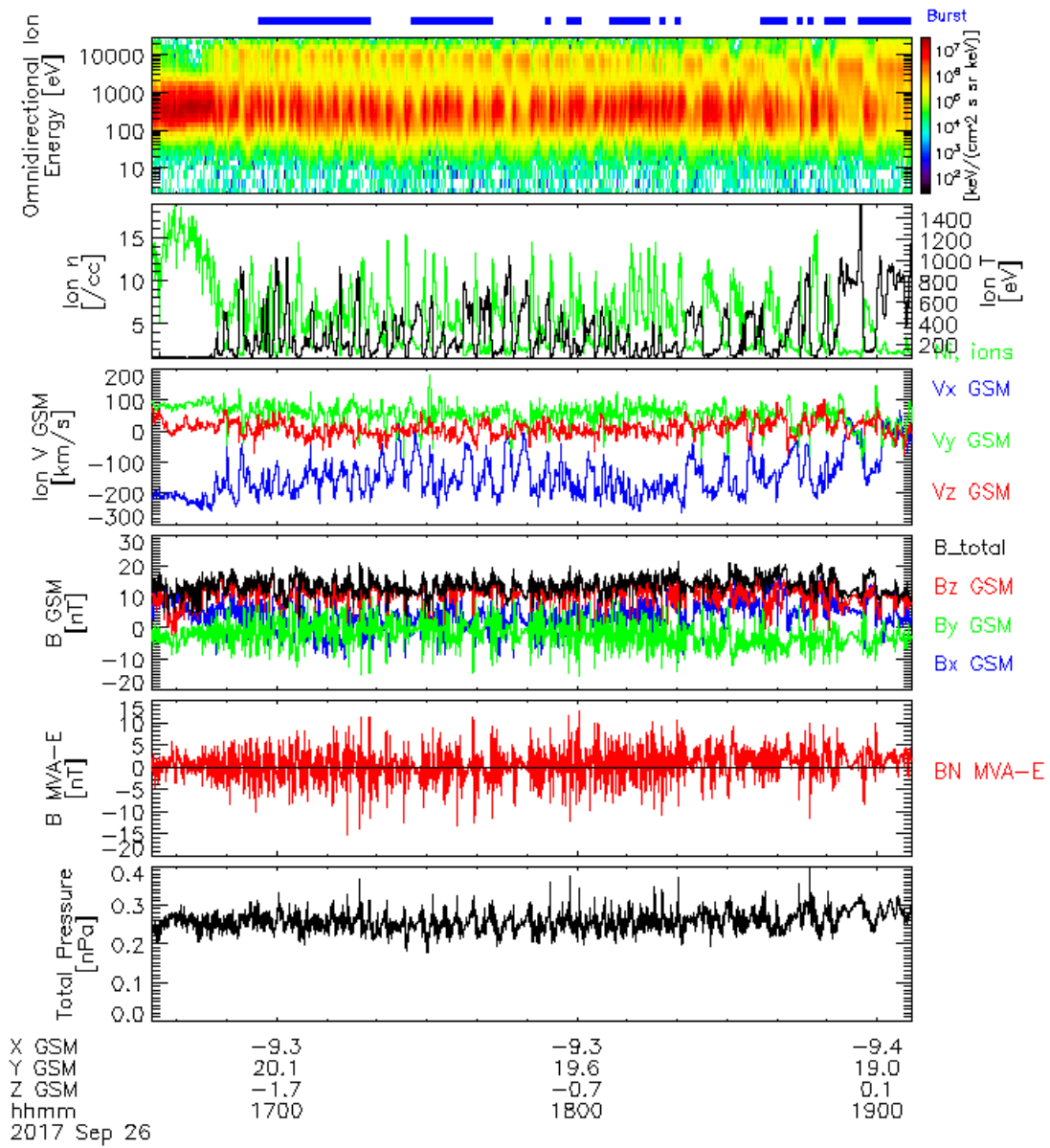


Figure 2.1: MMS observations of the KHI from 16:35 to 19:07 UT on 26 September 2017.

heavier species make up only a small fraction of the total plasma population and make an insignificant contribution to the overall behavior of the fluid-scale KHI.

### **Events from September 2015 to March 2020**

From the beginning of its operation in September of 2015 to March 2020, MMS made thousands of full and partial magnetopause boundary crossings. Approximately 100 of those crossings contained signatures of transient phenomena and instability resembling the KHI. More detailed checks of pressure and the boundary-normal components of the magnetic field allowed us to narrow this list of potential KH encounters to 45 confirmed observations, only two of which had been reported prior to the publication of *Rice et al.* [2022] [*Eriksson et al.*, 2016; *Nykyri et al.*, 2021b; *Michael et al.*, 2021]. All 45 observations exhibit the six expected signatures, though total pressure decreases could not always be aligned with points at which the magnetic field normal component is near 0. For events when  $B_N$  and total pressure were not well aligned, orientation of the IMF is checked. We keep only events for which the IMF is unlikely to support foreshock transients at the flank on which the event is observed.

Table 2.2 details the date, onset time, duration, location, and approximate KH wavelength of each of the 45 events. Here the “onset time” refers to the time at which MMS first observed the KHI. It is likely the KHI had already been operational for some time prior to observation by the MMS, but it is not possible to estimate how long the KHI may have persisted from observations alone.

The 45 MMS observations of the KHI are well varied, ranging in duration from 10 minutes to nearly 13 hours. There are more observations on the dusk flank (29 events) than the dawn (16), but without weighted comparisons based on solar wind



conditions and spacecraft orbit patterns, the difference in observations between the two flanks does not indicate a preference for KHI development at dusk. Observations are evenly split between the dayside and tail magnetopause: 22 (23) events occur sunward (tailward) of the terminator. Nightside KHI are all observed in or after May 2017. This is primarily due to a sampling effect of the MMS orbit change from Phase 1, which targeted the dayside magnetosphere, to Phase 2, which targeted the tail. Burst mode data is available for portions of all 45 events, which is crucial for the study of wave activity below the ion scale.

Table 2.2: The date, onset time, duration, GSM location, and estimated wavelength of the 45 KHI events observed by MMS from September 2015 to March 2020. Burst mode data is available for portions of all events.

Event No.	Date	Onset Time UT	Duration [min]	GSM Location [ $R_E$ ]	KH Wavelength [ $R_E$ ]
01	08 Sep 15	09:00	170	[5.0, 7.4, -4.5]	2.80
02	15 Sep 15	10:45	240	[5.1, 8.7, -5.5]	5.00
03	11 Oct 15	10:30	30	[8.7, 6.5, -4.7]	3.71
04	15 Oct 15	06:00	60	[9.0, 4.1, -2.3]	2.29
05	17 Oct 15	16:00	28	[6.4, 7.8, -4.1]	4.94
06	18 Oct 15	15:00	25	[7.2, 7.5, -4.4]	8.18
07	22 Dec 15	22:15	35	[7.9, -5.7, -1.8]	2.58
08	11 Jan 16	20:52	18	[6.2, -7.6, -3.4]	1.99
09	19 Jan 16	19:57	38	[5.3, -8.2, -3.9]	3.25
10	05 Feb 16	18:55	35	[3.3, -9.3, -5.0]	5.97
11	07 Feb 16	03:45	55	[7.0, -6.9, -3.5]	4.20

Continued on next page

Table 2.2: Continued from previous page

Event No.	Date	Onset Time UT	Duration [min]	GSM Location [ $R_E$ ]	KH Wave-length [ $R_E$ ]
12	18 Feb 16	19:30	70	[2.5, -9.7, -6.3]	6.81
13	25 Feb 16	18:55	70	[1.3, -9.9, -6.5]	2.26
14	26 Sep 16	14:15	70	[2.7, 8.5, -5.4]	11.85
15	27 Sep 16	19:50	20	[0.3, 11.5, -3.4]	2.62
16	04 Oct 16	18:20	70	[1.8, 11.2, -3.6]	9.51
17	10 Oct 16	14:40	60	[4.3, 9.3, -5.0]	9.43
18	24 Oct 16	10:50	30	[6.8, 6.1, -4.3]	1.09
19	04 Nov 16	11:45	75	[8.1, 7.2, -3.8]	2.28
20	03 May 17	02:00	150	[-12.9, -19.7, -3.9]	17.39
21	08 May 17	13:00	110	[-14.8, -17.2, 0.3]	11.50
22	11 May 17	12:00	150	[-15.6, -18.2, 1.4]	18.47
23	11 May 17	15:44	31	[-15.3, -19.2, -0.3]	7.75
24	19 May 17	23:58	107	[-17.8, -16.6, -2.1]	20.72
25	20 May 17	02:00	150	[-17.6, -17.4, -0.6]	26.65
26	20 Sep 17	22:32	43	[-10.8, 20.9, 1.3]	8.20
27	26 Sep 17	16:35	152	[-9.3, 19.6, -0.9]	6.47
28	16 Oct 17	14:30	50	[-4.0, 18.6, -2.7]	7.71
29	30 Oct 17	19:05	35	[-0.6, 17.3, 1.6]	4.20
30	02 Nov 17	17:25	50	[-0.9, 14.8, 0.8]	6.38
31	03 May 18	00:15	35	[-9.3, -17.5, -2.3]	8.43

Continued on next page

Table 2.2: Continued from previous page

Event No.	Date	Onset Time UT	Duration [min]	GSM Location [ $R_E$ ]	KH Wave-length [ $R_E$ ]
32	18 Sep 18	15:50	25	[-14.1, 20.6, -1.0]	5.17
33	24 Sep 18	14:10	195	[-14.1, 20.3, -1.6]	19.35
34	02 Oct 18	23:45	35	[-10.8, 22.5, 2.1]	11.25
35	04 Oct 18	17:25	10	[-0.8, 16.2, -0.2]	2.50
36	13 Apr 19	07:45	30	[-0.6, -17.5, 2.4]	9.68
37	03 Jun 19	23:05	75	[-2.2, -14.9, -3.8]	7.46
38	25 Sep 19	13:45	765	[-16.7, 22.0, -0.2]	12.33
39	02 Oct 19	08:15	165	[-9.9, 21.5, -4.5]	8.54
40	02 Oct 19	16:00	80	[-12.9, 23.5, -2.1]	13.03
41	02 Oct 19	21:40	25	[-14.6, 24.0, 1.1]	7.11
42	06 Oct 19	14:50	175	[-14.8, 24.4, -4.2]	17.10
43	15 Oct 19	19:00	75	[1.2, 12.8, 2.9]	8.81
44	22 Oct 19	22:00	20	[1.8, 15.3, 3.8]	3.76
45	12 Nov 19	20:30	75	[6.7, 11.8, 5.2]	7.04

Solar wind and IMF data from OMNI is available for 44 of the 45 KHI events, which occur under the full range of typical conditions. We consider the planar ( $B_X$  and  $B_Y$ ) and  $B_Z$  components of the IMF separately. At the onset time, the planar components of the IMF show a preference for Parker Spiral Orientation (17). Less common orientations include radial, duskward, and dawnward (8 each). The remaining three events are first observed during Ortho-Parker Spiral orientations. The

average IMF orientation for the duration of each event is most often the Parker Spiral (17), followed by radial and dawnward (8 each). Duskward (6) and ortho-Parker Spiral (5) orientations are less common. At the time of first observation, the  $B_Z$  component of the IMF is more often northward (27) than southward (17). This holds true over the duration of the events as well: 26 (18) of the observations are made during average  $B_Z$  positive (negative).

More details about the 45 observed events and their large scale properties are discussed in Chapter 3.

### **Challenges in Event Identification**

The identification of transient phenomena in satellite data is difficult. Several boundary processes may create signatures which resemble those of the KHI. For example flux transfer events (FTEs) are large ropes of magnetic flux which can produce bipolar signatures in the normal component of the magnetic field, much like the KHI. Pressure gradients in a FTE are different than those in the KHI. Within the KHI, pressure decreases at the center of the rotational vortex, where the normal component of the magnetic field is near 0. At the edges of the KH vortex the total pressure is larger and the plasma is compressed, which can correspond with increases in both density and magnetic field strength. Within a FTE, however, pressure minima correspond with times of enhanced magnetic field strength [*Nykyri et al.*, 2006a; *Zhao et al.*, 2016].

Surface wave modes may also resemble the linear stages of the KHI. A shifting magnetopause boundary caused by dynamic pressure pulsations in the solar wind may also mimic the KHI. In both cases, we rely on fluctuations in the magnetic field to help us distinguish the KHI from other processes. We may also consult solar

wind observations to determine if any pressure pulsations are ongoing during the observations. Additionally, IMF orientation can help rule out foreshock transients creating signatures similar to the KHI.

Absolute certainty in event identification is simply not possible; too many competing explanations can account for some of the signatures associated with the KHI. The observed KH events in this work are no different. Alternate explanations exist and may be true for any single event. We believe, however, the events presented and analyzed in this work are more likely than not to be the KHI.

### **Automated Region Sorting**

When analyzing the KHI, it is often necessary to separate plasma populations originating on either side of the boundary. In case studies, or studies of only a handful of events, this is typically done manually. A few minutes of apparently pure magnetosheath and magnetospheric observations are used to characterize the different populations. This works well enough on a case by case basis, but is not efficient or easily reproducible over the many events included in a statistical study. Instead, we seek to develop a method which will automatically identify regions of magnetosheath and magnetospheric plasma which may be used to characterize the populations in calculations and analysis.

The magnetosheath, comprising the shocked solar wind, is typically cold, dense, and flowing quickly along the flanks. In contrast the magnetosphere is hot, tenuous, and relatively stagnant. Therefore we have three parameters with distinct values on either side of the boundary: density, temperature, and velocity. Used in combination they are able to distinguish the two regions

We developed six sorting parameters to describe the regions, which are summarized in Table 2.3 and detailed below.

- The ratio of density to temperature,  $n/T$ .

The ratio of density and temperature is large in the cold, dense magnetosheath and small in the hot, tenuous magnetosphere. This parameter does not consider the velocity of the regions, but a constraint may be enforced such that any point considered to be in the magnetosphere has a tailward velocity component at least one standard deviation less than the mean tailward velocity of the magnetosheath. In this way less dense plasma that has already undergone mixing and is being dragged tailward with the magnetosheath is excluded from the identified pure magnetospheric region.

- Specific entropy,  $S = T/n^{2/3}$ .

Specific entropy is small in the cold, dense magnetosheath and large in the hot, tenuous magnetosphere. Again, the velocity is not considered with this parameter, but a velocity constraint may be applied in the same manner as for the ratio of density and temperature.

- The product of density and GSM- $X$  velocity,  $nv_x$ .

The product of density and GSM- $X$  velocity, essentially the number flux of particles, is large and negative in the dense, fast-flowing magnetosheath and small, either positive or negative, in the tenuous and stagnant magnetosphere. This method does not include any information about the temperature.

In order to simplify the inclusion of velocity in the sorting parameters, we derive a “tailward” velocity from the GSM  $X$  component, such that  $v_{tail} = |v_x - \max v_x|$ . Thus

the tailward velocity is strictly positive, with the magnetosphere velocity defined to be 0.

- The ratio of the product of density and tailward velocity and temperature,  $nv_{tail}/T$ .

The tailward velocity is multiplied with the previously described ratio of density and temperature, creating a new parameter,  $nv_{tail}/T$ , which is large in the magnetosheath and small in the magnetosphere. This parameter is dependent on all three quantities, and simplifies the methodology over applying a velocity constraint to already separated regions.

- The ratio of entropy and tailward velocity,  $S/v_{tail}$ .

The ratio of entropy and tailward velocity is small in the magnetosheath and large in the magnetosphere. However, due to the definition of the tailward velocity, there is always a point at which  $v_{tail} = 0$  and the ratio is singular. This point is ignored in our analysis and not sorted into either region.

- The ratio of tailward velocity and entropy,  $v_{tail}/S$ .

We also consider the ratio of tailward velocity and specific entropy,  $v_{tail}/S$ , which is large in the magnetosheath and small in the magnetosphere. This sorting parameter neatly avoids the singularity inherent in  $S/v_{tail}$ .

To apply the sorting parameters, we must first determine a magnetopause value. For each parameter, values are sorted, and a certain percentage of both extremes are used to calculate a mean, which is termed the magnetopause value,  $mp$ , of that sorting

Table 2.3: A summary of the sorting parameters developed here and their relative values in each region.

Parameter	MSH	MSP	Notes
$n/T$	Large	Small	Additional $v_x$ constraint added separately
$S$	Small	Large	Additional $v_x$ constraint added separately
$nv_x$	Large (-)	Small (-/+)	No influence from temperature
$nv_{tail}/T$	Large	Small	
$S/v_{tail}$	Small	Large	Singularity at $v_{tail} = 0$
$v_{tail}/S$	Large	Small	

parameter. The percent of data used to find this value ranged from 2.5% to 25% of both extremes, resulting in a mean calculated using between 5% and 50% of the total data contained in any one event. The mean of the entire dataset is unsuitable, because the spacecraft rarely observes the two regions in equal measure, thus  $mp$  would be an over (under) estimate of the magnetopause value for cases in which the spacecraft spent more time in the region where a sorting parameter is expected to be large (small) than the other. Using only a fraction of the entire event, and the extreme values representative of the most pure magnetosheath and magnetospheric regions gives a more reasonable value for  $mp$ .

Given the magnetopause value, we next determine cutoff values defining the magnetosheath and magnetosphere relative to  $mp$ . In the most simple method, data points with a sorting parameter value greater than or less than the magnetopause value would be assigned to the appropriate region. However, this ignores the physical implications of intermediate values very near  $mp$ . As the KHI operates, it mixes plasma and makes the boundary more diffuse, and any plasma with a sorting parameter value near  $mp$  has already been mixed, and is not representative of the pure magnetosheath or magnetosphere. Therefore, we must select cutoff values which better isolate the



pure magnetosheath and magnetosphere.

In the region in which a given sorting parameter is expected to be large, cutoff values are varied from  $1.0 * mp$  to  $1.9 * mp$ . The most restrictive values ( $> 1.7 * mp$ ) are ruled out because they do not return a reasonable or sufficient number of data points in the region. For some events, MMS never observed plasma which would fulfill the more restrictive criteria. The most relaxed cutoff values ( $< 1.3 * mp$ ) include too much mixed plasma from regions already strongly affected by the KHI. The inclusion of such mixed plasma has a significant but unpredictable effect. Marginal cutoff values, from  $1.4 * mp$  to  $1.6 * mp$  appear to be the best choice.

In the region in which a given sorting parameter is expected to be small, cutoff values were varied from  $0.1 * mp$  to  $1.0 * mp$ . As was true for the previous case, the most restrictive ( $< 0.3 * mp$ ) and the most relaxed ( $> 0.7 * mp$ ) cutoff values are unsuitable. The more restrictive values yield too little, and occasionally no, observations in the region. The more relaxed values include too much plasma already affected by mixing and heating processes in the KHI. The marginal cutoff values ( $0.4 * mp$  to  $0.6 * mp$ ) again seem to be the best choice.

The percentage of data used to determine  $mp$  and the cutoff values were varied in parallel. Plots of the density and temperature for both regions were created for all combinations of  $mp$  and cutoff values. Figures 2.2 and 2.3 show examples of these plots for the magnetosheath and magnetosphere density, respectively, for the KHI observed on 15 October 2015. As can be seen in Figure 2.2, the sorting parameters which are expected to be large in the sheath ( $n/T$ ,  $nv_x$ ,  $nv_{tail}/T$  and  $v_{tail}/S$ ) return density values between  $\approx 9$  and  $12$  /cc, in line with expectations for typical magnetosheath densities. Sorting parameters expected to be small in the sheath ( $S$  and  $S/v_{tail}$ )

return density values less than 6 /cc, which is lower than expected. We see a similar pattern in the magnetosphere, as is shown in Figure 2.3. Sorting parameters which are expected to be large ( $S$  and  $S/v_{tail}$ ), return density values in line with expectations,  $\approx 0.5$  /cc. Sorting parameters expected to be small in the magnetosphere ( $n/T$ ,  $nv_{tail}$ ,  $nv_{tail}/T$  and  $v_{tail}/S$ ), overestimate density, with results between 1 and 2 /cc. In both regions, the sorting parameters which are expected to be large perform much better than sorting parameters which are expected to be small. Thus, we find it best to use two sorting parameters in our automated region sorting method, one expected to be large in the magnetosheath and one expected to be large in the magnetosphere.

Additionally, Figures 2.2 and 2.3 show that the percent of data used to determine the magnetopause value,  $mp$ , has only a small effect on the mean density value in each identified region. As such, we choose to use the smallest and largest 12.5% (25% total) of all data for a given sorting parameter when determining  $mp$ . This ensures we are not only considering outliers, as would be the case if too little data were considered. Further, our value of  $mp$  will not be strongly effected if the spacecraft spends more time on one side of the boundary than the other, which would be the case if all the available data was included in determining  $mp$ .

Because no sorting parameter performed well in the region in which it is expected to be small, we must use two separate sorting parameters: one large in the magnetosheath and one large in the magnetosphere. We choose  $nv_{tail}/T$  as our sheath sorting parameter and specific entropy,  $S$ , as our magnetosphere sorting parameter. Both of the chosen sorting parameters produce consistent results over the range of marginal cutoff values ( $1.4*mp$  to  $1.6*mp$ ), suggesting they are robust and not overly sensitive to the selection of cutoff value. In order to balance our desire to select the

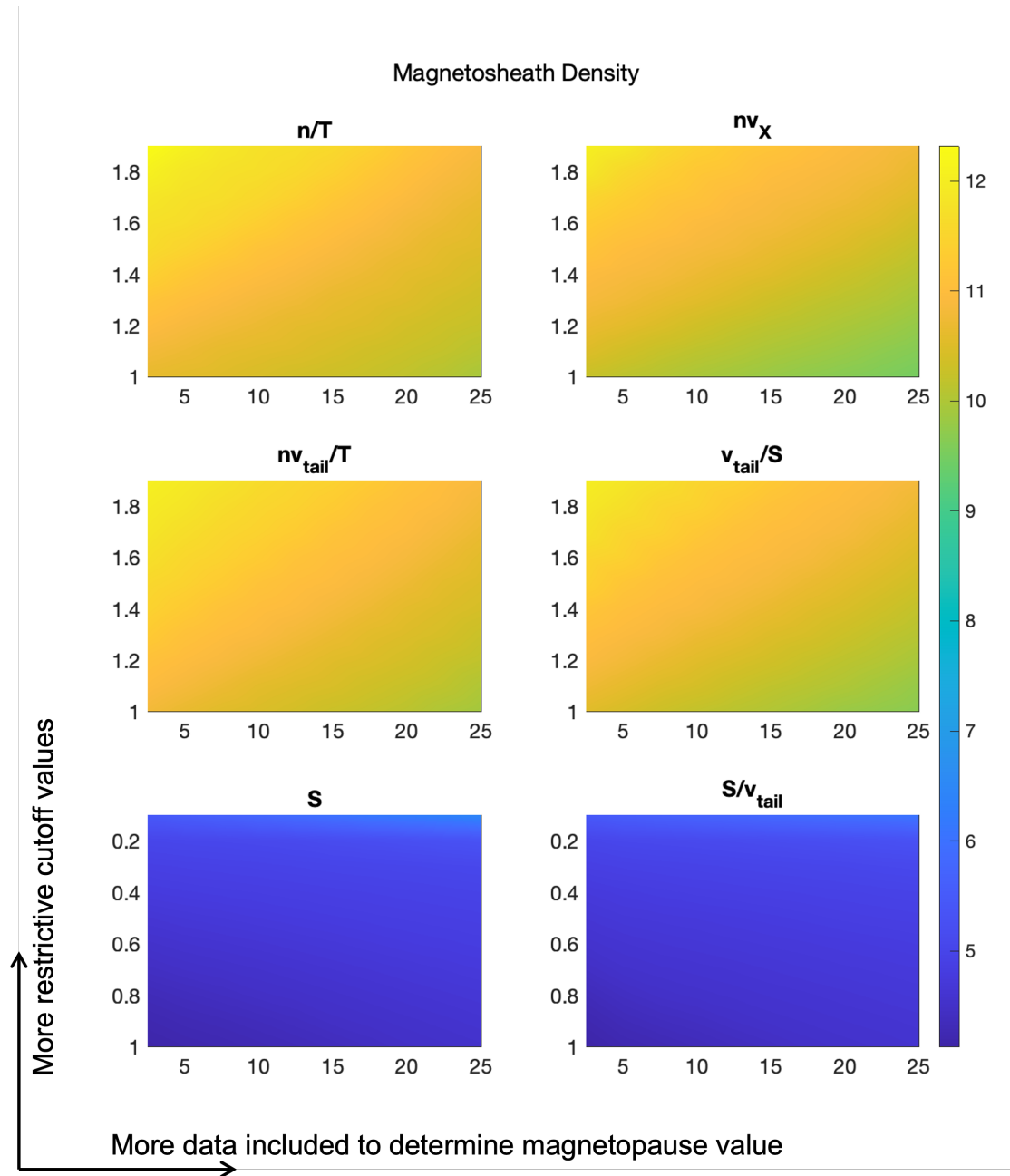


Figure 2.2: Sorting parameters which are expected to be large in the magnetosheath ( $n/T$ ,  $nv_x$ ,  $nv_{tail}/T$ , and  $v_{tail}/S$ ) provide reasonable density results. Parameters which are expected to be small in the magnetosheath ( $S$  and  $S/v_{tail}$ ) yield densities much lower than expected. Overly restrictive and overly relaxed cutoff values can negatively effect results. Sorting parameters are less sensitive to the percent of data used to determine the magnetopause value.

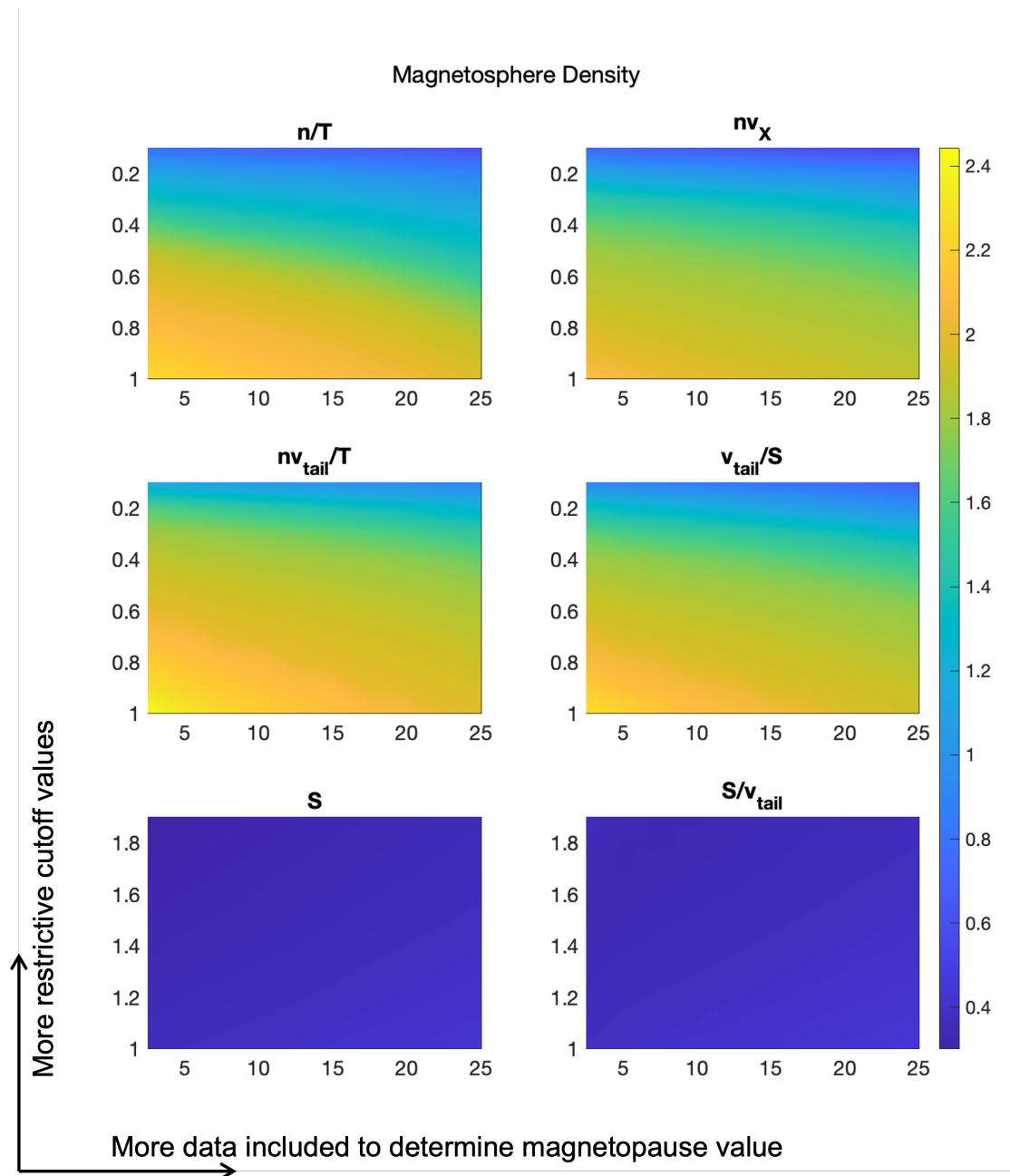


Figure 2.3: Sorting parameters which are expected to be large in the magnetosphere ( $S$  and  $S/v_{tail}$ ) produce reasonable density results. Parameters which are expected to be small in the magnetosphere ( $n/T$ ,  $nv_x$ ,  $nv_{tail}/T$ , and  $v_{tail}/S$ ) yield densities much higher than expected. Overly restrictive and overly relaxed cutoff values can negatively effect results. Sorting parameters are less sensitive to the percent of data used to determine the magnetopause value

most pure plasma from each region and the need to have a significant number of observational data points in each region, we select a cutoff value of  $1.5 * mp$  for both regions.

In summary, to identify regions of magnetosheath plasma, a time series of  $nv_{tail}/T$  is calculated for a KH event. The mean of the largest 12.5% of all  $nv_{tail}/T$  values and the smallest 12.5% of all  $nv_{tail}/T$  values are used to determine the magnetopause value  $mp$ . Any observation with  $nv_{tail}/T > 1.5 * mp$  is labelled the magnetosheath. The magnetosphere is identified in the same way, using  $S$  in place of  $nv_{tail}/T$ . Any observation which does not meet the criteria of either region is considered “mixed.” The sorting parameters, cutoff values, and identified regions are shown for the example KH event (26 September 2017) in Figure 2.4.

It is important to note, the effectiveness of the automated region sorting method is dependent upon the path of MMS through the KHI. The method works best when the spacecraft spends a significant portion of the event duration on both sides of the boundary. Events in which MMS only skims the KHI or spends significantly more time in one region than the other tend to result in identified regions with less contrast than typically expected of the pure magnetosheath and pure magnetosphere. The effects of observation geometry on the automated region sorting method are discussed in more detail in Section 2.3.

The new region sorting method was also compared with a region sorting technique previously published in *Moore et al.* [2017]. In that study, histograms of the most commonly observed energy channel at each time step are used to determine the typical energy values of the magnetosheath and magnetosphere, marked by the bright blue and red bins in the top panel of Figure 2.5. The log mean average of the two regions’

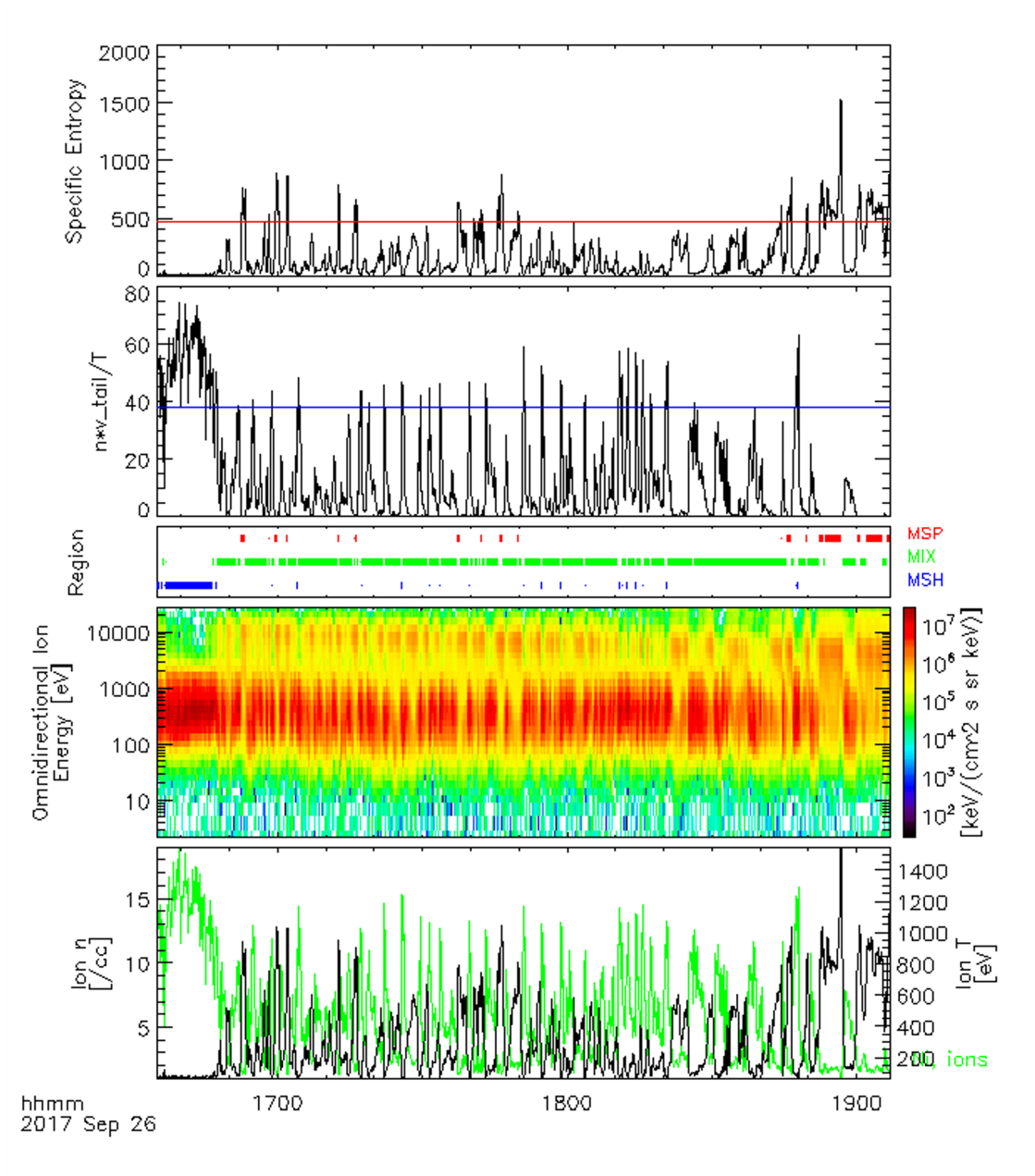


Figure 2.4: The sorting parameters,  $S$  and  $nv_{tail}/T$  are shown as a time series for the example event on 26 September 2017. Any plasma with  $S$  or  $nv_{tail}/T$  above the cut-off value (colored lines) is sorted in the magnetosphere or magnetosheath, respectively. The results of the automated region sorting method are in good agreement with expectations based on the omnidirectional ion energy and ion density and temperature.

energies is considered representative of the mixed plasma region. Each time step is then sorted into the region to which its weighted mean energy is closest. For KHI where the magnetosheath and magnetospheric energies are well separated, this method works well. In such cases, the Moore method produces results similar to the method developed here, as can be seen in Figure 2.5 for the example KH event on 26 September 2017. For the 45 MMS observations of the KHI, the new method sorts more plasma into the mixed region than the Moore method, as can be seen when comparing Figures 2.4 and 2.5. This is preferred, as the resulting regions are more representative of the “pure” magnetosheath and magnetosphere.

The KH event observed on 26 September 2016, shown in Figure 2.6, is a good example of the new region sorting method’s selection of only pure magnetosheath plasma. Plots of the MMS orbit show the spacecraft skimming the magnetopause boundary, primarily on the magnetosphere side, with only a brief excursion into the magnetosheath. Solar wind density is  $\approx 8$  /cc, corresponding to a magnetosheath density of  $\approx 32$  /cc per MHD shock physics. MMS observes density  $\approx 30$  /cc only after 15:15 UT, suggesting that MMS only observes pure sheath for around 10 minutes at the end of the observation interval and is otherwise in mixed or magnetospheric plasma. As can be seen in Figure 2.6, the new method identifies as the pure magnetosheath only the portion of MMS observations where density is nearly 30 /cc. The Moore method selects an early portion of the data as magnetosheath plasma based on its energy, even though the density and temperature are more consistent with mixed plasma.

The new method developed here has additional benefits over the Moore method. First, it is fully automated. The Moore method requires manual selection of the

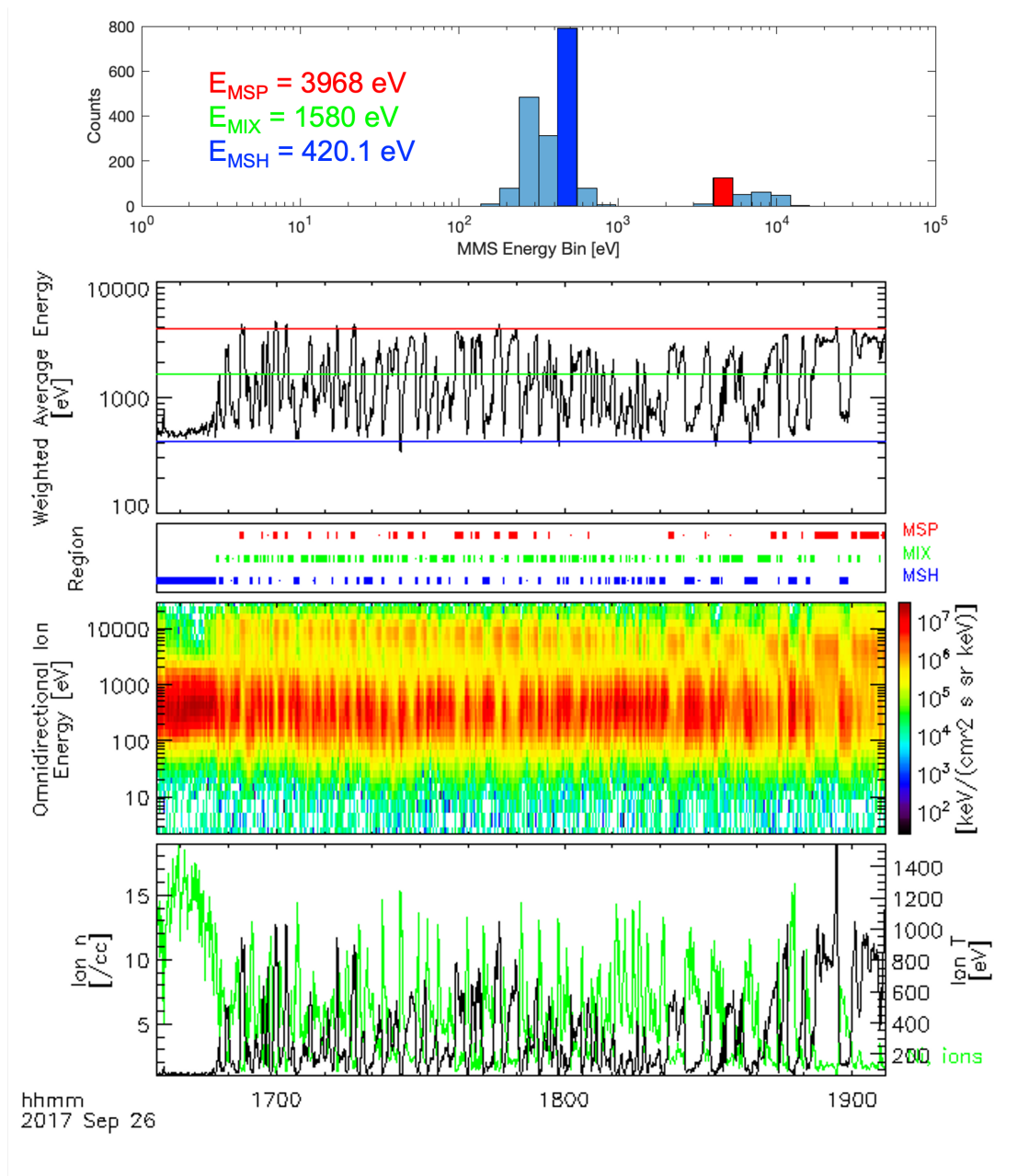


Figure 2.5: A region sorting technique from *Moore et al.* [2017] uses weighted averages of the ion energy to identify magnetospheric, mixed, and magnetosheath regions. Results are in general agreement with the omnidirectional ion energy and ion density and temperature, but identify less mixed plasma than the newly developed method.



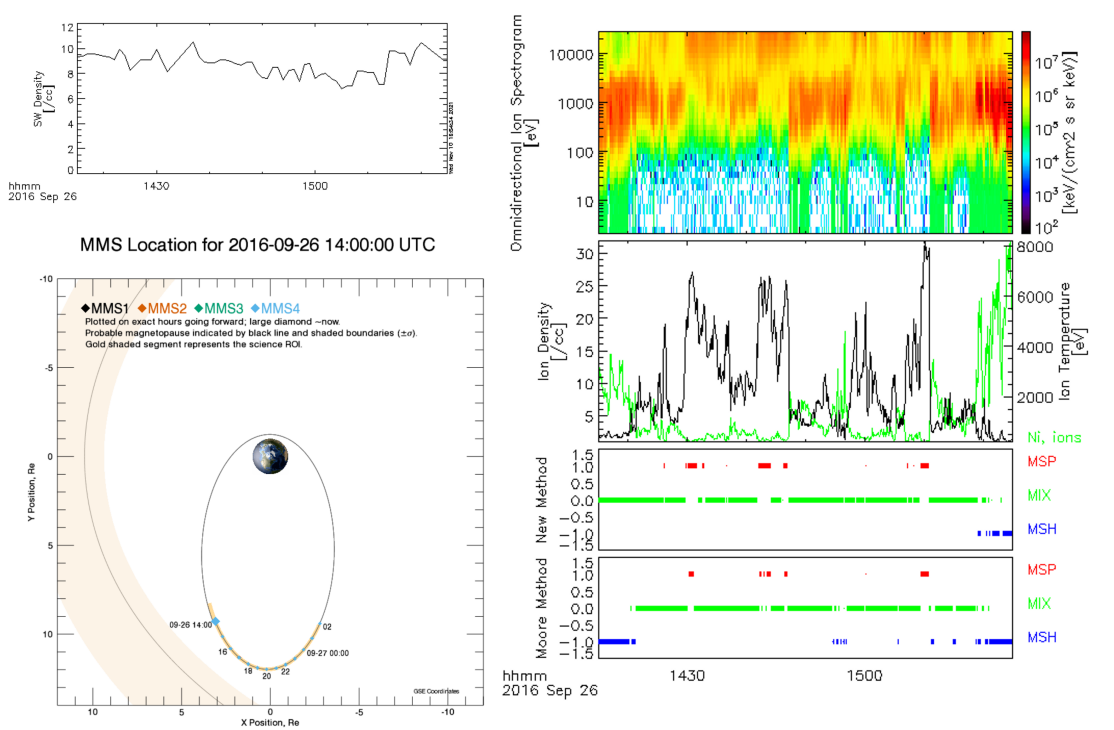


Figure 2.6: On 26 September 2016, MMS observed the KHI while skimming the magnetopause boundary (bottom). Solar wind density (top) suggests a magnetosheath density  $\approx 30$  /cc, which is only observed at the end of the interval. The new region sorting method developed here selects only the pure sheath, where density  $\approx 30$  /cc, while the method used in *Moore et al.* [2017] includes mixed plasma earlier in the interval (right).

magnetosheath and magnetospheric energies in the energy channel histograms. The energy channel histogram presents its own challenges. When the magnetosheath and magnetospheric energies are well separated, the two peaks in energy channels are obvious. If the characteristic energies are not as well separated, as is often the case for boundaries effected by the KHI, peak energies may not be clear. In more extreme cases, there may only be one peak energy channel, making the selection of both magnetosheath and magnetosphere energies very difficult, if not arbitrary. For these reasons, the automated region sorting method developed here is the best option for our analysis.

Though we are generally satisfied with the performance of the new automated region sorting method, work is still ongoing to ensure it is optimized. Comparison with high frequency field data from the SCM and EDP instruments may reveal signatures unique to the magnetosphere and magnetosheath. These signatures in the field may be used to separate the two regions independently of the ion moments. Alternatively, they may be used in conjunction with the new region sorting method to produce a more holistic definition of the sorted magnetosheath and magnetospheric plasmas.

### **The KHI Growth Rate and Unstable Solid Angle**

Assuming an infinitely thin boundary layer, a region unstable to the KHI will satisfy the KH instability criterium

$$[\mathbf{k} \cdot (\mathbf{v}_1 - \mathbf{v}_2)]^2 \geq \frac{n_1 + n_2}{4\pi m_0 n_1 n_2} [(\mathbf{k} \cdot \mathbf{B}_1)^2 + (\mathbf{k} \cdot \mathbf{B}_2)^2] \quad (2.1)$$

where  $\mathbf{v}_i$ ,  $n_i$ , and  $\mathbf{B}_i$  are the velocity, density, and magnetic field on either side of the velocity shear layer and  $\mathbf{k}$  is the wave vector [*Chandrasekhar*, 1961].

Equation 2.1 may be rearranged to determine the normalized growth rate of the KHI in a particular region, which is defined as

$$Q/k = \sqrt{a_1 a_2 (\Delta \mathbf{v} \cdot \hat{\mathbf{k}})^2 - a_1 (\mathbf{v}_{A1} \cdot \hat{\mathbf{k}})^2 - a_2 (\mathbf{v}_{A2} \cdot \hat{\mathbf{k}})^2} \quad (2.2)$$

where  $a_i$  is a density parameter on either side of the boundary, defined by  $a_i = \rho_i / (\rho_1 + \rho_2)$ ,  $\mathbf{v}_{Ai}$  is the Alfvén velocity, and  $\hat{\mathbf{k}}$  is the unit wave vector (thus the growth rate is normalized to the wavelength) pointing in the direction of maximum growth. We use only proton data to determine the values in Equation 2.2 as the low mass electrons have no meaningful influence on the growth rate, and minor ion species are not abundant enough to contribute significantly. Values for each region are determined using the automated region sorting method as described in Section 2.2.1.

Equation 2.2 is an upper limit of the growth rate for an observed event due to the assumption of an infinitely thin boundary, which is not true for the magnetopause. Equations 2.1 and 2.2 also assume an incompressible plasma, yet for very high ( $> 600$  km/s) solar wind speeds, the compressibility is generally sufficient to stabilize the development of the KHI. Due to these assumptions, the growth rate as determined by Equation 2.2 is an overestimate of the growth rate for an observed KHI. It must also be noted that MMS is unlikely to observe the source region of the KHI and local conditions may not match those of the source region. The difference in growth rate from the source region to the observation point is not predictable from observations.

In order to compare KHI events observed at various locations and under a variety of solar wind conditions and IMF orientations, we make the growth rate unitless via normalization to the local fast mode speed,  $v_{fm} = \sqrt{v_A^2 + c_s^2}$ . Both magnetic tension and compressibility have stabilizing effects on the KHI. Likewise, the fast mode speed is dependent on magnetic tension via the Alfvén velocity,  $v_A$ , and compressibility via the sound speed,  $c_s$ . Further, *Miura and Pritchett* [1982] showed the KHI growth rate is strongly correlated to the fast mode speed, and the KHI is stabilized if  $Q/k > v_{fm}$ . Thus it is more physically meaningful to normalize to the fast mode speed than another characteristic speed.

It is also important to note, our expression of the fast mode speed here is an upper limit which assumes the magnetic field is perpendicular to the bulk velocity. When the field and velocity are parallel, the larger of the sound or Alfvén speed is used as the fast mode speed. This means the unitless growth rate we present is a lower bound, and may be larger depending upon the relative geometry of the magnetic field and bulk velocity.

The fast mode speed is not equal in the magnetosheath (sub-index *msh*) and magnetosphere (sub-index *msh*), so we normalize to the mean of the two, such that

$$Q_{unitless} = \frac{Q/k}{v_{fm}}$$

where  $v_{fm} = (v_{fmmsh} + v_{fmmsh})/2$ .

In Equation 2.2 the direction of  $\hat{\mathbf{k}}$  is chosen to maximize the normalized growth rate, but many directions of  $\hat{\mathbf{k}}$  may satisfy the instability criterium. This range of wave vector directions capable of satisfying the instability criterium can be used to

determine just how susceptible a region is to the development of the KHI.

The KHI may propagate in any direction  $\hat{\mathbf{k}}$  for which  $Q/k$  is real (the right hand side of Equation 2.2 is positive under the square root). If we express  $\hat{\mathbf{k}}$  in terms of the spherical angles  $\phi$  and  $\theta$ , the percent of the  $4\pi$  solid angle that satisfies the KHI instability criterium at a given location may be calculated. We term this percentage the “unstable solid angle” [Burkholder et al., 2020; Nykyri et al., 2021b]. Figure 2.7 is a visualization of the unstable solid angle for the example KH event on 26 September 2017. On the total  $4\pi$  solid angle sphere, blue points indicate directions which are unstable to the development of the KHI. Events with larger unstable solid angles are likely to be KHI.

The growth rate, unitless growth rate, and unstable solid angle all help characterize an observed KH event. Chapter 3 reports the growth rate, unitless growth rate, and unstable solid angle for all 45 KH events observed by MMS between September 2015 and March 2020.

## 2.2.2 Kinetic Scale Wave Analysis Tools

### Variance Analysis

Though MMS data is typically reported in GSE or GSM coordinates, it is often useful to rotate the data into coordinate systems dependent upon the local boundary geometry. Boundary normal, or LMN, coordinate systems consist of three orthonormal vectors: one vector,  $\mathbf{N}$ , normal to the boundary and two vectors,  $\mathbf{L}$  and  $\mathbf{M}$ , tangential to it. Boundary normal coordinates are determined using variance analysis. The general method of variance analysis techniques is given in *Sonnerup and Scheible* [1998]. In this work, we make use of two forms of variance analysis: maximum variance anal-

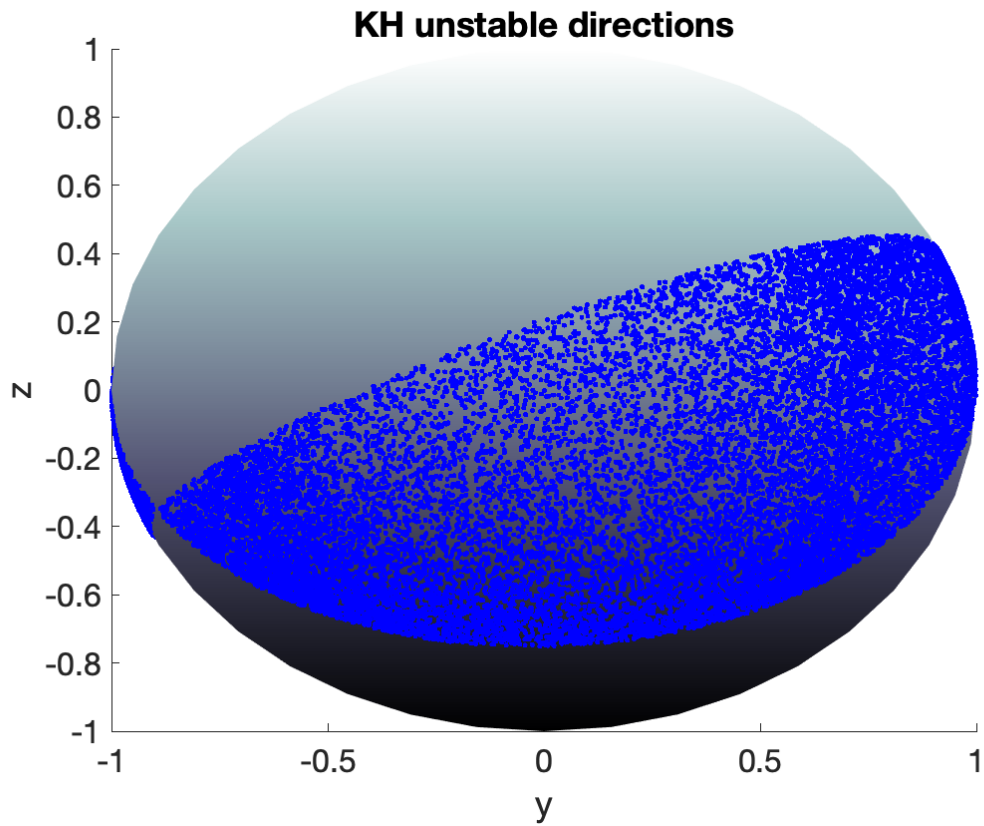


Figure 2.7: The unstable solid angle is the fraction of the total  $4\pi$  solid angle sphere which can support the growth of the KHI. The directions in which the KHI is able to grow are shown in blue for the September 26 2017 event.

ysis of the electric field (MVA-E) and minimum variance analysis of the magnetic field (MVA-B).

The MVA-E technique is used to determine the unit vector,  $\mathbf{N}$ , normal to the magnetopause boundary at which the KHI is operating. A variance matrix is constructed from the convective electric field,  $\mathbf{E} = -\mathbf{v} \times \mathbf{B}$ . The direction of maximum variance of the field is determined as an eigenvalue problem of the variance matrix. The direction of maximum variance is defined by the maximum eigenvector of the variance matrix and corresponds to  $\mathbf{N}$ . Directions tangential to the boundary correspond to the intermediate and minimum eigenvectors. The MVA-E technique is used when determining the “global” normal of the boundary during an observation of the KHI. The normal component of the magnetic field,  $B_N$ , in which KH waves create bipolar signatures, is calculated using the MVA-E method.

The MVA-B technique follows a similar procedure. A variance matrix is constructed from the measured magnetic field, and solved as an eigenvalue problem. In this case, the normal direction is the direction in which the variance is minimized, i.e. the direction of the minimum eigenvector of the variance matrix. The tangential directions correspond to the intermediate and maximum eigenvectors. In this work MVA-B is used to determine the direction of propagation for small scale waves. In this application, the minimum variance direction,  $B_{\min}$ , corresponds with the direction of the wave vector,  $\mathbf{k}$ . The intermediate and maximum variance directions,  $B_{int}$  and  $B_{\max}$  are tangential to the plane of the wavefront.

The quality of a boundary normal coordinate system is indicated by the ratio of the variance matrix’s eigenvalues. In MVA-E, the coordinate system is well defined if the ratio of the maximum and intermediate eigenvalues,  $\lambda_{\max}/\lambda_{int}$ , is large. For

MVA-B, the coordinate system is well defined if the ratio of the intermediate and minimum eigenvalues,  $\lambda_{int}/\lambda_{min}$ , is large. For the application of MVA-B to the wave field, eigenvalue ratios indicate how well polarized the wave may be. The statistical analysis of ion scale waves presented in Chapter 4 considers only well polarized wave intervals, such that  $\lambda_{int}/\lambda_{min} > 5$  and  $\sqrt{\lambda_{int}/\lambda_{max}} > 0.5$ .

It must be noted the normal direction identified using variance analysis techniques is subject to a  $180^\circ$  ambiguity. When used to determine the normal component of the magnetic field, we require the normal direction point outward from the magnetopause into the magnetosheath. When used to determine the direction of the wave vector, the  $180^\circ$  ambiguity cannot be resolved with a single spacecraft. It is possible to identify the exact wave vector direction if multiple spacecraft observe the same wave packet at different times, but such analysis is beyond the scope of the current work.

### Isolating Wave Fields

Generally, the electric and magnetic fields can be expressed as the sum of a steady background field and a component wave field,  $\mathbf{E} = \mathbf{E}_0 + \delta\mathbf{E}$ ,  $\mathbf{B} = \mathbf{B}_0 + \delta\mathbf{B}$ . There may be many wave fields, each at a different frequency. To isolate only the wave field near a certain frequency of interest, the ion cyclotron frequency for example, we use band pass filtering via a fast Fourier transform (FFT).

Consider the case in which we wish to isolate the wave field around the ion cyclotron frequency,  $f_{IC}$ . Over the course of a KH event,  $f_{IC}$  varies from  $f_{IC\min} = 2^j$  to  $f_{IC\max} = 2^k$  where  $j$  and  $k$  can be any number. The FFT requires frequency bounds which correspond to integer powers of 2, thus we select the bounds of the band pass filter such that  $f_{\min} = 2^{\lfloor j \rfloor - 1}$  and  $f_{\max} = 2^{\lceil k \rceil + 1}$ .



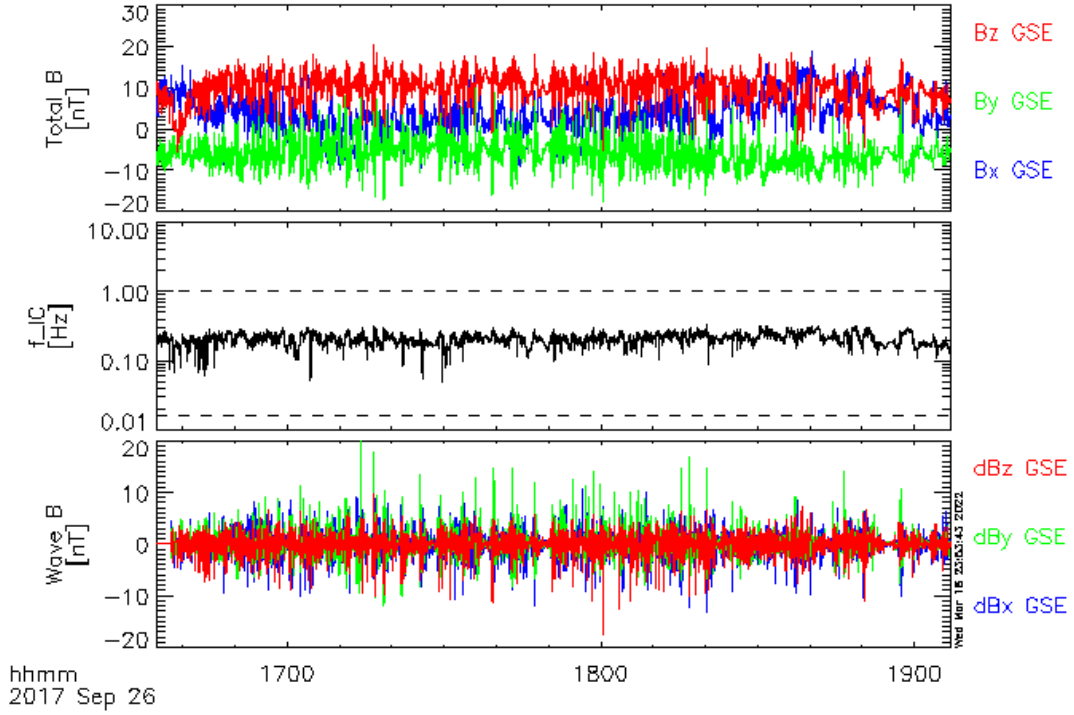


Figure 2.8: The total magnetic field, ion cyclotron frequency, and filtered wave magnetic field for the example event on 26 September 2017. Dashed lines indicate the upper and lower boundaries of the band pass filter used to isolate the wave field.

The selection of upper and lower bounds of the band pass filter for the example KH event observed on 26 September 2017 is depicted in Figure 2.8. For the example shown,  $f_{IC}$  varies from a minimum of  $f_{IC\min} = 0.049 = 2^{-4.34}$  Hz to a maximum of  $f_{IC\max} = 0.32 = 2^{-1.60}$  Hz. The bounds of the band pass filter, marked with dashed lines in Figure 2.8, are thus  $f_{\min} = 2^{[-4.34]-1} = 2^{-6} = 0.016$  Hz and  $f_{\max} = 2^{[-1.60]+1} = 2^0 = 1$  Hz. The total and filtered wave magnetic fields are also shown in Figure 2.8.

## Wave Mode Identification

Several characteristics of a wave may be used to identify its wave mode. We take advantage of a few, namely the wave frequency, the angle of wave propagation relative to the background magnetic field, the electromagnetic or electrostatic nature of the wave, and the ellipticity.

In this work, we search for waves only in a set frequency range, specifically waves about the ion cyclotron frequency. Therefore, the potential wave modes which we expect to observe are narrowed to the ion cyclotron wave, the kinetic Alfvén wave, and the kinetic magnetosonic wave. More details about the generation mechanisms, effects, and signatures of the wave modes near the ion cyclotron frequency are given in Chapter 4.

The direction at which observed waves propagate is determined using MVA-B analysis on the wave field, as described in section 2.2.2. The direction of minimum variance is in line with the wave vector,  $\mathbf{k}$ . Kinetic Alfvén waves tend to propagate parallel to the background field while the kinetic magnetosonic wave propagates perpendicular to the field.

Both the kinetic Alfvén and kinetic magnetosonic waves are electromagnetic waves in which oscillations of both the electric and magnetic field are present. We may determine if a wave is electromagnetic or not using the ratio of the wave electric and wave magnetic fields ( $\delta E/\delta B$ ). For electrostatic waves, oscillations of the electric field dominate and the ratio is greater than the Alfvén velocity i.e.  $(\delta E/\delta B)/v_A > 1$ . For electromagnetic waves, the ratio is less than the Alfvén velocity and  $(\delta E/\delta B)/v_A < 1$ .

Ellipticity describes the polarization of the observed wave field. Linearly polarized waves have ellipticity  $\epsilon = 0$ . Exactly circularly polarized waves have elliptic-

ity  $\epsilon = \pm 1$  depending on their handedness. Waves which rotate about the background magnetic field according to the right-hand rule are right-handed circularly polarized with ellipticity  $\epsilon = 1$ . Left-handed circularly polarized waves, with  $\epsilon = -1$ , obey the left-hand rule relative to the background magnetic field. Observations more typically have intermediate values of ellipticity. Ellipticity can be determined using hodograms, or calculated directly, using methods developed by *Krauss-Varban et al.* [1994]. Mathematically, ellipticity is the ratio of the right- and left-handed circularly polarized wave field powers:

$$\epsilon = \Re \frac{B_\xi - iB_y}{B_\xi + iB_y} \quad (2.3)$$

Where  $B_\xi$  and  $B_y$  are the components of the wave field perpendicular to the wave propagation direction. The determination of these components requires the rotation of the wave field into a coordinate system aligned with the wave vector. The unit vector  $\hat{\xi}$  is coplanar to both the wave vector direction,  $\hat{\mathbf{k}}$ , and the direction of the background magnetic field,  $B_{||}$ . Additionally,  $\hat{\xi}$  is perpendicular to the wave vector. The third unit vector direction completes the right-handed system such that  $\hat{\mathbf{k}} \times \hat{\xi} = \hat{\mathbf{y}}$  [*Krauss-Varban et al.*, 1994].

The kinetic Alfvén wave is polarized in the left-handed sense, as is the ion cyclotron wave [*Krauss-Varban et al.*, 1994]. The kinetic magnetosonic wave is right-handed polarized [*Krauss-Varban et al.*, 1994].

In conjunction with frequency, propagation direction, and  $\delta E/\delta B$  ratios, ellipticity is useful in classifying observations as consistent with a particular known wave mode. It is important to note, calculating ellipticity or frequency directly from spacecraft measurements will yield results in the spacecraft frame. The spacecraft, however, is

moving with respect to the field, and Doppler shift effects can play an important role. Large Doppler shift effects may even change the sign of an observed wave’s ellipticity, such that a wave appearing to be a right-handed in the spacecraft frame is truly left-handed (or vice-versa).

### Doppler Shift Effects

All MMS observations are made in the reference frame of the spacecraft as it moves through the plasma of the near Earth space. The observed waves, however, occur in the inertial plasma frame. The relative motion of the spacecraft and plasma frames means the wave properties, such as frequency and ellipticity, observed by MMS are not likely to be the true properties of the wave. We may account for some of this discrepancy by calculating the Doppler shifted frequency. The Doppler shift of angular frequency from the spacecraft to the plasma frame is described by Equation 2.4,

$$\omega_p = \omega_{sc} - \mathbf{k} \cdot \mathbf{v}_{\text{bulk}} \quad (2.4)$$

where  $\omega_p$  and  $\omega_{sc}$  are the angular frequency in the plasma and spacecraft frames, respectively,  $\mathbf{k}$  is the wave vector, and  $\mathbf{v}_{\text{bulk}}$  is the bulk plasma velocity. The direction of the wave vector is determined using MVA-B analysis (see Section 2.2.2). The magnitude of the wave vector is dependent upon the wave mode, though for waves near the ion cyclotron frequency, the thermal ion gyroradius is a reasonable estimate.

A full account of the Doppler shift effects on ellipticity is dependent upon the perpendicular and parallel components of the wave vector and each wave mode’s unique dispersion relation. This work is ongoing (see Chapter 5).

## 2.3 MHD Simulations

### MHD Theory

In the magnetohydrodynamic (MHD) description, plasma is treated as a fluid made of several species of particles, though species are typically limited to protons and electrons for magnetospheric space plasmas. Like a normal fluid, the plasma must obey the laws of hydrodynamics, i.e. the conservation of mass and momentum via the continuity equation, 2.5 and the momentum equation, 2.6.

$$\frac{\partial \rho}{\partial t} + \nabla \cdot \rho \mathbf{v} = 0 \quad (2.5)$$

assuming no sources or losses;

$$\frac{\partial(\rho \mathbf{v})}{\partial t} + \nabla \cdot \rho \mathbf{v} \mathbf{v} = -\nabla p \quad (2.6)$$

where the very small the electron mass is considered negligible

However, because plasma is made of charged particles with an embedded magnetic field, the velocity and density cannot be arbitrarily specified as they could be for an unmagnetized fluid. Consider a magnetized, quasi-neutral plasma in which a new set of particles is introduced with an arbitrary velocity. The new particles' velocity is effected by the magnetic field via the Lorentz force. The change in particle motion induces a current, which in turn affects the magnetic field. The velocity and magnetic field are co-dependent, therefore we must develop a self-consistent set of equations to describe the fluid motion and field behavior of the plasma. This system of equations combines the continuity and momentum equations of hydrodynamics with Maxwell's

Equations governing electric and magnetic fields (2.7-2.9) along with the Generalized Ohm's Law (2.10).

$$\frac{\partial \mathbf{B}}{\partial t} = -\nabla \times \mathbf{E} \quad (2.7)$$

$$\nabla \times \mathbf{B} = \mu_0 \mathbf{J} \quad (2.8)$$

$$\nabla \cdot \mathbf{B} = 0 \quad (2.9)$$

$$\mathbf{E} + \mathbf{v} \times \mathbf{B} = \eta \mathbf{J} + \frac{\mathbf{J} \times \mathbf{B}}{en} + \frac{\nabla \cdot \mathbf{P}}{en} + \frac{m_e}{e} \frac{dv_e}{dt} \quad (2.10)$$

However, in the ideal MHD description, we treat the plasma as fluid and ignore the smaller scale behavior of single particles (i.e. the ion and electron inertial scales). Thus the Generalized Ohm's law is reduced to

$$\mathbf{E} + \mathbf{v} \times \mathbf{B} = 0 \quad (2.11)$$

The ideal MHD description relies on several assumptions for its validity. For example, ideal MHD only applies when the time and length scales under consideration are much greater than the characteristic scales (e.g: the gyroradius for length and inverse of the plasma frequency for time). Ideal MHD also assumes the plasma has infinite conductivity. For infinitely conductive plasmas the magnetic field is “frozen” into the fluid. In short, ideal MHD describes the plasma as a fluid and is entirely dependent on the bulk properties. At small scales where particle motion is dominant,

or the if the frozen in condition is violated, ideal MHD will no longer hold. For this reason, we can study the fluid scale KHI via ideal MHD simulation and approximation, but not the small scale waves associated with the KHI.

The ideal MHD description is not capable of resolving many important processes in space plasma which occur at smaller scales, such as reconnection, which requires the violation of the frozen in condition. In order to capture small scale processes, ideal MHD is often modified to include terms on the right hand side of the generalized Ohm's law. Common modifications of MHD include Hall-MHD and resistive MHD.

In Hall-MHD, the Hall term, which describes the effects of currents perpendicular to the background field, is preserved. Ohm's law for Hall-MHD is

$$\mathbf{E} + \mathbf{v} \times \mathbf{B} = \frac{\mathbf{J} \times \mathbf{B}}{en} \quad (2.12)$$

The resistivity term may also be included to yield Hall-MHD with anomalous resistivity, in which Ohm's Law is

$$\mathbf{E} + \mathbf{v} \times \mathbf{B} = \eta \mathbf{J} + \frac{\mathbf{J} \times \mathbf{B}}{en} \quad (2.13)$$

The Hall and resistivity terms are able to support smaller scale process than the ideal MHD description. This work makes use of resistive Hall-MHD simulations, as described in the following section.

## **Application of MHD Simulations**

To verify the automated region sorting method developed in section 2.2.1 was truly robust, it was applied to parameters generated by 2 dimensional Hall-MHD simula-

tions of the KHI. A simulation case for the KHI developing under northward IMF (NIMF) orientation was initiated using conditions comparable to those of the KH event observed on 08 September 2015. A second simulation of the KHI developing during Parker Spiral IMF (PSIMF) orientation was created using initial conditions similar to those of the event observed on 18 October 2015.

The simulations, after *Ma et al.* [2019], solve the full set of resistive Hall-MHD equations using a leapfrog scheme [*Potter*, 1973; *Birn*, 1980; *Otto*, 1990]. All physical quantities are normalized to their typical scale. Length,  $L$ , is normalized to the half width of the initial shear flow,  $L_0$ ; number density,  $n$ , to  $n_0$ ; the magnetic field,  $B$ , to  $B_0$ ; velocity,  $v$  to the Alfvén velocity,  $v_A = B/\sqrt{\mu_0\rho_0}$ ; and time,  $t$ , to the Alfvén transit time,  $T_A = L_0/v_A$ . Exact values of the normalizations for both simulation cases are listed in Table 2.4.

Table 2.4: Normalization constants for the 2D MHD simulations.

Quantity	Northward	Parker spiral
Magnetic field $B_0$ (nT)	71.5	30.23
Number Density $n_0$ (/cc)	12.36	2.78
Length scale $L_0$ (km)	640	640
Velocity $V_A$ (km/s)	443	395.21
Time $t_0$ (s)	1.35	1.62

As shown in Figure 2.9, a cut is taken through the simulation box at every time step, simulating the way a spacecraft would move through the KHI at the magnetopause. Data recorded along the cut is separated into magnetospheric and magnetosheath regions using the automated region sorting method. Plasma parameters in the identified regions agreed well with the known values. The density in each region at every time step of the simulation can be seen in Figure 2.9. For the duration of a simulation of NIMF conditions, the automated region sorting produces a density



within 0.15 /cc of the known values in either region. The automated method yields density values within 0.3 /cc of the known values for a simulation under PSIMF conditions. This indicates the automated region sorting method works well, even for late stages of the KHI with significant mixing.

Simulations also underscore the dependence of the region sorting method on the path of the spacecraft through the observation (or the geometry of the cut in simulation space). Four cuts with different geometries were taken at each time step: one perpendicular to the boundary, one oblique to the boundary, one parallel to the boundary on the magnetosheath side, and one parallel to the boundary on the magnetospheric side, as can be seen for the PSIMF simulation on the left of Figure 2.10. The automated region sorting method was applied to data from each of the cuts and used to calculate plasma parameters for each region. The density in both regions is plotted on the left of Figure 2.10 along with the known value. The perpendicular and oblique cuts match the known value throughout the simulation. As discussed previously, the regions identified from the oblique cuts are, at worst, within 0.3 /cc with the known density for each region (see Figure 2.9). The perpendicular cut produces comparable results to the oblique cut. The parallel cuts, as expected, do not isolate regions matching with known values until they observe both regions. As the instability develops, and more plasma from both regions is captured by the cut, the results improve drastically, as can be seen between simulation time steps 150 and 200 in Figure 2.10. Prior to this point, each parallel cut yields density values similar to the region it is in for both regions. After time step 200, the boundary has been twisted enough that the parallel cuts observe significant amounts of plasma associated with both regions, and the automated region sorting method yields much better results.

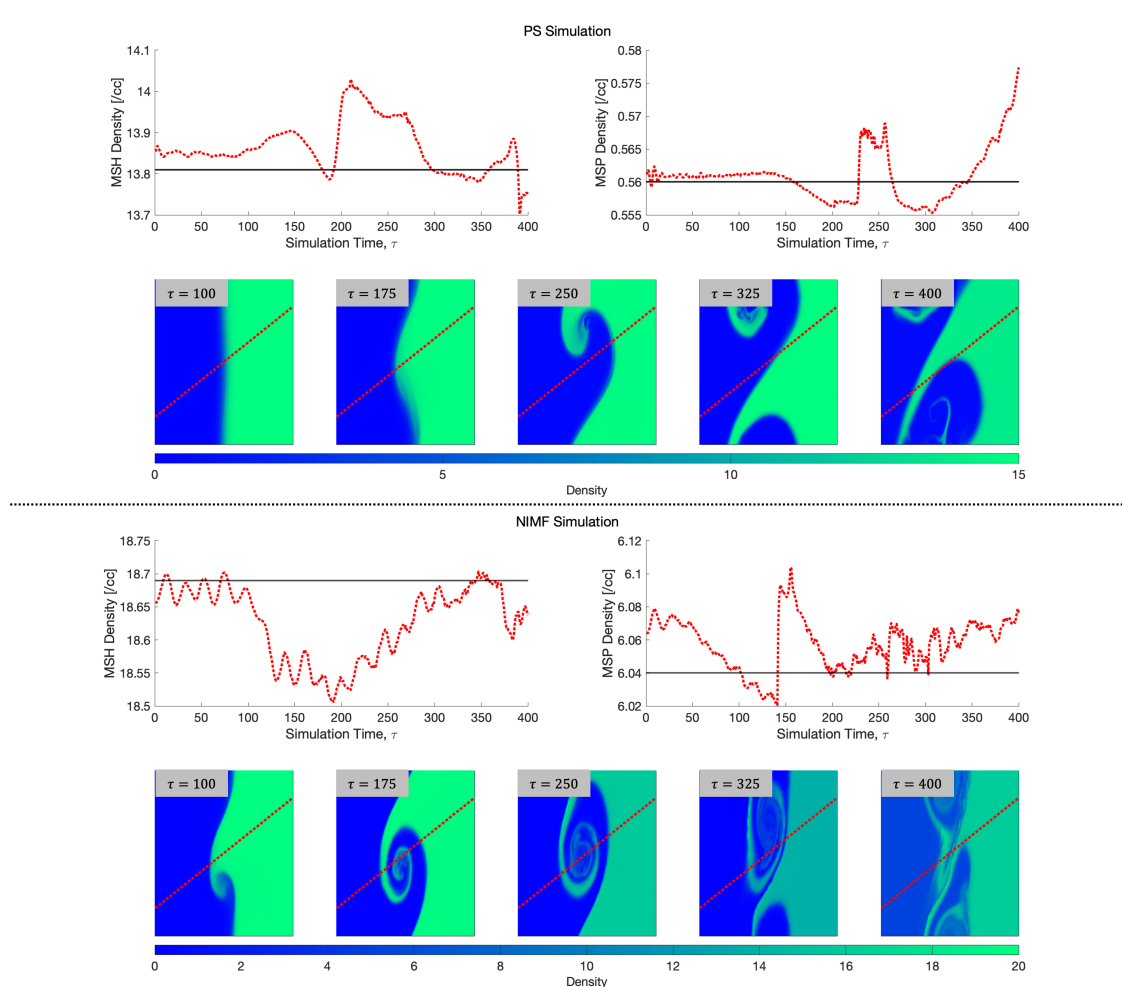


Figure 2.9: The automated region sorting method yields regions in which measured density (red, dashed lines) agrees well with the known value (black, solid lines) even as the simulations develop and the plasma is mixed.

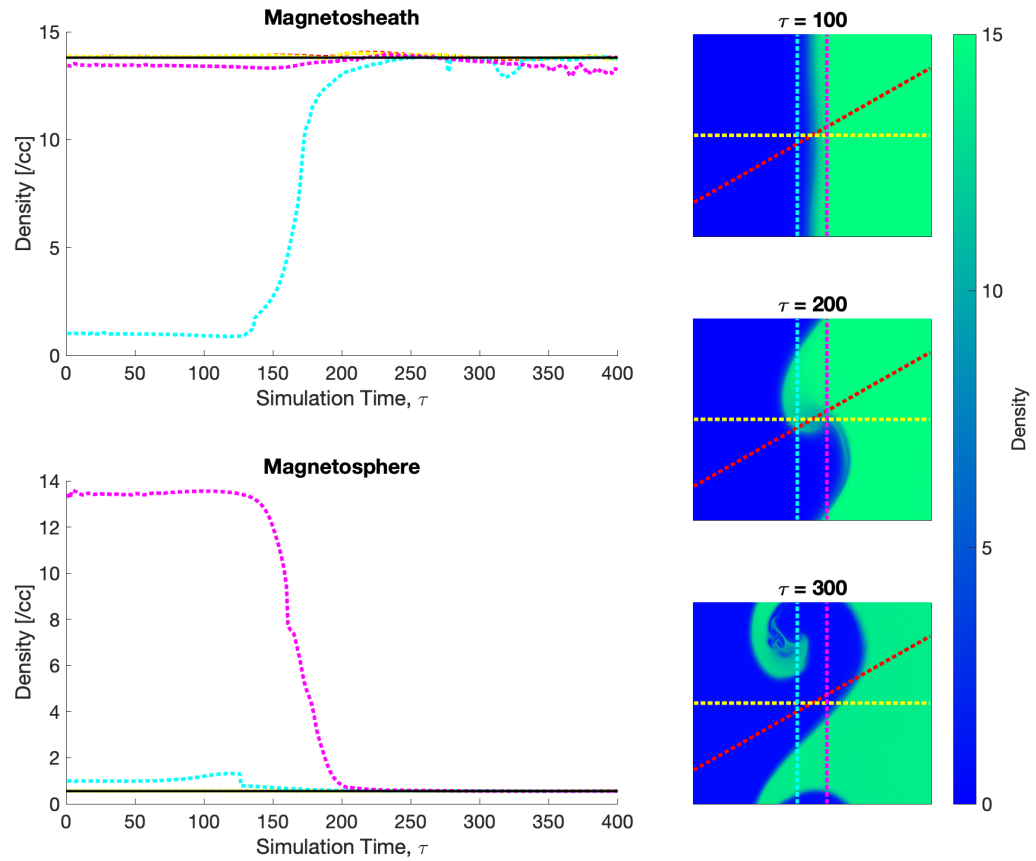


Figure 2.10: The results of the automated region sorting method depend on cut geometry in simulation space. Cuts which spend significant portions of the event on both sides of the boundary produce the best results. The known density value for each region is indicated by the solid black line, the measured densities are indicated by dashed lines with colors corresponding to the cut geometries shown on the right.

## 2.4 Conclusions

Based on the signatures described in Section 2.2.1, we identified 45 MMS observations within the MMS data. Initial analysis indicates these observations are well distributed along the magnetopause and span the full range of IMF orientations. More details about the large scale properties of the KHI are presented in Chapter 3.

A new automated region sorting technique was developed to aid in the characterization of the KH events observed by MMS. This technique uses specific entropy,  $S = T/n^{2/3}$ , and  $nv_{tail}/T$  to isolate pure magnetosphere and pure magnetosheath plasma, respectively. When the new technique was tested on simulated data, the resulting plasma regions were in excellent agreement with known properties of the simulation. Comparison with a previous region sorting method from *Moore et al.* [2017] shows general agreement in the resulting regions, but the new method better selects the most pure magnetosheath and magnetospheric plasma. The newly developed method also has the benefit of being fully automated.

The kinetic scale wave analysis described in this Chapter is used to isolate well polarized wave intervals within the KHI. Chapter 4 details the results of that analysis.

# Chapter 3

## Statistical Results of KHI Properties

The results presented in this chapter are published in *Rice et al.* [2022].

### 3.1 KHI Growth Rates and Unstable Solid Angles

The 45 KHI events observed by MMS were sorted into regions of magnetosheath, mixed, and magnetospheric plasma using the method described in Section 2.2.1. In order to characterize and compare the KHI observations, the growth rate, unitless growth rate, and unstable solid angle of each event were calculated as described in Section 2.2.1. The results of these calculations are listed in Table 3.1.

Growth Rate ranges from 3.93 km/s to 103.16 km/s. When normalized to the local fast mode speed, unitless growth rate ranges from 0.005 to 0.325, but is more typically between 0.010 and 0.200. That is, the KHI typically develops at 1 to 20% of the local fast mode speed; only eight events fall outside this range (seven below

and one above).

Unstable solid angle ranges from 0.06 to 39.51%. Two of the events have unstable solid angles less than 1% of the total  $4\pi$  solid angle. Unstable solid angle is between 1% and 10% for 23 events, and between 10% and 25% for 17 events. Three events have unstable solid angles greater than 25% of the total  $4\pi$  solid angle.

At its maximum, the normal component of the velocity often accounts for more than 60%, and occasionally all, of the total velocity, indicating the observed KH waves have significantly twisted the boundary.

Table 3.1: Growth rates (GR), unitless growth rates (UGR), unstable solid angles (USA), and the relative value of the maximum normal velocity component for each of the 45 KHI events observed by MMS from September 2015 to March 2020.

Event No.	Date	GR [km/s]	UGR	USA [%]	$v_{Nmax}/v_{tot}$
01	08-Sep-15	81.63	0.081	6.37	0.96
02	15-Sep-15	16.27	0.019	0.82	0.99
03	11-Oct-15	15.68	0.016	0.42	0.58
04	15-Oct-15	8.83	0.007	0.11	0.85
05	17-Oct-15	25.05	0.032	4.01	0.92
06	18-Oct-15	52.31	0.063	9.07	0.83
07	22-Dec-15	10.41	0.010	0.29	0.83
08	11-Jan-16	17.47	0.015	0.27	0.89
09	19-Jan-16	13.78	0.025	0.12	0.52
10	05-Feb-16	22.31	0.028	5.74	0.93
11	07-Feb-16	13.36	0.019	0.16	0.66
12	18-Feb-16	34.90	0.038	8.96	1.00

Continued on next page

Table 3.1: Continued from previous page

Event No.	Date	GR [km/s]	UGR	USA [%]	$v_{Nmax}/v_{tot}$
13	25-Feb-16*	5.01	0.012	0.08	0.69
14	26-Sep-16	51.46	0.068	7.26	0.99
15	27-Sep-16	84.07	0.117	8.37	0.96
16	04-Oct-16	54.67	0.063	7.17	0.70
17	10-Oct-16	43.30	0.059	8.98	0.75
18	24-Oct-16	3.93	0.005	0.06	0.71
19	04-Nov-16	16.78	0.019	0.78	0.95
20	03-May-17	56.65	0.197	39.51	0.85
21	08-May-17	84.15	0.278	29.87	1.00
22	11-May-17	45.56	0.103	12.07	0.87
23	11-May-17	49.99	0.198	13.33	0.33
24	19-May-17	90.54	0.186	29.00	0.93
25	20-May-17	47.42	0.066	30.22	0.75
26	20-Sep-17	53.99	0.145	18.75	0.19
27	26-Sep-17	52.01	0.189	24.23	0.83
28	16-Oct-17	26.03	0.047	6.74	0.79
29	30-Oct-17	11.51	0.023	4.70	0.97
30	02-Nov-17	39.55	0.109	5.95	0.67
31	03-May-18	95.59	0.325	23.37	0.97
32	18-Sep-18	40.87	0.090	9.96	0.91
33	24-Sep-18	71.16	0.227	36.91	0.73

Continued on next page

Table 3.1: Continued from previous page

Event No.	Date	GR [km/s]	UGR	USA [%]	$v_{Nmax}/v_{tot}$
34	02-Oct-18	41.17	0.111	10.18	0.65
35	04-Oct-18	31.26	0.081	6.16	0.50
36	13-Apr-19	48.93	0.089	15.66	0.76
37	03-Jun-19	42.25	0.108	16.63	0.94
38	25-Sep-19	74.22	0.198	28.04	0.91
39	02-Oct-19	29.28	0.083	6.10	0.58
40	02-Oct-19	96.46	0.209	26.71	0.82
41	02-Oct-19	37.12	0.111	18.09	0.52
42	06-Oct-19	82.43	0.210	34.49	0.98
43	15-Oct-19	94.08	0.296	18.37	0.98
44	22-Oct-19	52.52	0.110	12.00	1.00
45	12-Nov-19	103.16	0.250	14.34	0.90

A few of the observed events occur in apparently stable regions with very low growth rates (e.g: the high-latitude case on 25 Feb 2016 [*Nykyri et al.*, 2021b; *Michael et al.*, 2021]). This does not preclude the observed events from being the KHI. Convective instabilities, like the KHI, dissipate energy stored in unstable regions and systems. As excess energy is dissipated, the region becomes more stable, therefore maximum instability and growth rate occur just prior to the formation of the instability. Because it is difficult to identify the KHI in observational data until it is relatively well developed and has dissipated some of the excess free energy, observations will only be made after growth rate has decreased from its maximum. We believe those



events occurring in apparently more stable regions may be later in development than faster growing KHI in less stable areas.

We also note the path MMS takes through the KHI event can have a significant effect on the growth rate determination, as discussed in Sections 2.2.1 and 2.3. Encounters which skim the KH vortex rather than passing directly through it may grow faster than our calculations would indicate.

## 3.2 Solar Wind and IMF During the KHI

The IMF orientations for which KHI are observed are compared with those observed for the entirety of the 4.5 year interval from September 2015 to March 2020. OMNI data is available for 44 of the 45 KH events observed by MMS and is listed in detail in Appendix A. As can be seen in Figure 3.1, the IMF magnitude and orientations during KHI observations match well with the distribution of observations for the full 4.5 year interval. KHI are observed slightly less than expected for the most common IMF magnitude, and more than expected for very large IMF. This is due to a single outlier event which occurred during  $IMF \approx 20$  nT [Eriksson *et al.*, 2016]. The planar,  $B_X$  and  $B_Y$ , components of the IMF show no conclusive variation in the KHI observations relative to the complete 4.5 year interval. However, northward IMF is more common during KHI observations than for the full time range. Southward IMF is correspondingly less common during KHI intervals than otherwise. This is likely due to subsolar reconnection during southward IMF, which creates a more diffuse boundary layer which is less prone to the development of the KHI.

Solar wind conditions for the KH observations cover the full range of typical

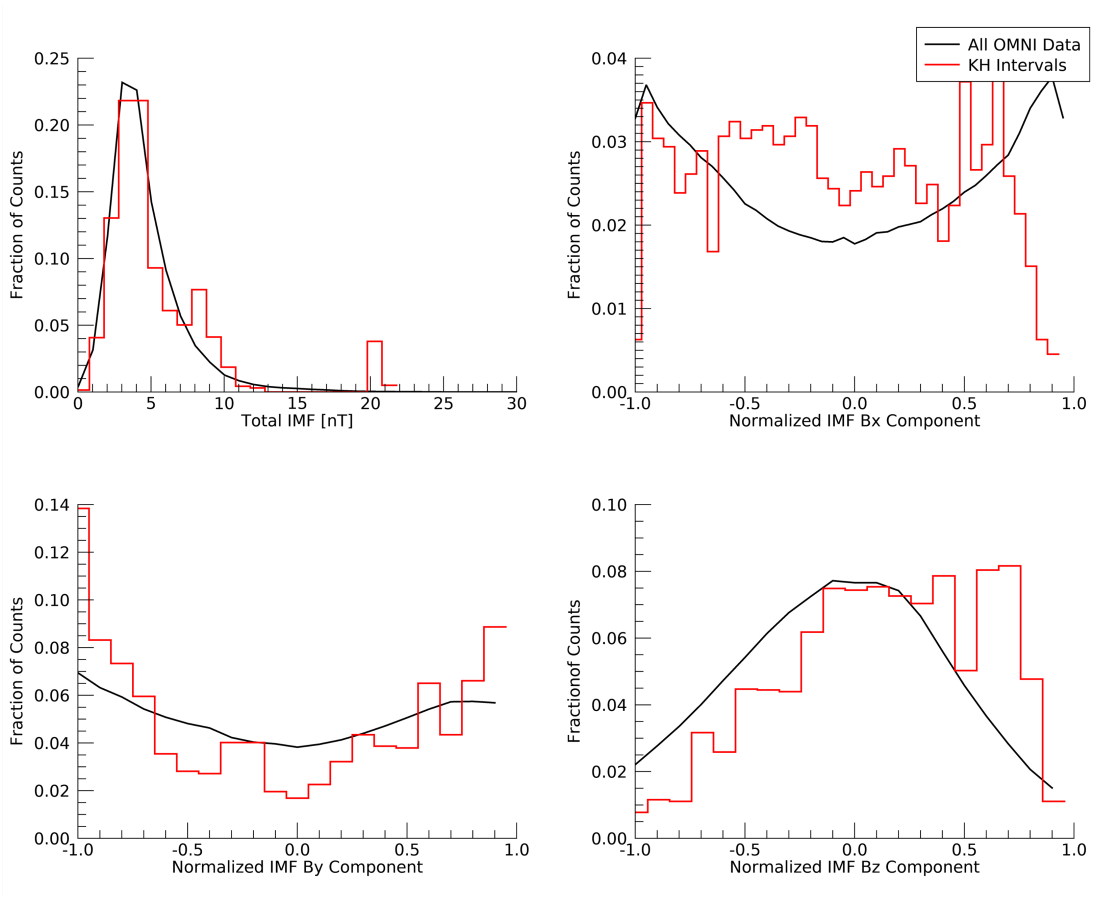


Figure 3.1: The normalized distributions of IMF strength and normalized IMF components for KHI observations (red) and the full 4.5 year interval from September 2015 to March 2020 (black) are similar, though the KHI occurs more frequently when the  $B_z$  component is positive.

parameters, as can be seen in Figure 3.2. The distribution of solar wind density, temperature, flow speed, and Alfvén mach number during KHI observations generally agree with the distributions for the full 4.5 year interval from September 2015 to March 2020. The most pronounced discrepancy is in solar wind flow speed: KHI observations overrepresent high solar wind speeds, particularly between 350 and 450 km/s. This is unsurprising, as the KHI develops preferentially for high ( $> 400$  km/s) solar wind speeds while magnetic compressibility at very high speeds ( $> 600$  km/s) can have a stabilizing effect.

While the KHI occurs for the full range of solar wind conditions and IMF orientations, the solar wind and IMF have no apparent effect on the KHI growth rate, unitless growth rate, or unstable solid angle. Figure 3.3 plots the growth rate, unitless growth rate, and unstable solid angle of 44 of the 45 KHI observations as functions of solar wind density, temperature, flow speed, Alfvén Mach number, and IMF magnitude. The color bar indicates the event number (listed in both Tables 2.2 and 3.1) so each event is plotted with the same color across all plots for direct comparison. No correlation is apparent between growth rate, unitless growth rate, or unstable solid angle and any of the solar wind and IMF parameters, with the exception of solar wind flow speed, in which there appears to be a selection window between 295 and 610 km/s.

The apparent selection window in solar wind flow speed fits with expectations that low velocity shears between the magnetosheath and magnetosphere are not unstable to the KHI and compressibility effects for very large shears stabilize the KHI [*Miura and Pritchett, 1982*]. However, the distribution of solar wind speeds for the 4.5 year interval from September 2015 to March 2020 shown in Figure 3.2 indicates the solar

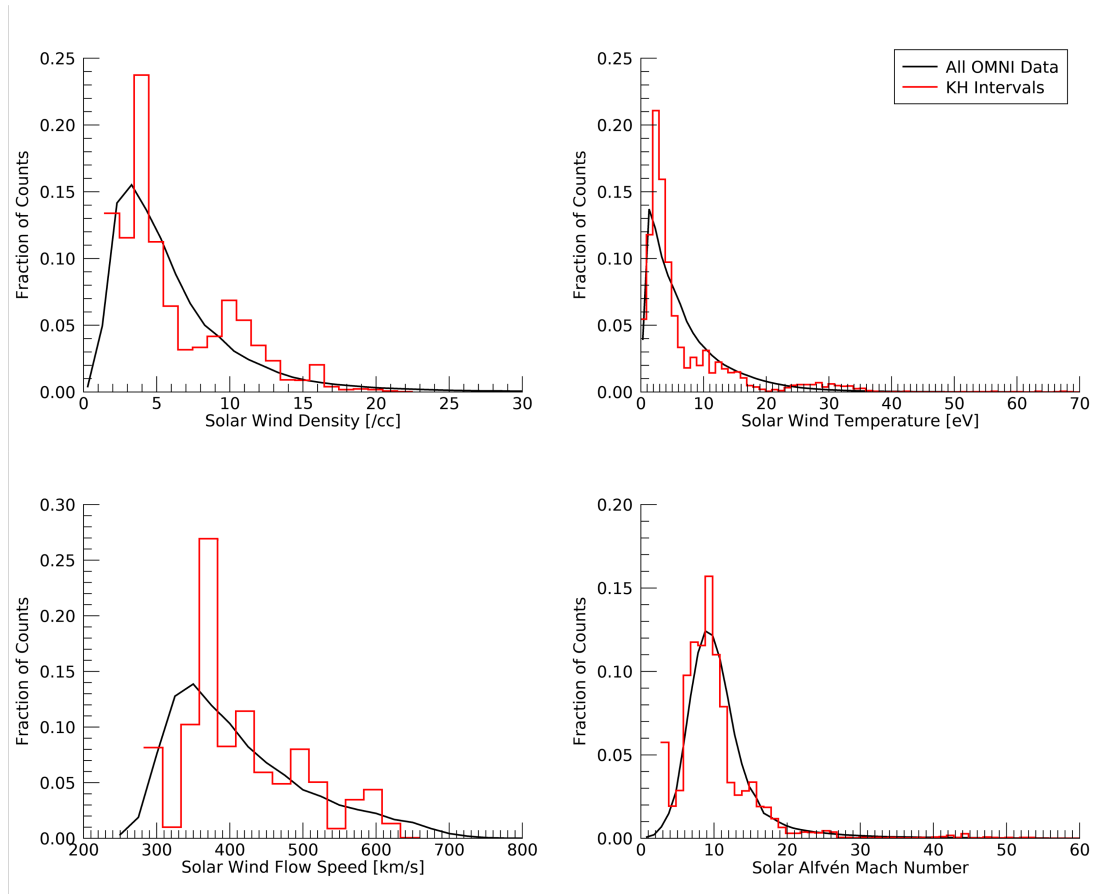


Figure 3.2: Normalized distributions of solar wind density, temperature, flow speed, and Alfvén Mach number for KHI observations (red) and the full 4.5 year interval from September 2015 to March 2020 (black) are generally similar, though the KHI observations overrepresent solar wind speeds between 350 and 450 km/s.

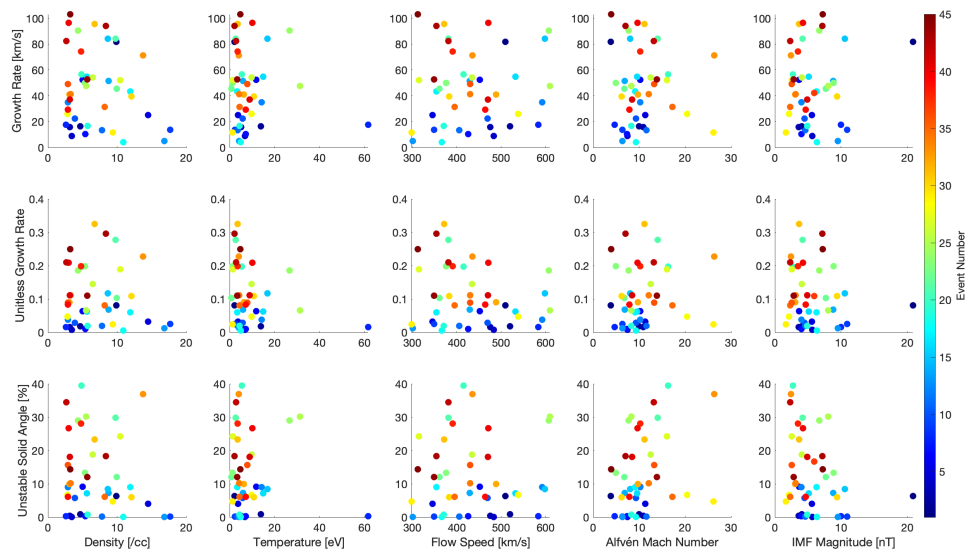


Figure 3.3: KHI growth rate (top), unitless growth rate (middle), and unstable solid angle (bottom) as functions of solar wind density (far left), temperature (center left), flow speed (center), Alfvén Mach number (center right), and IMF magnitude (far right). There is no obvious correlation between KH characteristics and solar wind conditions

wind speed is rarely below 300 km/s or above 600 km/s. Therefore, the apparent selection window is likely not significant.

### 3.3 KHI Observation Locations

The KHI growth rate, unitless growth rate, and unstable solid angle show some dependence on location. Figure 3.4 plots the location of the 45 MMS observations of the KHI in the GSM  $X$ - $Y$ ,  $X$ - $Z$ , and  $Y$ - $Z$  planes. Growth rate, unitless growth rate, and unstable are indicated by the color bars for each row. The KHI observations near the subsolar point tend to have lower growth rate than those observed farther along the tail. This trend is still apparent even when growth rate are normalized to the local fast mode speeds. This is likely due to the low velocity shear near the subsolar point. Immediately after encountering the bow shock, magnetosheath plasma is slowed significantly from solar wind speeds, and the shear between the sheath and the magnetosphere is much lower than farther downtail, where the magnetosheath plasma has accelerated and returned to solar wind velocity. The low velocity shear near the subsolar point will yield lower growth rates and unitless growth rates, as can be seen from Equation 2.2.

Unstable solid angle shows a similar pattern; larger values are observed farther downtail. Again, this is explained by the large velocity shears encountered along the tail magnetopause. On the dayside, the shocked solar wind of the magnetosheath is still accelerating back up to solar wind speed after encountering the obstacle of Earth's magnetosphere and bow shock, therefore velocity shears between the sheath and magnetosphere are smaller. Farther downtail the magnetosheath plasma has re-

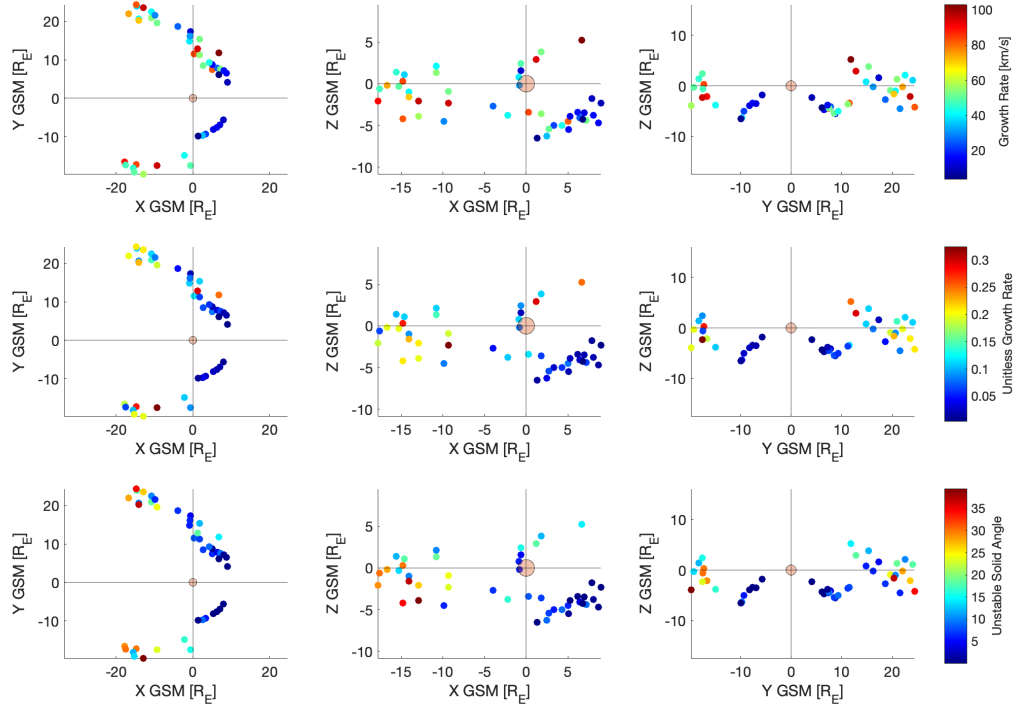


Figure 3.4: KHI growth rate (top), unitless growth rate (middle), and unstable solid angle (bottom) with respect to the KHI's observation location in the GSM  $X$ - $Y$  (left),  $X$ - $Z$  (center), and  $Y$ - $Z$  (right) planes. KH events occurring farther downtail tend to grow faster and in less stable regions.

achieved solar wind flow speed, increasing the shear between the two regions. For larger velocity shears, the stabilizing effects of the magnetic field are less influential in the development of the KHI, and a larger solid angle is unstable to the growth of the KHI.

A cluster of KHI observations were made at high southern magnetic latitudes (GSM  $Z \leq -4.5 R_E$ ), show the KHI is not limited to the lower equatorial latitudes. This is a new finding as previous missions, such as THEMIS, remained at lower magnetic latitudes. Only three prior observations, two made by Cluster [*Hwang et al.*, 2012; *Ma et al.*, 2016] and one made by MMS [*Nykyri et al.*, 2021a; *Michael et al.*, 2021], have been studied as examples of the KHI at high latitudes near the flanks of the magnetospheric cusp.

### 3.4 Conclusions

The main conclusions of the statistical study of fluid scale KHI properties may be summarized as follows.

- The automated region sorting method developed in Chapter 2 was used to isolate regions of magnetosheath and magnetospheric plasma for the 45 KHI events observed by MMS. Plasma parameters from each region were used to calculate KHI growth rate, unitless growth rate, and unstable solid angle for the 45 events in our database.

Growth rates, unitless growth rates normalized to the local fast mode speed, and unstable solid angles for the 45 KHI events in our database are reported in Table 3.1.



Growth rates range from a minimum of 3.93 km/s to a maximum of 103.16 km/s. When normalized to the fast mode speed, the unitless growth rate ranges from 0.005 to 0.325 in the extremes, with most events in the 0.01 to 0.20 range. That is, most of the observed KHI grow at speeds between 1% and 20% of the local fast mode speed. Increased growth rates and unitless growth rates are usually observed farther downtail where the velocity shear between the magnetosphere and magnetosheath is larger than on the dayside.

Two of the observed KHI have unstable solid angles less than 1% of the total  $4\pi$  solid angle. Unstable solid angles are between 1% and 10% for 23 events, and between 10% and 25% for 17 events. Three events have unstable solid angles greater than 25% of the total  $4\pi$  solid angle. Larger solid angles are more common farther down tail where the velocity shear from the magnetosheath to the magnetosphere is greater and thus the stabilizing effects of the magnetic field are less influential.

We note a few of the observed events occur in apparently stable regions with very low growth rates, but these events are still likely to be the KHI. Convective instabilities, like the KHI, dissipate energy stored in unstable regions and systems. As excess energy is dissipated, the region becomes more stable, and growth rate and unstable solid angle will decrease. Growth rate and unstable solid angle are maximized just prior to the formation of the instability. Identification of the KHI in observational data is difficult until it is relatively well developed and has dissipated some of the excess free energy. Therefore, observations will most likely be made after growth rate and unstable solid angle have decreased from their maxima. We believe those events occurring in apparently more stable regions may be later in development than faster growing KHI in less stable areas.

We also note the path MMS takes through the KHI can have a significant effect on the calculated growth rate. Encounters which merely skim the KH vortex rather than passing directly through it may actually grow faster than our calculations would indicate.

- The KHI is observed for the full range of solar wind conditions and IMF orientations. Growth rate, unitless growth rate, and unstable solid angle show no obvious correlation to solar wind conditions or IMF strength. An apparent selection window in solar wind flow speed is likely insignificant.

Values of the growth rate, unitless growth rate, and unstable solid angle for each event are listed in Table 3.1. As can be seen in Figure 3.3, growth rate, unitless growth rate, and unstable solid angle appear to be independent of solar wind conditions, with the exception of solar wind flow speed. All of the observed events occurred when the solar wind speed was between 295 km/s and 610 km/s. At flow speeds much below 295 km/s, the velocity shear is too low to satisfy the KHI onset condition (Equation 2.1). At solar wind speeds above 610 km/s magnetic compressibility will usually stabilize the KHI [*Miura and Pritchett, 1982*]. Within this selection window between 295 km/s and 610 km/s, however, flow speed is not correlated with growth rate, unitless growth rate, or unstable solid angle. Additionally, as can be seen in Figure 3.2, this selection window likely reflects the distribution of solar wind speed throughout the entire 4.5 year time range considered in this study, and is thus insignificant.

While the KHI was observed for the full range of IMF orientations, positive  $B_Z$  components are overrepresented during KH events when compared with observations for the entire 4.5 year interval from September 2015 to March 2020. This is in line with expectations, as IMF orientations with a negative  $B_Z$  component may trigger

subsolar reconnection, creating a more diffuse boundary layer which is less prone to the development of the KHI.

- KHI observations are well distributed along the magnetopause. Growth rates, unitless growth rates, and unstable solid angles are consistently larger along the tail magnetopause than on the dayside flanks.

The MMS made more observations of the KHI on the dusk flank (29) than on the dawn (16). Though *Henry et al.* [2017] reported a general preference for dawn flank formation of the KHI, we do not believe the MMS observations are in contradiction of the *Henry et al.* [2017] results. A conclusion about dusk flank preferential development would require normalization to observation time spent on each flank and detailed solar wind conditions, which is beyond the scope of this dissertation. Further, the change in MMS orbit from Phase 1 to Phase 2 occurred while MMS apogee precessed along the dayside dusk flank. As a result, MMS had one more dusk observation “season” than dawn “season” while its apogee was ideal for the observation of KH waves on the dayside flanks. This could account for the large discrepancy in dusk and dawn side observations of the KHI.

Observations of the KHI are evenly split on either side of the terminator: 22 events occurred on the dayside, and 23 events were observed along the tail. Events occurring farther downtail consistently have larger growth rates, unitless growth rates, and unstable solid angles than those occurring sunward of the terminator. This is expected as velocity shears between the magnetosheath and magnetosphere are smaller on the dayside where the solar wind is slowed immediately after the bow shock. Velocity shears increase as the magnetosheath plasma flows downtail and reaccelerates to match solar wind speeds. Large velocity shears are expected to increase growth rate

and decrease the stabilizing effects of the magnetic field, resulting in increased growth rates, unitless growth rates, and unstable solid angles.

- A cluster of KHI events were observed at high southern magnetic latitudes.

MMS observed a cluster of nine KH events at high southern magnetic latitudes (GSM  $Z \leq -4.5 R_E$ ). This is a new finding, as previous magnetospheric missions were constrained to more equatorial orbits. Prior to the launch of MMS, only two studies of high latitude KHI had been conducted using Cluster data [*Hwang et al.*, 2012; *Ma et al.*, 2016]. One of the high latitude events listed in this work has been the subject of case studies by *Nykyri et al.* [2021b] and *Michael et al.* [2021].

# Chapter 4

## Ion Scale Waves within the KHI

At the time of submission, the work presented in this Chapter is in preparation for submission to *Geophysical Research Letters*.

### 4.1 Expected Wave Modes

Plasmas are able to support a veritable “zoo” of wave modes, each with its own unique properties and generation mechanisms. At the ion scale, the wave modes we most expect to observe within the KHI are ion cyclotron waves, kinetic Alfvén waves, and kinetic magnetosonic waves. The generation mechanisms and characteristic behavior of each wave mode are described in the following sections and summarized in Table 4.1.

### 4.1.1 Ion Cyclotron Waves

In the plasma frame, ion cyclotron (IC) waves propagate up to, but not above, the ion cyclotron frequency: the frequency at which ions gyrate about the magnetic field. The electrostatic IC wave mode arises from the kinetic description of a cold, adiabatic plasma in which the magnetic field is constant and wave propagation is assumed to be parallel to the field [Nicholson, 1983]. However, the IC waves are not limited to parallel propagation and may, in fact, be as close as  $2^\circ$  from perpendicular to the background field [Nicholson, 1983].

It is also possible to derive an electromagnetic ion cyclotron (EMIC) wave mode if one does not assume a cold, adiabatic plasma [Peñano and Ganguli, 2002]. This EMIC wave is limited to parallel or quasi-parallel propagation. Both the electrostatic IC and EMIC wave modes are left-hand polarized with respect to the magnetic field. We may distinguish between the electrostatic and electromagnetic modes via comparison of the electric and magnetic wave fields. The ratio of the wave fields  $\delta E/\delta B$  is expected to at most on the order of the Alfvén velocity for electromagnetic waves, and larger for electrostatic waves [Peñano and Ganguli, 2002].

As the frequency of the IC wave mode approaches the ion cyclotron frequency of the plasma, ions can be energized via resonance. Left-handed EMIC waves are also capable of energizing electrons, despite the right-handed nature of the electron motion [Peñano and Ganguli, 2002].

Both the electrostatic IC and EMIC wave modes may be driven by ion beams, such as those produced at reconnection sites within KH vortices. Gradients in parallel velocity parallel (perpendicular) to the magnetic field can drive electrostatic (electromagnetic) IC waves [Nykyri et al., 2003b, 2006a; Peñano and Ganguli, 2002;

*Kim et al.*, 2004]. Due to the twisting of magnetic field lines in the KH vortex, we may expect both electrostatic and electromagnetic IC waves to develop, perhaps even in different regions of the same KH wave as the relative geometry of the velocity shear and magnetic field changes. EMIC waves may additionally be driven by the overlap of hot anisotropic plasma with another cold, dense plasma population [*Zhang et al.*, 2017]. Such overlaps would be expected around KH vortices where the hot magnetosheath plasma is mixed with the cold, dense magnetosphere.

#### 4.1.2 Kinetic Alfvén Waves

*In the literature, the Kinetic Alfvén wave is often abbreviated as “KAW.” For consistency with the other wave modes presented in this work, we will refer to the “KA wave.”*

The kinetic Alfvén (KA) wave mode bridges the gap between kinetic wave modes and other Alfvén waves described by MHD physics [*Nykyri et al.*, 2006b]. Though it is often described as a left-handed, parallel propagating wave [*Moore et al.*, 2016, 2017], the KA wave can propagate across a range of angles, and at high propagation angles and high values of  $\beta$ , the handedness of the KA wave changes from left to right [*Nykyri et al.*, 2006b; *Krauss-Varban et al.*, 1994]. The KA wave can develop in plasmas with  $m_e/m_i < \beta_e < 1$ , that is, plasma with electron beta less than one and greater than the electron to ion mass ratio ( $\approx 0.0005$  in space plasmas in which protons are the dominate ion species).

Within KH vortices, KA waves can be generated via mode conversion. At points of Alfvén resonance where the speed of the surface mode wave matches the local Alfvén speed, surface waves can be converted to KA waves [*Chaston et al.*, 2007;

*Johnson et al.*, 2001]. These Alfvén resonance points are more common within KHI due to the varying magnetic field strength caused by the rotating vortex twisting and compressing field lines.

KA waves are capable of driving ion energization into the magnetosphere [*Hasegawa*, 1976]. A component of the KA wave mode’s electric field is parallel to the background magnetic field, which leads to both effective ion acceleration and electron heating parallel to the field [*Hasegawa*, 1976; *Nykyri et al.*, 2021b]. Theoretical work has also shown KA waves driving perpendicular heating via turbulence [*Johnson and Cheng*, 2001].

### 4.1.3 Magnetosonic Waves

The fast magnetosonic (FM) wave mode is one of three wave modes which arise from the MHD description of plasma. FM mode waves are incredibly important because they can carry energy perpendicularly across magnetic field lines. Models have shown the FM wave mode can be triggered by a combination of fast magnetosheath flows and perturbations in total pressure, such as those seen near the center of KH vortices [*Mann et al.*, 1999]. The kinetic counterpart of the MHD FM wave is the kinetic magnetosonic (KM) wave mode. KM waves may be driven by ion shells, such as those generated by mid-latitude reconnection within the KHI [*Moore et al.*, 2016; *Nykyri et al.*, 2021c].

Unlike the IC and KA wave modes, the FM and KM waves may propagate both above and below the local ion cyclotron frequency. FM waves above the ion cyclotron frequency and below the lower hybrid frequency have been shown in models to effectively heat ions [*Lembege et al.*, 1983]. Similar heating has also been shown for



large amplitude KM waves propagating below the ion cyclotron frequency [*Terasawa and Nambu*, 1989]. More recent observational studies have confirmed that KM wave modes associated with the KHI do indeed contribute to ion heating in space plasmas [*Moore et al.*, 2016, 2017].

KM waves typically propagate perpendicularly or quasi-perpendicularly to the background field and are consistently right-handed with respect to the background magnetic field [*Krauss-Varban et al.*, 1994; *Moore et al.*, 2016].

By comparing the propagation angle, ellipticity, and electromagnetic or electrostatic nature of an observed wave interval, we may determine which wave mode it is most likely to be. The characteristic behavior of these parameters is summarized in Table 4.1 for the electrostatic IC, EMIC, KA, and KM wave modes considered in this work.

Table 4.1: Characteristic behavior of the electrostatic and electromagnetic ion cyclotron, kinetic Alfvén, and magnetosonic wave modes.

Wave Mode	Propagation Angle	Ellipticity	EM or ES
Ion Cyclotron	Parallel & Perpendicular (Quasi-)Parallel	Left	Electrostatic
		Left	Electromagnetic
Kinetic Alfvén	(Quasi-)Parallel	Left or Right	Electromagnetic
Kinetic Magnetosonic	(Quasi-)Perpendicular	Right	Electromagnetic

## 4.2 Example Interval

As previously described in Section 2.2.2, we use the minimum variance of the magnetic field (MVA-B) technique to identify intervals of well polarized wave activity. The wave vector direction,  $\hat{\mathbf{k}}$ , is calculated for each wave interval by applying a sliding window to the high pass filtered magnetic field. The high pass filtered field is obtained using

a cutoff frequency of 0.005 Hz to remove low frequency oscillations in the field caused by the KHI. The length of the MVA-B window is proportional to the maximum observed ion cyclotron frequency, such that the window length,  $t_{win} = 1/f_{IC\max}$ . The sliding window is shifted one-half the window length,  $t_{win}/2$ , to ensure some overlap in analysis. We are concerned only with well determined wave vectors during well polarized wave intervals. For the purpose of the current work, a well determined wave vector direction has an intermediate to minimum eigenvalue ratio  $\lambda_{int}/\lambda_{min} > 5$ . Well polarized intervals additionally have intermediate to maximum eigenvalue ratios such that  $\sqrt{\lambda_{int}/\lambda_{max}} > 0.5$ . One such well defined wave interval occurred during the example KHI event on 26 September 2017 from 16:43:03 to 16:43:06 UT.

From 16:43:03 to 16:43:06 UT, MMS was in the magnetosheath and observed a well polarized wave field. Figure 4.1 depicts the hodogram of the perpendicular wave components,  $B_\xi$  and  $B_Y$  (as described in Section 2.2.2) traced in time from the start (green circle) to the end (red square) of the interval. The perpendicular components rotate in a right-handed sense about the background magnetic field, which points into the page. The calculated ellipticity,  $\epsilon = 0.66$ , is in agreement with the hodogram. The wave vector during this interval propagates at about  $122^\circ$  from the background electric field. The right-handed polarization and quasi-perpendicular propagation of the wave field in this interval are consistent with a KM wave.

Additionally, we note the perpendicular wave field components complete nearly two full revolutions within the interval. As the interval is proportional to the ion cyclotron frequency, this indicates the wave frequency is greater than  $f_{IC}$ , which is further evidence that we are indeed observing a KM wave. The wave mode is also strongly electromagnetic, with a normalized electric to magnetic field ratio

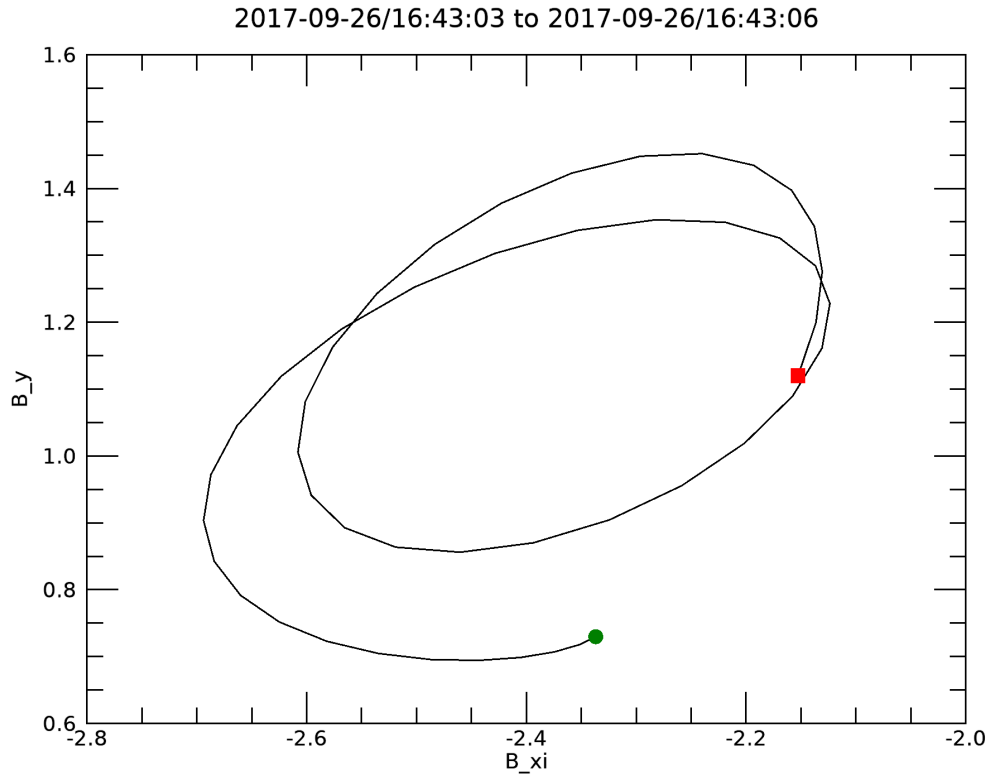


Figure 4.1: The trace of perpendicular components (see Section 2.2.2) of the wave field observed from 16:43:03 (green circle) to 16:43:06 (red square) on 26 September 2017. The wave field is right-handed polarized with respect to the background magnetic field (into the page) and propagates quasi-perpendicularly ( $\theta_{kB} = 122^\circ$ ) to the background field.

$(\delta E/\delta B)/v_A = 0.008$ , consistent with the KM mode.

We next attempt to determine the driving source of the observed wave. As described in Section 4.1.3, the FM wave may be driven by ion shells. The ion distribution function as observed by the FPI during the interval from 16:43:01 to 16:43:06 UT is shown in Figure 4.2. There is no clear evidence of ion shells in the distribution, which would appear in the distribution as a crescent of energetic particles shifted in single direction from the origin. Instead, the cold population (smaller velocities) is only slightly shifted in the negative parallel direction. The high energy population (larger velocities) is somewhat cigar shaped: the parallel velocity is larger than the perpendicular. However, the ion population as a whole is very nearly isotropic, with  $T_{\perp}/T_{\parallel} = 1.06$ .

We also consult the distribution of  $H^+$  ions observed by the HPCA instrument during the wave interval, shown in Figure 4.3. The ions observed by HPCA are cooler than those observed by FPI (the maximum velocity observed by HPCA is  $\approx 200$  km/s compared to  $\approx 1000$  km/s observed by FPI), so we are able to see more detail in the distribution of the cold ions. As can be seen in Figure 4.3, there is some evidence of ion shells in both the upper and left quadrants of the distribution. These shells may be the source of the KM wave observed in the interval from 16:43:03 to 16:43:06 UT.

The KM wave observed from 16:43:03 to 16:43:06 on 26 September 2017 can be an important contributor to ion heating within the KHI. We suspect this wave is driven by shell distributions of the cold ions. Efforts to confirm this suspicion using the Waves in Homogenous Anisotropic Magnetized Plasma (WHAMP) dispersion solver are ongoing [Rönmark, 1982]. We also cannot, at this time, discount the potential for a remote generation mechanism, such that the wave is convected to the observation

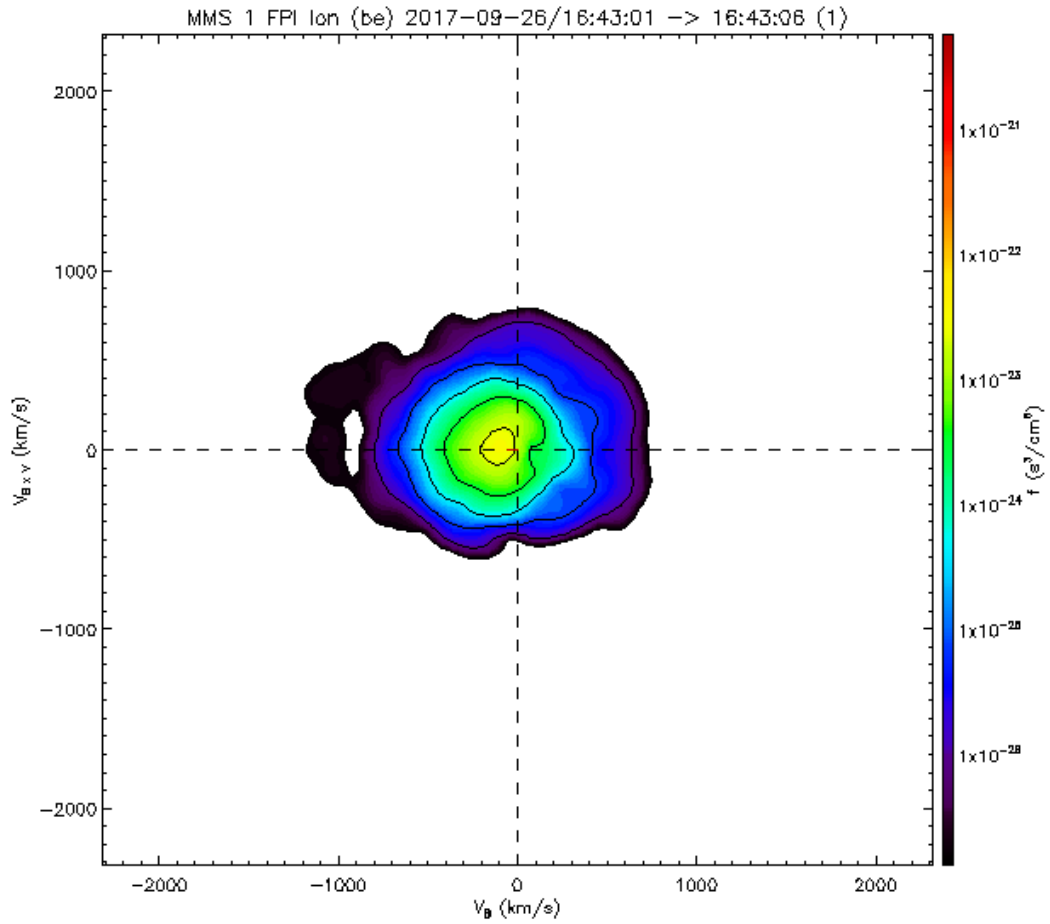


Figure 4.2: The ion distribution function from the FPI instrument aboard MMS1 during the example wave interval is very slightly anisotropic ( $T_{\perp}/T_{\parallel} = 1.06$ ). The cold ions are shifted slightly in the negative  $B_{\parallel}$  direction while the hotter ions are more cigar shaped.

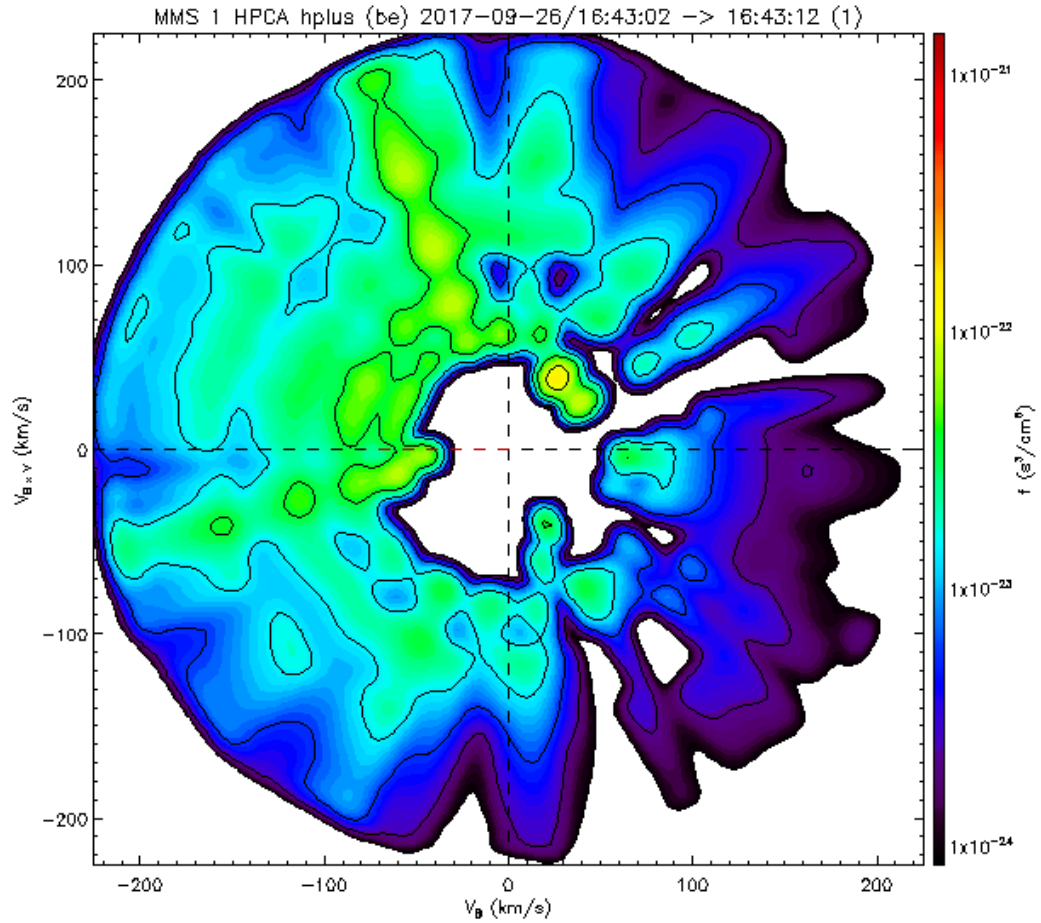


Figure 4.3: The  $H^+$  ion distribution function from the HPCA instrument aboard MMS1 during the example wave interval shows some evidence of shells in the cold ions which could drive a KM wave.

point and the driving ion shells are not observed.

While the exact driving mechanism of the example wave interval is not yet determined, we may still contextualize the small scale waves observed during the KHI via comparison with similar observations when the KHI is not active.

### 4.3 Comparison of KHI and non-KH Observations

In order to determine the contribution of the KHI to heating, it is necessary to compare KHI observations to those made when the KHI is not active. As described in Chapter 2 for the KHI events, non-KHI events were also identified by searching the MMS event database, SITL notes, and Quicklook plots to find MMS crossings of the magnetopause during which the signatures of the KHI are not present. One such “quiet” crossing is shown in Figure 4.4. MMS crossed the dayside dusk flank from the magnetosheath to the magnetosphere in the two hours between 16:00 and 18:00 UT on 01 November 2018. There is a single, smooth transition from magnetospheric energy, density and temperature to magnetosheath values shortly after 16:50 UT rather than the many quasi-periodic fluctuations associated with the KHI. A single, large velocity shear is observed at the same time, as is expected during a quiet magnetopause boundary crossing. Magnetic field and total pressure signatures are also not indicative of the KHI.

It is important to note that while the quiet crossings do not show signatures of active KHI, there is no way to ensure that the KHI was not previously operational. A prior KHI at the location may have affected the characteristics (e.g. thickness, density) of the boundary region. However, because we are concerned only with the ion

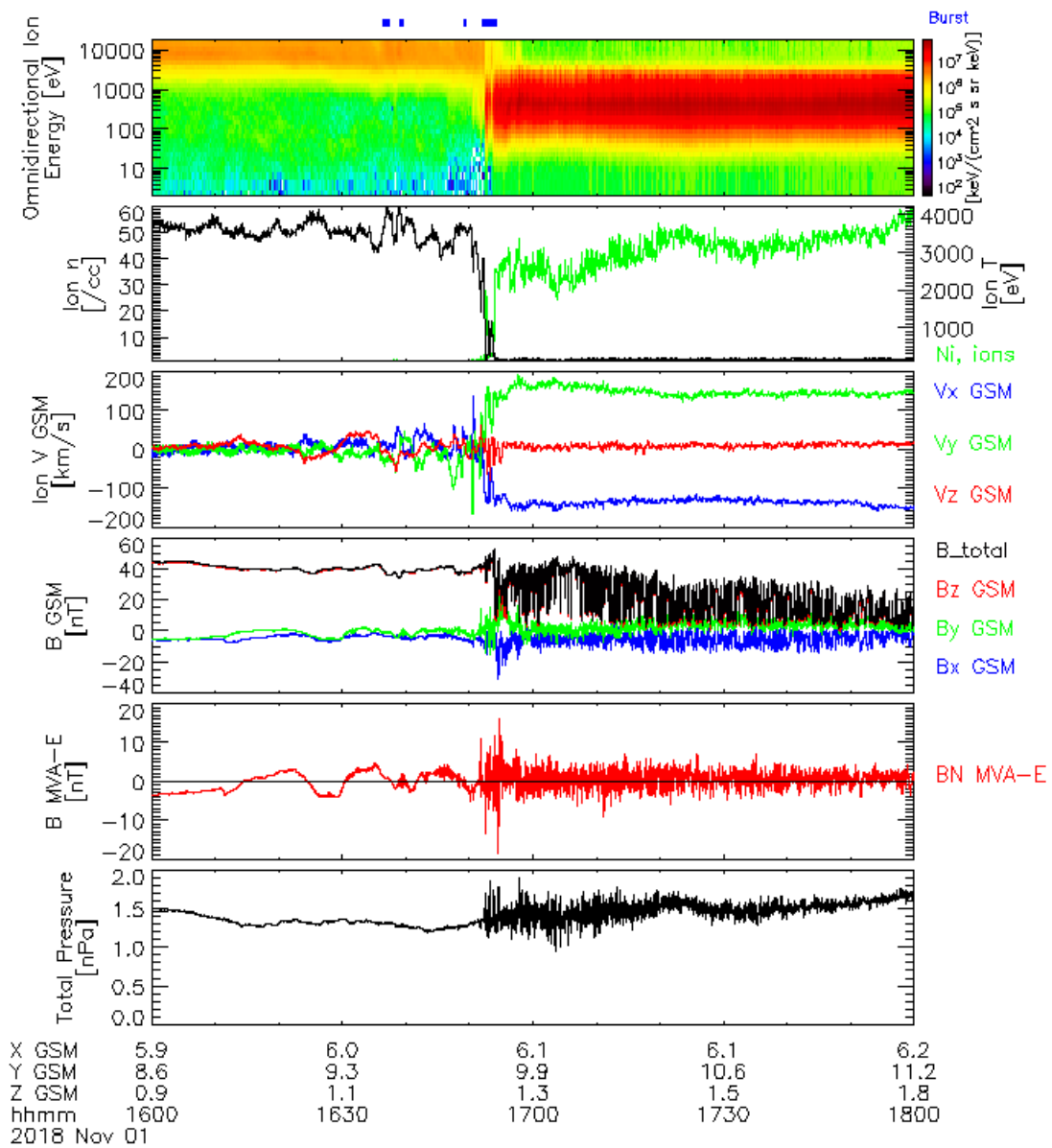


Figure 4.4: MMS observations of a quiet magnetopause crossing from 16:00 to 18:00 UT on 01 November 2018 in which no signatures of the KHI were observed.



scale waves generated by the active KHI, the potential effects of previously operational KHI are ignored.

The 45 KH events presented in Chapters 2 and 3 total 66 hours and 52 minutes of MMS observations. 47 hours and 33 minutes of observation are on the dusk flank, while 19 hours and 19 minutes are on the dawn flank. A total of 33 non-KH crossings were collected for comparison, comprising 66 hours and 20 minutes of MMS observations. 47 hours and 20 minutes of the non-KHI observations are on the dusk flank and 19 hours are on the dawn flank. We account for the slight inequality in KHI and non-KH observations by normalizing results for both observation types. More details about the non-KH observations may be found in Appendix B.

The automated region sorting method described in Section 2.2.1 is applied to the non-KH events as well. The region sorting results for the example KHI and non-KH events are shown in Figure 4.5. As expected, the mixed region is much more prominent during the KHI. Because MMS does not observe each region equally for both KHI and non-KH events, results presented in the statistical study (Section 4.4) are normalized to the number of well polarized wave intervals in each region for direct comparison.

## 4.4 Statistical Results

Within all well polarized intervals, for both KHI and non-KH observations, the mean total power, the normalized ratio of the electric and magnetic wave fields, and total integrated Poynting flux are calculated. The angle between  $\hat{\mathbf{k}}$  and the background magnetic field and the ellipticity as described in Section 2.2.2 are also determined.

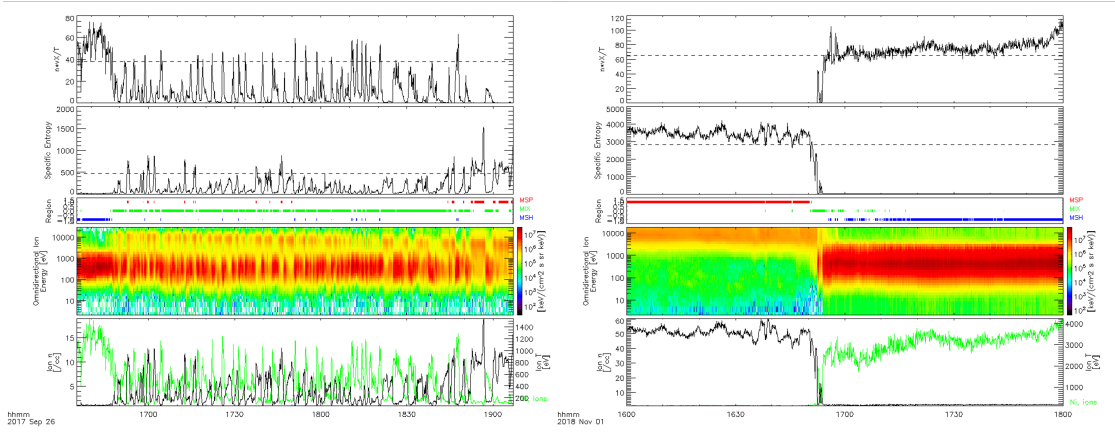


Figure 4.5: The region sorting parameters,  $S$  and  $nv_{tail}/T$ , automatically sorted regions, omnidirectional ion energy, and ion density and temperature for the example KHI event on 26 September 2017 (left) and the example quiet crossing on 01 November 2018 (right). As expected, the quiet crossing contains much less mixed plasma than the KH event.

In order to discern potential driving mechanisms, we also examine the mean ion temperature anisotropy, mean electron beta, and maximum parallel velocity shear in each wave interval. We attempt to quantify the contribution to heating made by ion scale waves in the KHI using the characteristic heating frequency and the change in energy across well polarized wave intervals.

#### 4.4.1 Wave Angle and Ellipticity

Results of the wave angle and ellipticity in each of the well polarized wave intervals are shown as 2D histograms in Figure 4.6. All wave intervals are sorted into bins according to their propagation angle and mean ellipticity, and all bins are normalized for ease of comparison. Observations from the magnetosphere, mixed, and magnetosheath regions for the KHI events are shown from left to right along the top of Figure 4.6. Observations from the non-KH events are order in the same format across the bottom

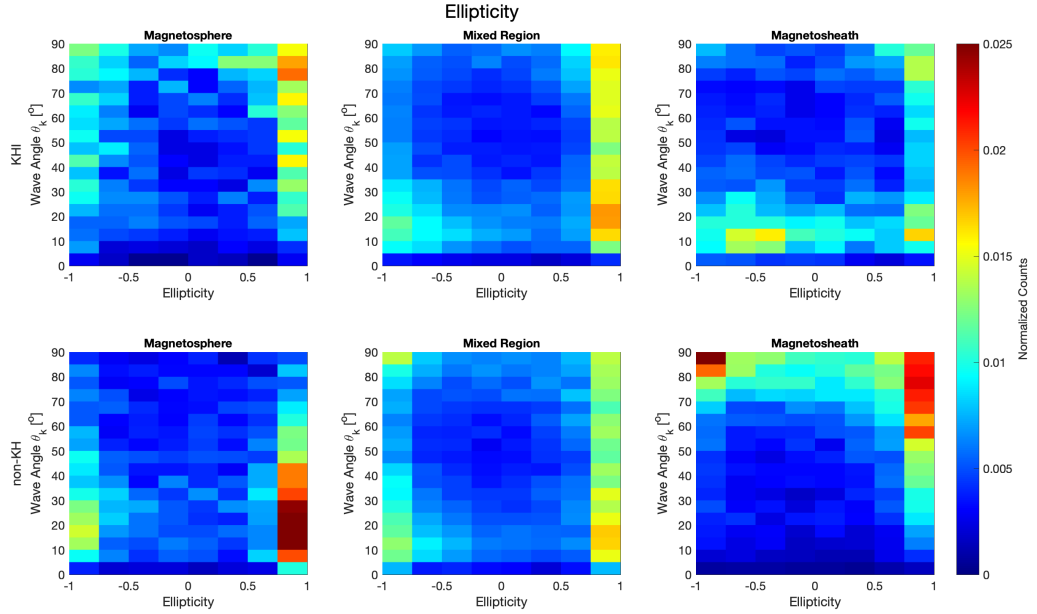


Figure 4.6: Normalized histograms of wave angle and ellipticity in the magnetosphere (left), mixed region (center), and magnetosheath (right) for KHI (top) and non-KH (bottom) observations.

of Figure 4.6.

For KHI observations in the magnetosphere (top left), most wave intervals are quasi-perpendicular to the field. Of those quasi-perpendicular intervals, most have right-handed polarization, but some are left-handed. The perpendicular right- and left-handed wave intervals are consistent with the KM and electrostatic IC wave modes, respectively. In contrast, wave intervals in the magnetosphere during non-KH observations (bottom left) are primarily quasi-parallel propagating. The parallel intervals are more often right-handed polarized, which is not consistent with any of the 3 expected wave modes. This may be due to Doppler shift effects as we observe these waves in the spacecraft frame moving through the plasma.

In the magnetosheath during KHI observations (top right), most wave intervals are

parallel propagating and left-handed polarized, consistent with the KA or EMIC wave mode. A smaller fraction of wave intervals are right-handed polarized, propagating both parallel and perpendicular to the background field, consistent with either KM or electrostatic IC waves. For the non-KH observations in the sheath (bottom right), wave intervals are mostly quasi-perpendicular. These perpendicular wave intervals are both right- and left-handed polarized, consistent with the KM and electrostatic IC wave modes, respectively.

In the mixed region, wave intervals for both KHI and non-KH (top and bottom center, respectively) observations are primarily right-handed polarized. The right-handed wave intervals span the range of propagation angles, though are slightly more common for parallel propagation. A smaller fraction of wave intervals are left-handed polarized at parallel propagation angles for both KHI and non-KH observations, indicative of KA or EMIC waves. The non-KH observations show an additional grouping of left-handed perpendicular wave intervals consistent with electrostatic IC waves.

We note some of the observed wave angle and ellipticity observations are not consistent with any of the electrostatic or electromagnetic IC, KA, or KM wave modes, namely the right-handed quasi-parallel waves seen in the magnetosphere (magnetosheath) during non-KH (KHI) observations and in the mixed region for both observation types. This may be due to the  $180^\circ$  ambiguity in the wave propagation direction (see section 2.2.2). Unfortunately, this ambiguity cannot be resolved via single spacecraft methods. Observations of the wave packet by multiple spacecraft at different times can be used to unambiguously identify  $\hat{\mathbf{k}}$ , but such analysis for the hundreds of thousands of wave intervals considered here is beyond the scope of this work.

Additionally, the ongoing detailed analysis of Doppler shift effects should be illu-

minating for these right-handed quasi-parallel wave intervals. Extreme Doppler shift effects may change the sign of ellipticity, which would make such observations consistent with the left-handed quasi parallel EMIC and KA wave modes. If Doppler shifts are not sufficient to change the sign of ellipticity, then these waves may in fact be low frequency Whistler waves.

#### 4.4.2 Mean $\delta E/\delta B$ Ratio

Difference histograms, like those shown in Figure 4.7, directly compare wave intervals during KHI and non-KH observations. All difference histograms in this chapter depict KHI dominated wave activity in red and non-KH dominated activity in blue. Green regions indicate there is no significant difference between KHI and non-KH observations.

Figure 4.7 depicts the normalized electric to magnetic wave field ratios, which are well below 1 for all angles, regions, and observation types. This suggests all the observed wave intervals are strongly electromagnetic, consistent with the EMIC, KA, and KM wave modes. In the magnetosphere (top), quasi-perpendicular KM waves dominate during KHI activity while parallel EMIC or KA waves dominate when the KHI is not active. This activity is reversed in the magnetosheath (bottom), where parallel EMIC or KA waves are more common when KHI is active and perpendicular KM waves are more common when no KHI is present. In the mixed region (middle) a small preference for parallel waves during the KHI can be seen, though the distinction between KHI and non-KH observations is much less clear, suggesting wave modes in the mixed region are not as strongly effected by the presence of KHI as those in either the magnetosphere or magnetosheath.

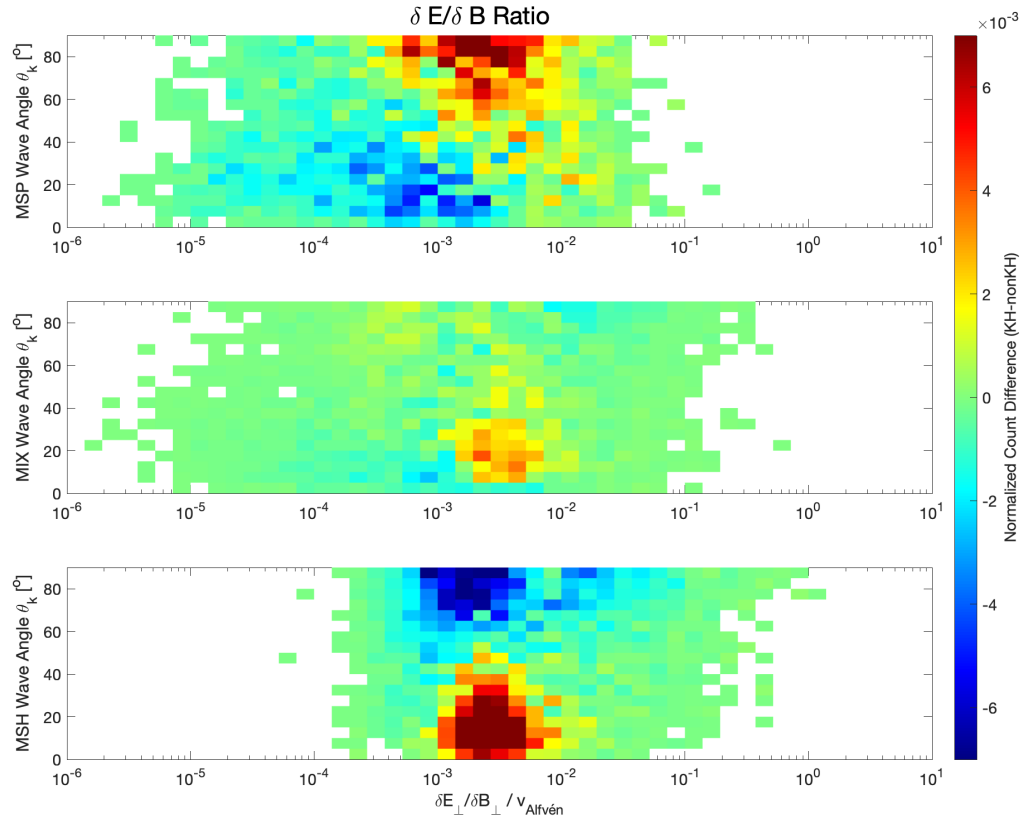


Figure 4.7: Normalized difference histograms comparing mean electric to magnetic wave field ratio and wave angle for the KHI and non-KHI observations in the magnetosphere (top), mixed region (middle), and magnetosheath (bottom).

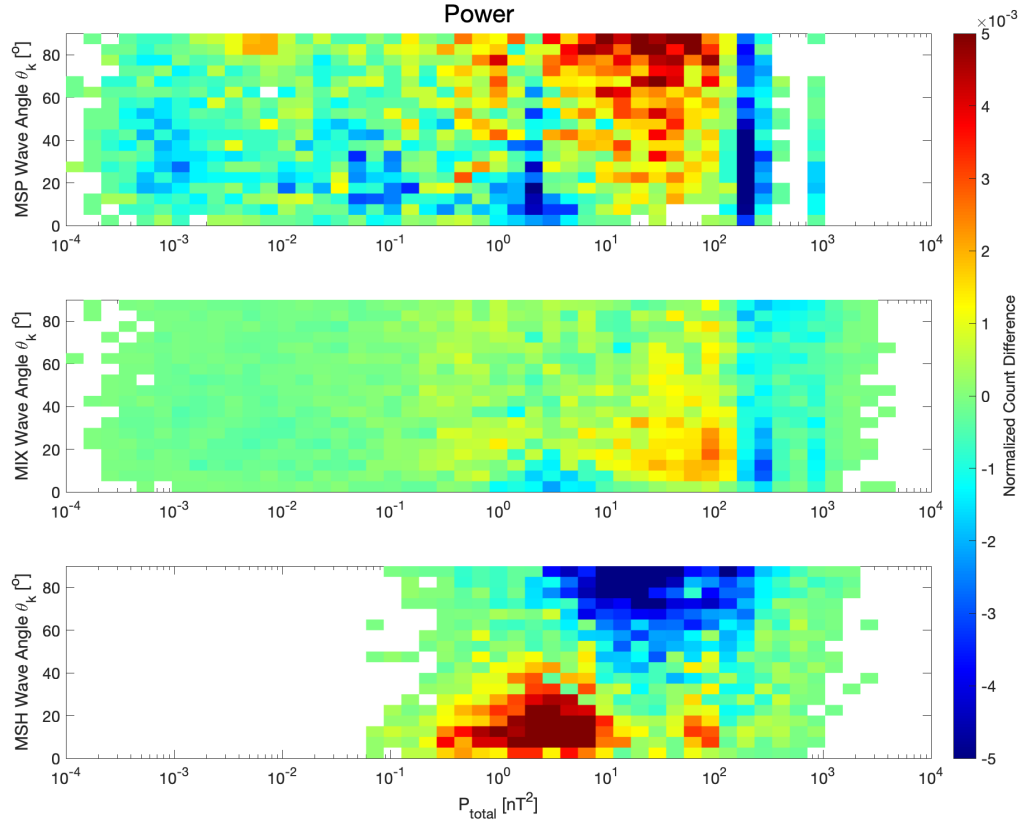


Figure 4.8: Normalized difference histograms comparing mean total wave power and wave angle for the KHI and non-KHI observations in the magnetosphere (top), mixed region (middle), and magnetosheath (bottom).

#### 4.4.3 Mean Total Power

Figure 4.8 depicts the propagation angle and mean total power in each wave interval. In the magnetosphere (top), quasi-perpendicular waves are more common when the KHI is present and have total power between  $0.1 \text{ nT}^2$  and  $100 \text{ nT}^2$ . Parallel waves are more common during non-KH observations, though with consistently lower power, typically less than  $10 \text{ nT}^2$ . There is, however, a band of very high power waves, greater  $100 \text{ nT}^2$  for all propagation angles during the non-KH observation.

In the magnetosheath (bottom), KHI associated wave activity has power between  $0.1 \text{ nT}^2$  and  $10 \text{ nT}^2$  with quasi-parallel propagation. Another smaller region of KHI dominance is observed for parallel waves with power around  $100 \text{ nT}^2$ . Non-KH wave activity is generally perpendicular with power between 1 and  $100 \text{ nT}^2$ .

In the mixed region (middle), parallel wave intervals with power between  $1 \text{ nT}^2$  and  $10 \text{ nT}^2$  are more common during non-KH observations. Waves with power between  $10 \text{ nT}^2$  and  $100 \text{ nT}^2$  are more commonly associated with the KHI for all propagation angles. Wave intervals with power above  $100 \text{ nT}^2$  at any angle are more commonly observed during non-KH observations. The differences between KHI and non-KH observations are much less pronounced in the mixed region than in either the magnetosphere or magnetosheath.

#### 4.4.4 Integrated Poynting Flux

Integrated over time, the Poynting flux describes the total energy in an electromagnetic wave which is available to do work, such as heat the plasma, during the interval in which the wave is observed. As shown in Figure 4.9, the total Poynting flux integrated over time in well polarized wave intervals is larger for KHI observations than for non-KHI observations in all regions. In the magnetosphere (top), quasi-perpendicular wave activity associated with the KHI commonly has higher integrated flux than the quasi-parallel activity associated with non-KH observations. In the magnetosheath (bottom), the main groupings of wave intervals associated with KHI and non-KH observations have similar total integrated fluxes, but a band of higher flux waves is observed at all propagation angles when the KHI is active. At all propagation angles in the mixed region (middle), flux is larger during the KHI, though this is less



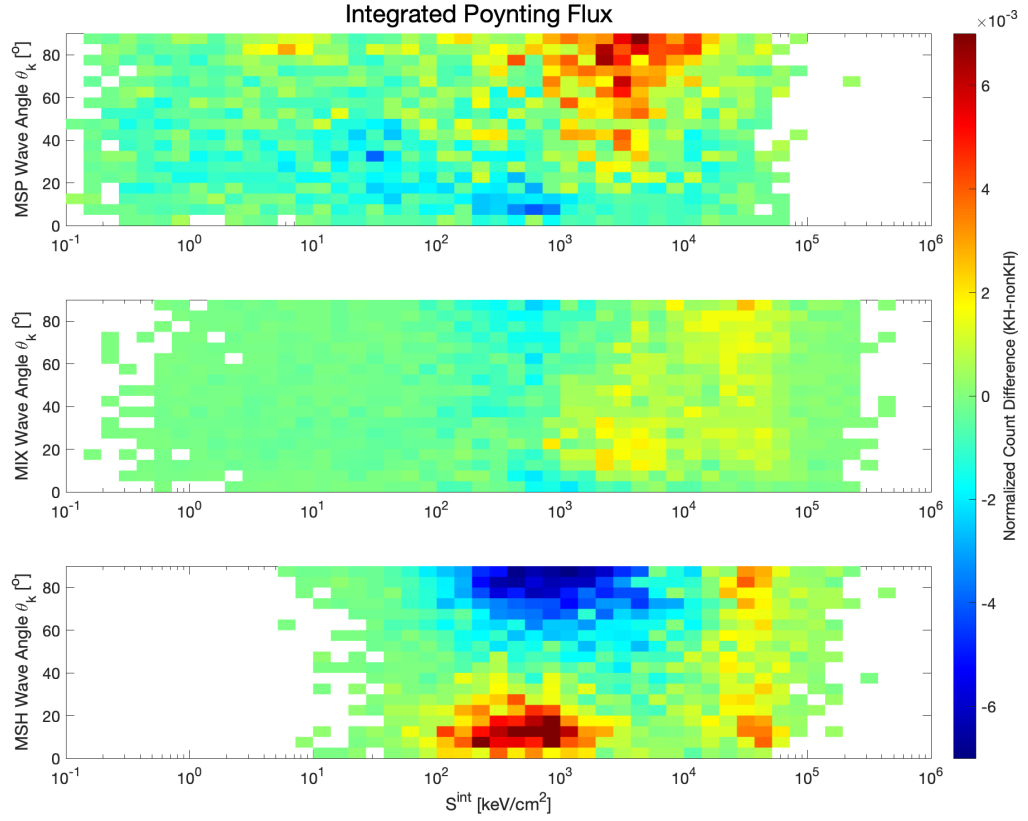


Figure 4.9: Normalized difference histograms comparing integrated total Poynting flux and wave angle for the KHI and non-KHI observations in the magnetosphere (top), mixed region (middle), and magnetosheath (bottom).

pronounced than in either the magnetosphere or magnetosheath.

The observed increase in integrated total Poynting flux during wave intervals associated with the KHI suggests more energy is available during KH activity to heat the plasma. We attempt to describe and quantify this potential heating in the following two sections.

#### 4.4.5 Characteristic Heating Frequency

We may characterize the rate of heating within well polarized wave intervals using recent work from *Nykyri et al.* [2021b] which derived the characteristic heating frequency (CHF) to describe the time-scale of non-adiabatic heating within the KHI,

$$f_{heat} = \frac{1}{S} \frac{dS}{dt} = \frac{\eta J^2}{P/(\gamma - 1)}. \quad (4.1)$$

That is, the frequency at which heating occurs is the ratio of the anomalous Ohmic heating and the plasma thermal energy density, with results in units inverse time,  $t^{-1}$ . For mono-atomic plasma the ratio of specific heats,  $\gamma$ , is 5/3.

Using the generalized Ohm's Law from Hall-MHD (see section 2.3), we can compute the anomalous Ohmic heating,  $\eta J^2$ , directly from spacecraft measurements, such that

$$\eta J^2 = (\mathbf{E} + \mathbf{v}_e \times \mathbf{B}) \cdot \mathbf{J} \quad (4.2)$$

where  $\mathbf{J}$  is the current density computed using the curlometer technique, and all other quantities are measured at each of the four MMS spacecraft and interpolated to the center of the spacecraft tetrahedron. The electron velocity and magnetic field measurements are interpolated to match the cadence of the survey mode EDP electric field measurements. It is important to note, the heating frequency can be either positive or negative, indicative of heating or cooling, due to off-diagonal components of the electron pressure tensor and electron inertial terms contained within the generalized Ohm's Law which are capable of breaking the frozen in condition. We consider only the absolute value of the heating frequency when characterizing the heating within a

well polarized wave interval.

The median CHF within each wave interval is shown in Figure 4.10. The calculation of the CHF requires both ion and electron data from all four MMS spacecraft, however, the MMS mission suffered a brief outage in ion measurements from MMS3 in 2017 and a loss of electron measurements from MMS4 for all events after July 2018. Therefore, we are able to calculate the CHF for only 28 of the 45 KHI and 22 of the 33 non-KH observations. The results shown in Figure 4.10 are for only those events with ion and electron data available from all four spacecraft.

In the magnetosphere (top) quasi-perpendicular waves associated with the KHI and quasi-parallel waves associated with non-KH observations have similar median CHF values. There is, however, a prominent band of KHI associated wave intervals across all propagation angles in which the median CHF is increased. Within the magnetosheath (bottom), the quasi-parallel waves associated with the KHI tend to have slightly higher median CHF values than the non-KH quasi-perpendicular wave intervals. We also see a band of KHI associated wave intervals covering the full range of propagation angles in which the median CHF is increased. This increase in CHF during KHI associated wave intervals is also observed in the mixed region (middle), though it is not as pronounced as either the magnetosphere or magnetosheath. The increased CHF within KHI wave intervals indicates that the waves associated with KHI are able to heat plasma more efficiently than the waves observed when there is no KHI activity.

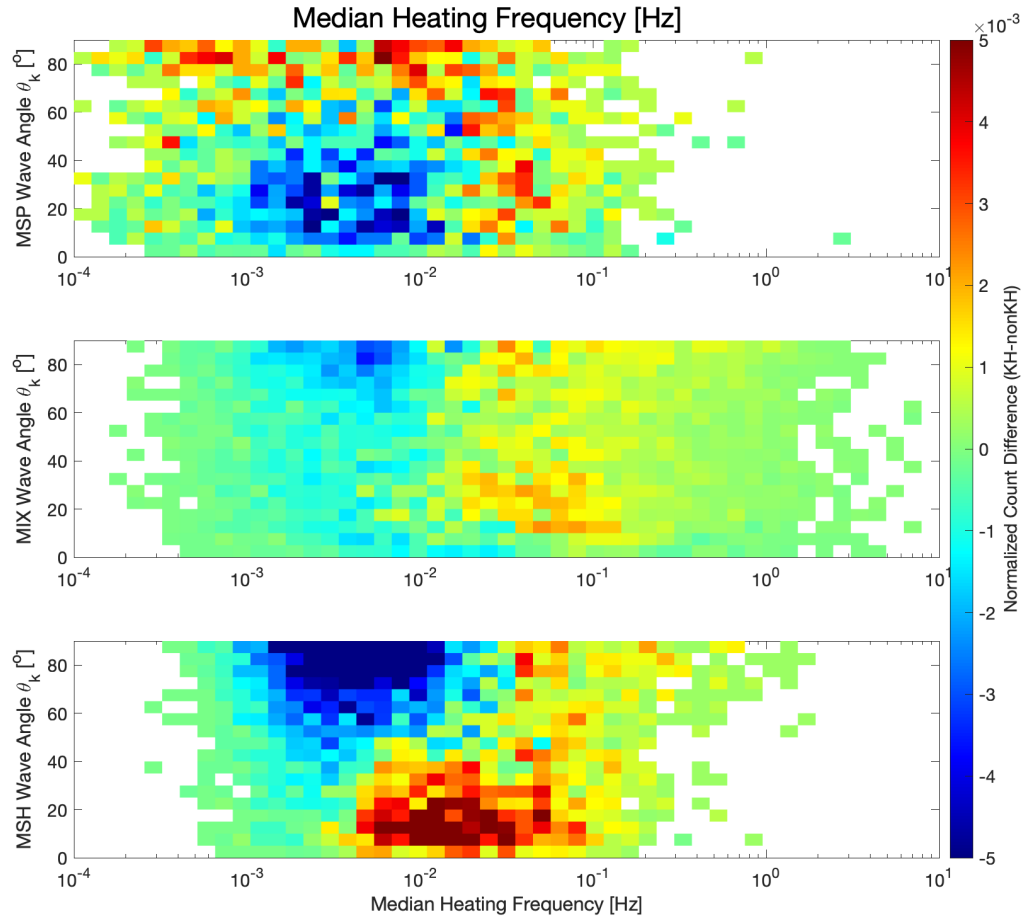


Figure 4.10: Normalized difference histograms comparing the median characteristic heating frequency and wave angle for the KHI and non-KHI observations in the magnetosphere (top), mixed region (middle), and magnetosheath (bottom). Due to data outages on MMS3 and MMS4, the heating frequency is only available for 28 of the 45 KHI observations and 22 of the 33 non-KH observations.

#### 4.4.6 Energy Analysis

We also consider the observed change in energy across well polarized wave intervals. The absolute change in average energy is shown in Figure 4.11. Within the magnetosphere (top), wave intervals associated with the KHI at all propagation angles show greater changes in energy than the quasi-parallel wave intervals associated with the non-KH observations. Similarly, the KHI associated wave intervals at all propagation angles in the magnetosheath (bottom) have greater energy changes than the quasi-perpendicular wave intervals observed when the KHI is not active. This trend is also observed in the mixed region, though the difference is not quite so pronounced as it is the magnetosphere or magnetosheath.

It is also worthwhile to test our assumption that increased Poynting flux will lead to greater heating within wave intervals. Figure 4.12 depicts 2D histograms comparing the change in average energy with total integrated Poynting flux in the well polarized wave intervals. In the magnetosphere (top) and magnetosheath (bottom), Poynting flux and energy changes are positively correlated. The KHI associated waves dominate the upper right quadrant, where both integrated flux and change in energy are high. The wave intervals associated with non-KH observations sit lower and to the left, indicating both lower integrated flux and energy changes. In the mixed region integrated flux is not as well separated for the KHI and non-KH observations, though the change in energy is much larger for KH associated wave intervals.

The larger changes in energy combined with the observed increases in Poynting flux associated with the KHI supports our conclusion that ion scale waves driven by the KHI are better able to heat the plasma than similar waves which develop when the KHI is not active. We note that some change in energy is expected across any

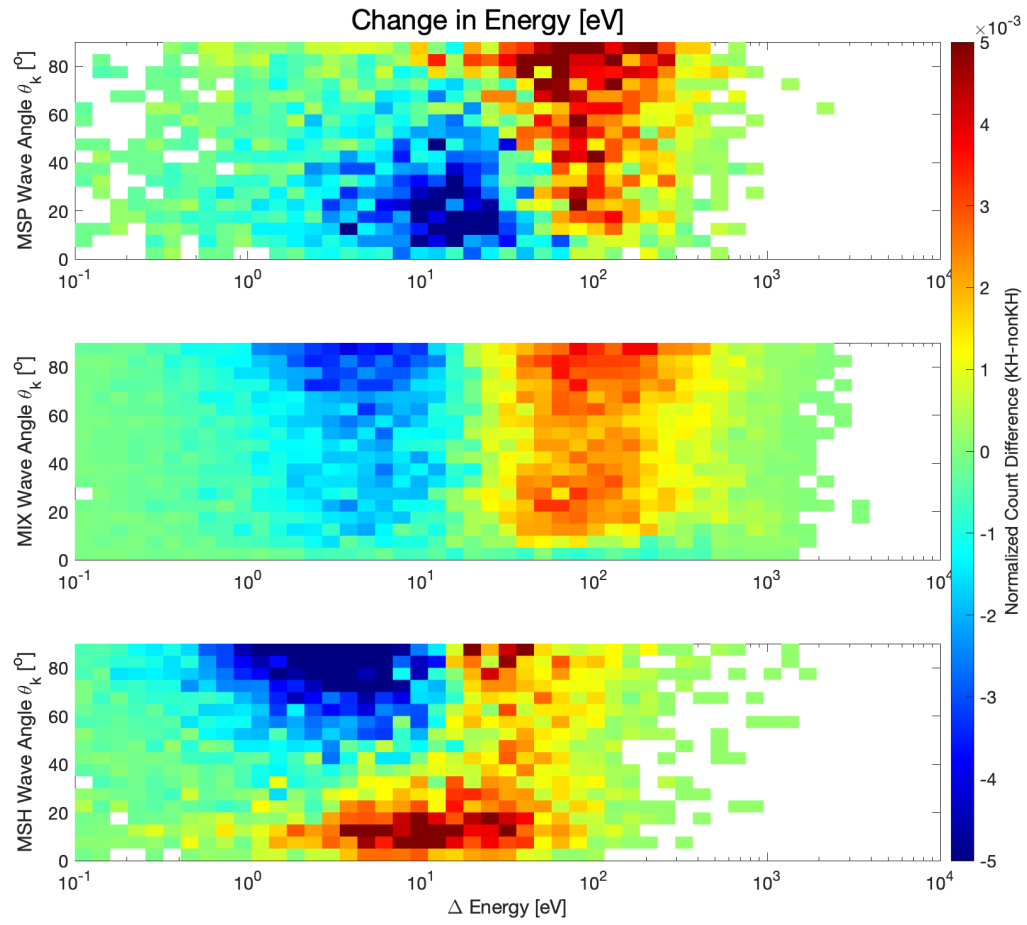


Figure 4.11: Normalized difference histograms comparing the change in average energy across wave intervals and the wave angle for the KHI and non-KHI observations in the magnetosphere (top), mixed region (middle), and magnetosheath (bottom).

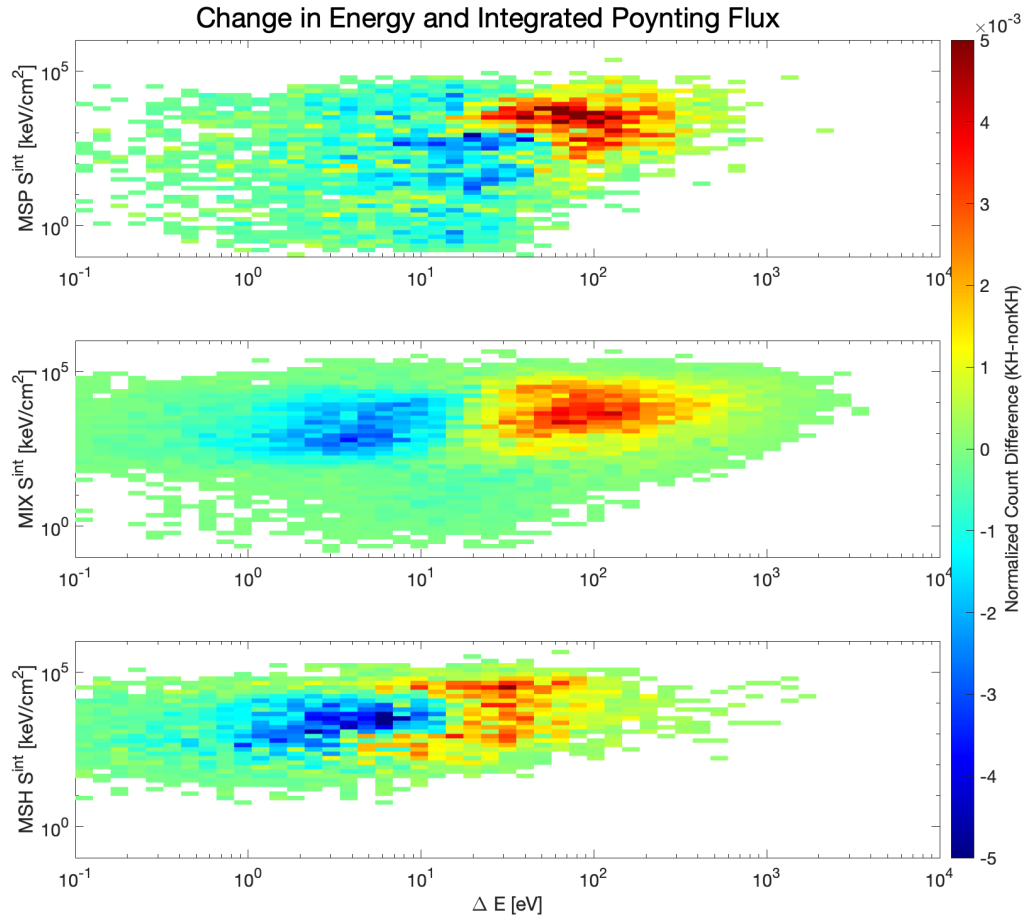


Figure 4.12: Normalized difference histograms comparing the change in average energy across wave intervals and the total integrated Poynting flux for the KHI and non-KHI observations in the magnetosphere (top), mixed region (middle), and magnetosheath (bottom).

ion scale interval, regardless of the presence of well polarized waves. Ongoing work attempts to quantify the expected energy change across intervals without ion scale wave activity which will be used to normalize the energy changes in well polarized wave intervals.

We next consider generation mechanisms which may explain the observed ion scale wave behavior.

#### 4.4.7 Mean Temperature Anisotropy

Ion temperature anisotropies, that is increases in the perpendicular component of ion temperature relative to the parallel component, are known drivers of EMIC waves. Ion temperatures are mostly isotropic during KHI observations in all regions, as can be seen in Figure 4.13, with  $T_{\perp}/T_{\parallel}$  between 0.7 and 1.5 in almost all wave intervals. There is, however, a significant number of wave intervals in the magnetosheath (bottom) in which the perpendicular ion temperature is 2 to 2.5 times hotter than the parallel ion temperature. These anisotropic ions may be the source of the increased parallel and quasi-parallel EMIC wave activity in the magnetosheath during KHI observations.

During non-KH observations, the perpendicular ions are consistently warmer than the parallel ions in all regions: anisotropy is between 1 and 1.5 in all regions for non-KH wave intervals.

#### 4.4.8 Mean Electron Beta

The propagation of KA waves requires electron beta between the electron to ion mass ratio and one, that is  $m_e/m_e < \beta_e < 1$ . Observations of mean electron beta during well polarized wave intervals is depicted in Figure 4.14. Magnetosheath electron beta



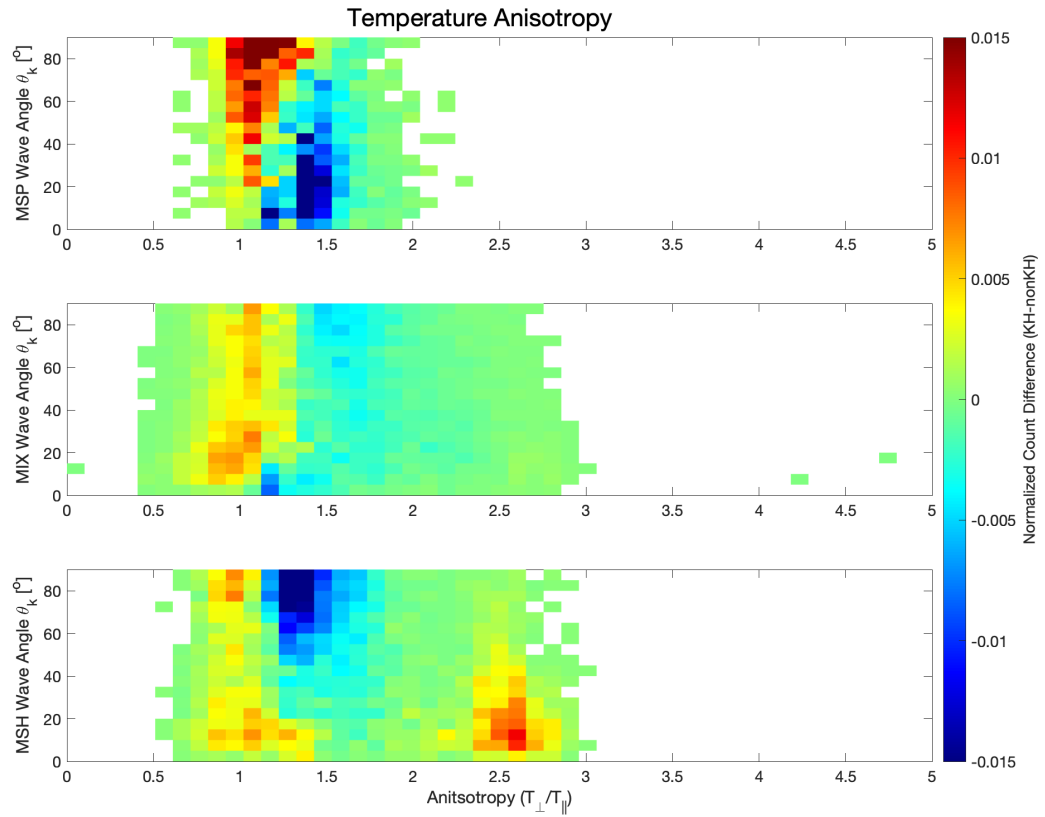


Figure 4.13: Normalized difference histograms comparing mean temperature anisotropy,  $T_{\perp}/T_{\parallel}$ , and wave angle for the KHI and non-KHI observations in the magnetosphere (top), mixed region (middle), and magnetosheath (bottom).

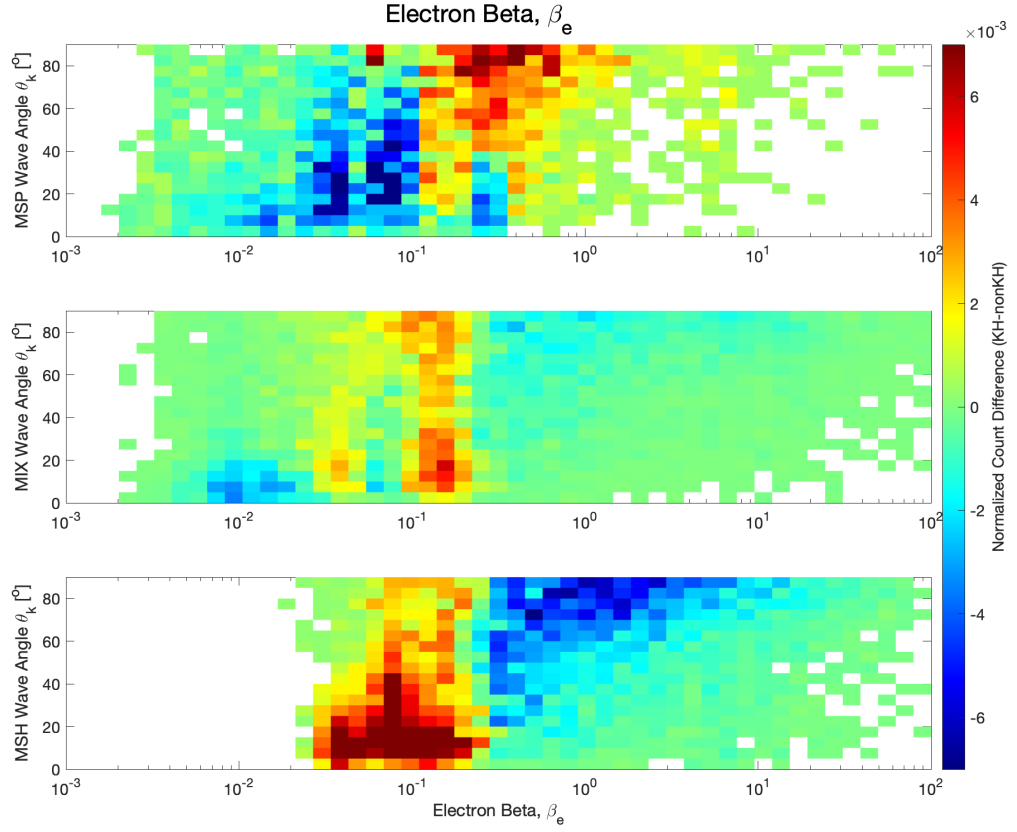


Figure 4.14: Normalized difference histograms comparing mean electron beta,  $\beta_e$ , and wave angle for the KHI and non-KHI observations in the magnetosphere (top), mixed region (middle), and magnetosheath (bottom).

(bottom) is lower when the KHI is active relative to the non-KH observations. Thus, parallel propagating KA waves are supported in the sheath during active KHI whereas they would not necessarily be supported when there is no KH activity.

Magnetosphere electron beta (top) is typically below 1 for both KHI and non-KH observations, thus KA waves would be supported in either case. During the KHI, wave intervals in the mixed region (middle) typically have  $\beta_e \approx 0.1$  and propagate at all angles relative to the background field. When the KHI is not active, there

are two subsets of wave activity in the mixed region: one with low beta ( $\beta_e \approx 0.01$ ) propagating parallel to the field, and another with higher beta ( $\beta_e$  between 0.1 and 1) propagating perpendicular to the field.

#### 4.4.9 Maximum Parallel Velocity Shear

Gradients in the component of velocity parallel to the background magnetic field are capable of driving electrostatic IC and EMIC waves. The change in parallel velocity between MMS1 and each of the other MMS spacecraft was calculated during well polarized wave intervals as observed by MMS1. Figure 4.15 compares the parallel shear between MMS1 and MMS2 (left), MMS1 and MMS3 (center), and MMS1 and MMS4 (left) with wave propagation angle. As previously mentioned, ion velocity data is not available from MMS3 during three (one) KHI (non-KH) events, so the velocity shear results for the MMS1-MMS3 pair include only the 42 (32) KHI (non-KH) observations for which data is available.

In all regions the parallel velocity shear is consistently higher during KHI activity. Shear in the magnetosheath (bottom) is typically an order of magnitude larger for KHI observations than the non-KH observations. A similar, though less stark, contrast is also observed in the mixed region (middle). Within the magnetosphere (top), velocity shears during KHI and non-KH observations are closer, but the KHI observations are still dominate for shears around and above 10 km/s. The increased shear during KHI may be the source of both the perpendicular and parallel wave activity observed in the magnetosphere and magnetosheath, respectively, during the KHI.

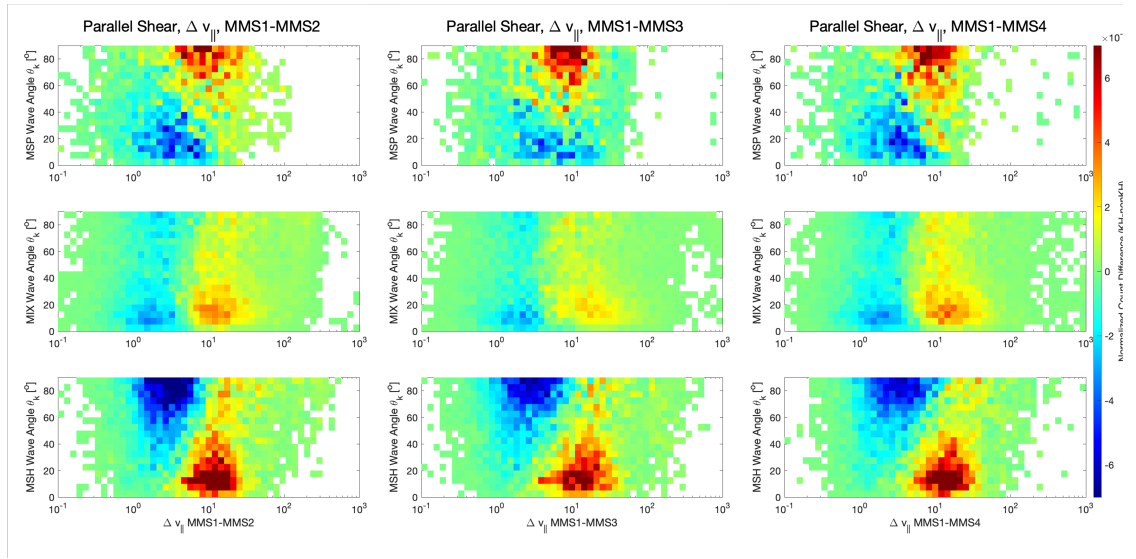


Figure 4.15: Normalized difference histograms comparing the difference in parallel velocity from MMS1 to MMS2 (left), MMS3 (center), and MMS4 (right) and wave angle for the KHI and non-KH observations in the magnetosphere (top), mixed region (middle), and magnetosheath (bottom). Ion velocity data is not available from MMS3 for 3 (1) KHI (non-KH) events. The MMS1-MMS3 results shown include only the 42 (32) events for which data is available.

## 4.5 Conclusions

Well polarized wave intervals during observations of the KHI are identified using MVA-B analysis as described in Section 2.2.2. We present analysis of a single wave interval from 16:43:03 to 16:43:06 UT during the KHI event on 26 September 2017. A hodogram of the perpendicular field components showed a right-handed wave propagating quasi-perpendicularly to the background magnetic field in the magnetosheath. The trace of the perpendicular components completes nearly two full revolutions within a single ion gyroperiod, suggesting the observed wave is a kinetic magnetosonic wave propagating with a frequency greater than the local ion cyclotron frequency. The wave field is also electromagnetic ( $(\delta E/\delta B)/v_A = 0.008$ ), consistent with the KM wave mode.

The source of the particular wave observed from 16:43:03 to 16:43:06 UT has not been positively determined, but the  $H^+$  ion distribution observed by the HPCA instrument shows some evidence of shells, which may be the source of the observed KM wave activity. Ongoing analysis of the distributions from both HPCA and FPI using the WHAMP distribution solver could confirm if they are indeed the source of the observed KM wave.

Well polarized wave intervals within KHI observations are also compared with wave intervals observed when the KHI is not active. Within each wave interval we calculate propagation angle, ellipticity, the normalized wave field ratio ( $\delta E/\delta B$ ), the mean total power, and integrated Poynting flux. We attempt to describe the heating within well polarized wave intervals using the characteristic heating frequency and change in average energy. We also make an effort to determine the generation mechanism of the observed waves. In order to do so, we calculate the ion temperature

anisotropy, electron beta, and parallel velocity shear in each wave interval.

Observations of the well polarized wave intervals are consistent with electromagnetic ion cyclotron (EMIC), kinetic Alfvén (KA), and kinetic magnetosonic (KM) waves during KHI and non-KH boundary crossings. A few of the wave intervals have combined ellipticity and propagation angles inconsistent with any of the expected wave modes, though this may be due to the  $180^\circ$  ambiguity in the wave propagation direction which could change the observed right- or left-handed ellipticity of the wave field. Extreme Doppler shift effects may also be able to change the sign of ellipticity. If ongoing work regarding the wave propagation direction and Doppler shift effects is unable to explain the quasi-parallel right-handed wave observations, then we may need to expand our expectations of ion scale waves to include low frequency Whistler waves.

During times when there is no KH activity, the magnetosphere is dominated by quasi-parallel propagating EMIC and/or KA waves. The magnetosheath is dominated by quasi-perpendicular KM waves when the KHI is not active. In contrast, the magnetosphere is dominated by the quasi-perpendicular KM wave mode and the sheath by the quasi-parallel EMIC and/or KA wave modes when the KHI is active. The increased presence of KA waves, which are known to effectively heat ions, in the sheath during KHI may contribute to enhanced heating across the magnetopause boundary. The preferential observation of perpendicular (parallel) propagating waves in the magnetosphere (magnetosheath) during active KHI is consistent with previous work done by *Moore et al.* [2017] using Cluster data.

Poynting flux is enhanced in all regions and at all wave angles during the KHI, which suggests more energy is available to drive heating. Observations of the char-

acteristic heating frequency suggest that waves associated with the KHI are able to more efficiently heat plasma than waves observed when there is no active KHI. This is further supported by the change in energy across wave intervals. Wave intervals associated with the KHI tend to show greater increases in average energy than those wave intervals associated with non-KH observations. The increased change in energy is also well correlated with increased Poynting flux in the magnetosphere and magnetosheath. These results are consistent with the findings of *Moore et al.* [2017].

Ion temperature anisotropy is increased in the magnetosheath during active KHI. This anisotropy may be responsible for the driving of EMIC waves in the sheath. Additionally, electron beta is decreased by approximately an order of magnitude in the magnetosheath during active KH. The decreased  $\beta_e$  allows the plasma to support KA waves which would not be supported when the KHI is not present and beta is nearer to 1. Again, these findings are consistent with *Moore et al.* [2017].

Velocity shears parallel to the background magnetic field are consistently higher during the KHI observations than in non-KH observations. Increased shears occur in both the magnetosphere and magnetosheath and may be responsible for the enhanced perpendicular (parallel) wave activity in the magnetosphere (magnetosheath). As KHI may only develop in regions of large velocity shear, it is possible the observed velocity shears existed prior to the development of the KHI.

The results of this Chapter should be considered preliminary pending a full analysis of the Doppler shift effects as discussed in Section 2.2.2.

# Chapter 5

## Summary and Discussion

### 5.1 Summary

The main results of this dissertation may be summarized as follows:

- MMS observed 45 KH events between September 2015 and March 2020.
- The observed KHI were well distributed along the magnetopause. More observations of the KHI were made along the dusk flank than the dawn flank, likely due to the apogee raising maneuvers used to transition the MMS orbit from Phase 1 to Phase 2 which took place on the dawn flank. Observations were evenly distributed on either side of the day-night terminator.
- MMS observed a cluster of nine KHI events at high southern magnetic latitude (GSM  $Z \leq -4.5 R_E$ ). Such high latitude KHI observations have been rare prior to the launch of MMS.
- A new automated region sorting technique was developed to isolate regions



of pure magnetosheath and magnetospheric plasma within observations of the KHI. The method was compared with a previous technique used in *Moore et al.* [2017] and with MHD simulations. The new technique is apparently robust and reliable.

- KHI growth rates, unitless growth rates, and unstable solid angles are consistently larger along the tail magnetopause than on the dayside.
- Observations of the KHI were made for the full range of solar wind conditions and IMF orientations. An apparent selection window in solar wind flow speed between 295 km/s and 610 km/s is likely insignificant and merely a reflection of the distribution of solar wind speeds for the full 4.5 year interval from September 2015 to March 2020. More observations of the KHI were made when the  $B_Z$  component of the IMF was northward than southward.
- KHI growth rates, unitless growth rates, and unstable solid angles are independent of solar wind conditions and IMF magnitude.
- Observations of ion scale wave intervals during the KHI are consistent with ion cyclotron, kinetic Alfvén, and kinetic magnetosonic wave modes. Normalized wave field ratios,  $\delta E/\delta B$ , indicate the observed wave intervals are electromagnetic.
- During KHI observations ion scale wave intervals in the magnetosphere are dominated by quasi-perpendicular waves and the magnetosheath is dominated by quasi-parallel waves. This is a reversal of the pattern of observations when the KHI is not active. Our observations of ion scale wave activity are consistent

with findings from *Moore et al.* [2017].

- During KHI observations Poynting flux within ion scale wave intervals is enhanced for all regions and all wave angles, suggesting there is more energy available for ion heating when the KHI is active.
- Characteristic heating frequency is larger in KH associated wave intervals than in non-KH associated wave intervals. This indicates the KH associated waves are able to more efficiently heat plasma than the waves which develop when the KHI is not active.
- The change in energy across wave intervals is larger for KH associated wave intervals than for non-KH intervals. Additionally, the increased change in energy is well correlated with increased Poynting flux in the magnetosphere and magnetosheath, consistent with results from *Moore et al.* [2017].
- Electron beta is decreased in the magnetosheath when KH waves are present. The observed decreases in electron beta can help explain the increased observation of parallel and quasi-parallel propagating waves within the sheath during the KHI, as low beta plasma is able to support kinetic Alfvén waves which propagate quasi-parallel to the background field.
- Temperature anisotropy is increased in the magnetosheath when KH waves are present. Larger anisotropies can help explain the increased observation of parallel and quasi-parallel propagating waves within the sheath during the KHI, as they are capable of driving quasi-parallel propagating EMIC waves.
- The change in parallel velocity between MMS spacecraft pairs is consistently

larger during observations of the KHI. This increased shear in all regions may help drive ion scale wave activity and heating.

## 5.2 Discussion

The MMS observations of the KHI reported in this dissertation are consistent with those made using THEMIS, Cluster, and Geotail data [*Kavosi and Reader, 2015; Moore et al., 2017; Hasegawa et al., 2006*]. The identification of KHI within MMS data is a vital first step in the process of determining the KHI's contribution to heating and plasma transport across scale sizes. The identification of the KHI at high southern magnetic latitudes is a new finding as previous in-situ magnetospheric investigations were limited to more equatorial orbits when observing the magnetopause flanks where the KHI is likely to develop. The high latitude cases offer an excellent opportunity to study the ways in which the KHI may effect the dynamics of the magnetospheric cusps [*Nykyri et al., 2019, 2021b*].

The fluid scale properties of the KHI presented in Chapter 3 are consistent with previous works and our theoretical understanding of the KHI. The KHI observations are well distributed along the magnetopause. Though more events are observed on the dusk flank than the dawn flank, this is likely a product of the MMS orbit, and does not immediately contradict the expectations set by *Henry et al. [2017]*. KHI growth rates and unstable solid angles increase with distance downtail, which is consistent with magnetosheath plasma accelerating along the flanks to re-achieve solar wind speed after the bow shock [*Dimmock and Nykyri, 2013; Dimmock et al., 2015*]. The KHI growth rates and unstable solid angles are uncorrelated with solar wind conditions,

which is not surprising as the KHI is often observed downstream of its source region.

The automated region sorting method developed in Chapter 2 is perhaps the most significant contribution of this dissertation. The new method reliably selects the pure magnetosheath and magnetospheric regions, even for highly mixed boundary crossings which were not well sorted using previous methods [Moore *et al.*, 2017]. The new method performs well for both real satellite data and simulations. The new method may be applied to all types of boundary crossings, not just those when the KHI is active, to isolate regions of pure magnetosheath and magnetospheric plasma.

The ion scale wave analysis of KHI events in the MMS data is in agreement with previous studies of Cluster observations. We were able to identify a likely kinetic magnetosonic wave within the KH vortex observed on 26 September 2017, similar to the kinetic magnetosonic wave packet described by Moore *et al.* [2016]. The statistical study of MMS KHI observations showed increased perpendicular (parallel) wave activity in the magnetosphere (magnetosheath) at times when the KHI is active, consistent with the results of Moore *et al.* [2017]. Poynting flux is larger in KHI associated wave intervals in all regions, suggesting more energy is available to drive ion scale heating when the KHI is active. We also see greater changes in average energy across the wave intervals associated with the KHI, which is well correlated with the increased Poynting flux. Characteristic heating frequency also increases when the KHI is active, suggesting the KH driven ion scale waves are able to energize the plasma more efficiently than similar waves developing when the KHI is not active.

We believe increased temperature anisotropies and decreased electron beta in the sheath during observations of the KHI may be a driving mechanism for the observed mostly parallel and quasi-parallel wave activity in the sheath, as both electromagnetic

ion cyclotron and kinetic Alfvén waves can propagate at small angles with respect to the background field. Additionally, increased parallel velocity shears associated with the KHI can drive ion scale waves in all regions, though it is unclear if such shears are a result of the KHI or a precursor to its development.

Having found the results of the new MMS dataset consistent with the literature, it is now reasonable and necessary to extend the search for KHI associated small scale waves below the ion scale. Additional work may also strengthen the results and conclusions presented here, as described in the next section.

### 5.3 Ongoing and Future Work

Though we are generally satisfied with the performance of the automated region sorting method developed in Chapter 2, it is worthwhile to compare it to data from the wave analysis instruments aboard MMS (SCM and EDP). Studies at Jupiter’s magnetopause have shown clear signatures in the high frequency field data which can be used to distinguish magnetosheath and magnetospheric plasmas. Similar work may be possible at Earth’s magnetopause and could be used to supplement the region sorting method presented in Chapter 2.

We note the results of the ion scale wave study presented in Chapter 4 are preliminary pending a detailed analysis of the Doppler shift effects on the frequency and ellipticity of the observed wave intervals. There is a possibility that Doppler shifts are large enough to change the observed left- or right-handed nature of the wave field. This analysis should be particularly illuminating for the set of right-handed quasi-parallel wave intervals in the magnetosheath during KHI observations,

the magnetosphere during non-KH observations, and the mixed regions during both KHI and non-KH observations. These waves are not obviously consistent with any of the ion cyclotron, kinetic Alfvén, or kinetic magnetosonic wave modes, though theoretical work suggests the kinetic Alfvén wave may become right-handed for large plasma beta [*Krauss-Varban et al.*, 1994]. If the Doppler shift is sufficient to change the sign of the ellipticity, however, they would be consistent with the EMIC or KA wave modes. If the ellipticity remains positive after Doppler shifts are applied, then these intervals may instead contain low frequency Whistler waves. In either case, the determination of Doppler shift effects will provide greater insight to the array of ion scale wave modes present in the KHI.

Additionally, the analysis of energy changes within well polarized wave intervals does not currently account for the typical energies in their region of observation. We expect some energy change across ion scale intervals, even if they do not contain well polarized waves. Work to determine what the typical energy change across intervals which do not contain waves is ongoing. Results presented in Section 4.4.6 may then be normalized to better understand the effects of the ion scale waves independently of background trends.

The effect of reconnection on ion scale wave modes within the KHI remains a compelling open question. Future work may use the Walén relation to identify well polarized wave intervals associated with reconnection. Reconnection is a known driver of ion scale waves, like the ion cyclotron and kinetic magnetosonic waves considered here. A comparison of wave activity associated with reconnection in the KHI with waves generated independently of reconnection could provide new insight to the KHI's ability to drive heating into the magnetosphere. Though a few case studies have

identified specific sub-ion wave modes related to reconnection in the KHI [*Wilder et al.*, 2016; *Stawarz et al.*, 2016], the overall influence of reconnection on sub-ion scale waves associated with the KHI remains an open question.

The techniques developed and applied in this dissertation can be applied to wave intervals at smaller scales. MMS burst mode data is capable of resolving electron scale waves and processes. Burst mode data is available for portions of all the KHI events presented in this dissertation, totaling over 29 hours of burst data across all 45 events. This burst data is necessary for the extension of the present work to sub-ion scale wave modes. Preliminary results at hybrid scales are already promising. Using the techniques described here, a wave interval consistent with the lower hybrid drift instability was found in the example KHI event on 26 September 2017. Figure 5.1 shows burst mode electric and magnetic field data between 17:54 and 17:55 UT with a clear wave packet in the field filtered around the lower hybrid frequency.

While the search for sub-ion scale wave modes within the KHI should be straight forward, the comparison of those wave modes with non-KH observations may prove challenging. Burst mode data, which is necessary to resolve sub-ion scale processes, is less commonly available in the quiet crossing observations: just under 9 hours of burst data are available from all quiet crossings used in this study. Quiet magnetopause crossings do not usually trigger the typical thresholds for burst mode data collection. Even when burst mode data is collected around a quiet crossing, it is not often prioritized by the SITL for download from the satellite. A secondary search for quiet crossings will be necessary to build a non-KH burst mode database closer to parity with the KHI observations.

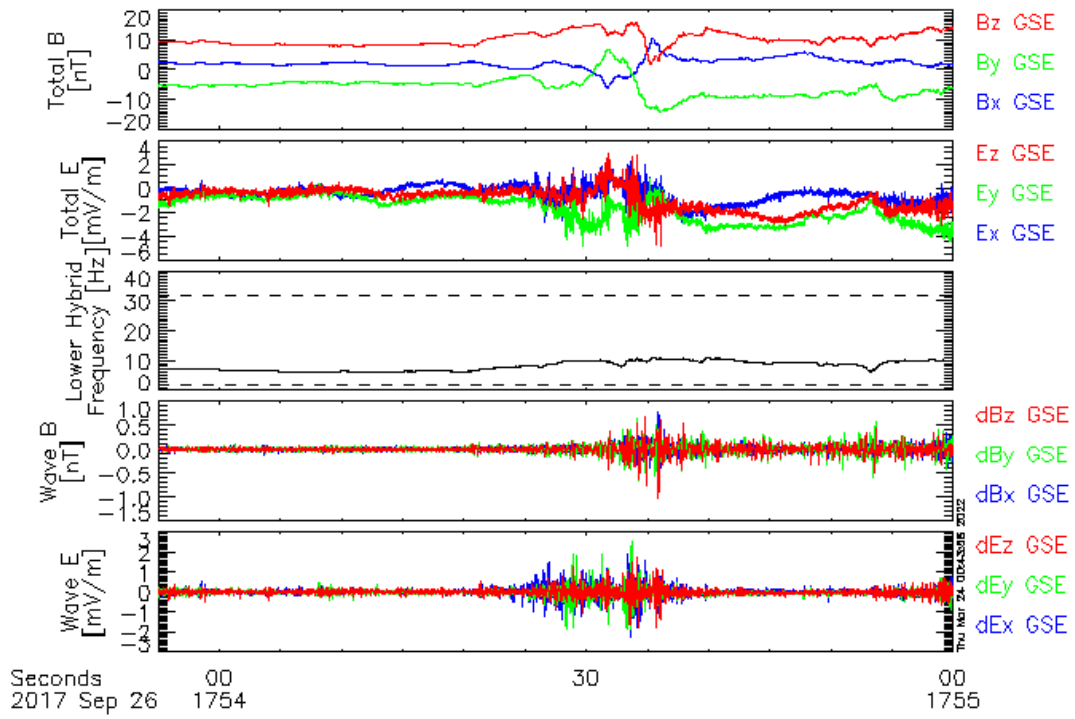


Figure 5.1: The total magnetic and electric fields, the lower hybrid frequency and band pass filter cutoff frequencies, and the filtered magnetic and electric fields show a clear wave packet around the lower hybrid frequency between 17:54 and 17:55 UT on 26 September 2017.



# Appendix A

## Solar Wind Conditions

Solar wind data is retrieved from the OMNIWeb database, maintained by NASA Goddard's Space Physics Data Facility. Data reported in the following tables is convected to the bow shock nose. An estimate of convection time to the KHI observation location was made using the local magnetosheath speed as observed by MMS. Delay times from the bow shock nose to the KHI location are small, typically between 2 and 10 minutes. Even in cases with the most extreme delays from the bow shock nose to the observation point, there is no significant difference in the average solar wind conditions or IMF orientation. For that reason, the bow shock nose shifted values available directly from OMNI are used in this dissertation and presented here. Table A.1 details the onset and average IMF orientations and magnitudes for the KHI events listed in Chapter 2. Table A.2 lists the average solar wind density, temperature, flow speed, and Alfvén mach number during the KHI observations.

Table A.1: The onset IMF orientation and magnitude and average IMF orientation and magnitude of the 45 KHI events observed by MMS from September 2015 to March 2020. OMNI data is not available for the event on 03 June 2019 (event no. 37).

Event No.	Onset IMF [nT]				Average IMF [nT]			
	GSM X	GSM Y	GSM Z	Mag.	GSM X	GSM Y	GSM Z	Mag.
01	13.42	3.75	15.79	21.06	12.59	6.15	15.42	20.84
02	-1.13	5.49	0.18	5.61	-1.31	3.13	2.19	4.04
03	-2.45	3.35	-1.14	4.30	-1.45	2.53	-2.10	3.59
04	-2.18	4.87	1.68	5.59	-0.45	5.26	-1.95	5.62
05	-3.40	4.65	1.30	5.91	-3.22	4.57	0.25	5.60
06	-3.29	0.76	-4.79	5.86	-2.98	1.31	-1.65	3.65
07	-1.97	-4.10	-5.35	7.02	2.62	-2.94	-0.74	4.01
08	0.06	-9.46	-3.30	10.02	0.42	-9.09	-4.05	9.96
09	9.21	4.64	4.17	11.12	6.98	5.57	6.24	10.89
10	-2.62	2.41	-3.41	4.93	-2.37	2.86	-2.56	4.51
11	-0.61	3.65	2.66	4.56	1.03	2.66	3.64	4.62
12	3.27	-2.25	-1.11	4.12	2.88	-2.74	0.32	3.99
13	-8.32	-4.13	2.69	9.67	-8.07	-3.81	3.26	9.50
14	-6.37	5.65	-2.36	8.84	-2.87	6.81	-4.79	8.80
15	-4.44	5.12	8.42	10.81	-5.76	1.06	8.82	10.59
16	-4.21	3.80	-2.99	6.41	-4.45	2.56	-0.23	5.13
17	-0.69	5.28	-2.65	5.95	-1.91	5.44	-2.46	6.27
18	-6.14	1.42	0.32	6.31	-5.89	1.86	-1.44	6.35

Continued on next page

Table A.1: Continued from previous page

Event No.	Onset IMF [nT]				Average IMF [nT]			
	GSM X	GSM Y	GSM Z	Mag.	GSM X	GSM Y	GSM Z	Mag.
19	-2.55	3.96	1.56	4.96	-2.60	3.42	2.34	4.89
20	-1.89	1.58	1.04	2.67	-2.05	1.35	1.15	2.71
21	0.28	3.35	2.85	4.41	1.80	1.76	3.35	4.19
22	-1.70	8.11	1.61	8.44	0.83	6.51	4.02	7.69
23	6.67	1.51	5.72	8.92	6.71	0.91	5.70	8.85
24	4.20	-5.12	1.15	6.72	4.42	-4.55	-2.25	6.73
25	6.51	-1.66	-2.10	7.04	6.40	-4.58	-1.79	8.07
26	-3.47	0.60	2.61	4.38	-3.48	0.31	2.10	4.08
27	0.33	-2.65	1.07	2.88	1.02	-1.73	1.56	2.54
28	-1.05	2.71	-0.29	2.92	-0.90	1.91	-0.50	2.17
29	-1.39	0.96	-0.10	1.69	-1.34	0.96	-0.09	1.65
30	0.47	-9.99	3.88	10.73	2.41	-7.16	5.59	9.40
31	-0.72	3.29	3.87	5.13	0.63	0.56	3.55	3.65
32	1.53	1.34	3.32	3.89	-0.19	-1.91	2.38	3.06
33	-3.60	0.86	2.24	14.33	-0.92	-1.88	1.24	2.43
34	-2.57	2.06	-0.22	3.30	-1.85	2.52	0.30	3.14
35	2.76	-1.31	1.00	3.21	2.08	-0.95	0.00	2.29
36	0.28	-1.23	-0.72	1.45	-1.50	-2.00	-0.31	2.52
37	NaN	NaN	NaN	NaN	NaN	NaN	NaN	NaN
38	2.26	-3.84	1.74	4.78	0.48	-3.45	0.25	3.50

Continued on next page

Table A.1: Continued from previous page

Event No.	Onset IMF [nT]				Average IMF [nT]			
	GSM X	GSM Y	GSM Z	Mag.	GSM X	GSM Y	GSM Z	Mag.
39	-4.57	2.38	-0.70	5.36	-4.27	1.82	-0.63	4.68
40	-3.98	0.21	1.57	4.28	-3.59	-0.61	2.12	4.22
41	-2.88	3.67	-0.62	4.71	-3.16	3.74	0.21	4.90
42	-1.76	1.18	-1.32	2.50	-1.26	1.80	-0.76	2.32
43	-0.91	-5.81	2.98	6.59	-1.22	-5.05	4.91	7.14
44	0.65	-2.82	0.59	2.95	0.55	-2.75	0.47	2.84
45	0.22	-4.55	5.82	7.39	0.21	-4.39	5.72	7.21

Table A.2: The average solar wind density, temperature, flow speed and Alfvén mach number during 45 KHI events observed by MMS from September 2015 to March 2020. OMNI data is not available for the event on 03 June 2019 (event no. 37).

Event No.	Density [/cc]	Temperature [eV]	Flow Speed [km/s]	Alfvén Mach No.
01	9.91	2.20	509.90	3.80
02	4.67	13.83	520.75	9.96
03	3.15	5.10	475.53	10.92
04	-3.46	6.47	483.63	7.42
05	14.48	3.73	346.20	11.32
06	5.03	11.81	451.94	10.27
07	5.42	7.12	426.18	7.37
08	2.59	61.49	583.90	4.67

Continued on next page

Table A.2: Continued from previous page

Event No.	Density [ $\text{/cc}$ ]	Temperature [eV]	Flow Speed [km/s]	Alfvén Mach No.
09	17.69	2.25	349.38	6.32
10	3.92	5.76	469.50	9.35
11	7.81	3.47	406.22	11.58
12	2.91	14.18	593.17	10.22
13	16.81	4.22	300.93	6.39
14	8.76	5.91	429.57	6.88
15	8.63	16.87	599.39	8.01
16	5.62	14.92	532.97	9.60
17	11.91	3.34	354.66	9.15
18	10.87	4.97	366.43	9.34
19	5.74	4.44	370.79	8.33
20	4.84	5.40	415.65	16.33
21	9.77	2.72	381.81	14.00
22	9.96	0.74	361.43	6.77
23	5.35	1.25	376.45	4.92
24	4.33	26.67	607.60	7.73
25	5.54	31.25	610.03	8.26
26	6.47	9.66	435.11	12.48
27	10.46	1.52	315.23	16.04
28	2.81	9.69	538.75	20.45

Continued on next page

Table A.2: Continued from previous page

Event No.	Density [/cc]	Temperature [eV]	Flow Speed [km/s]	Alfvén Mach No.
29	9.41	1.32	298.20	26.19
30	12.05	10.70	383.10	6.22
31	6.76	3.53	372.11	11.19
32	3.12	6.33	488.72	9.74
33	13.73	3.97	436.06	26.32
34	3.26	4.20	430.89	12.05
35	8.21	4.31	395.93	17.27
36	2.86	7.90	430.74	13.28
37	NaN	NaN	NaN	NaN
38	4.79	3.56	390.84	10.26
39	2.91	7.18	464.83	7.90
40	2.99	10.07	471.40	9.63
41	3.19	8.95	470.39	8.47
42	2.64	2.91	381.95	13.16
43	8.37	2.20	354.53	7.04
44	5.71	3.32	349.64	13.87
45	3.23	4.82	312.64	3.88

# Appendix B

## Non-KH Observation Details

The KHI observations in this dissertation are compared with magnetopause boundary crossings in which MMS does not observe any of the signatures of the KHI. The date, onset time, duration, and average location of these “quiet” crossings are listed in Table B.1. As discussed in Chapter 4 the total observation time of KHI and non-KH crossings is similar. The dawn and dusk distribution of the KHI and non-KH observations is also very similar. There is a significant discrepancy, however, in the distribution non-KH observations on either side of the day-night terminator. Of the 66 hrs 53 mins of KH observation, 44 hours and 3 minutes occur along the tail magnetopause. Only 45 minutes of the 66 hours and 20 minutes of non-KH observations take place in the tail. The tail magnetopause is not as stable as the dayside magnetopause, and many transient process and surface mode waves are often active along the tail. Thus, finding crossings which exhibit *none* of the signatures of the KHI is incredibly difficult.

Table B.1: The date, onset time, duration, and GSM location of 33 quiet magnetopause crossings observed by MMS from September 2015 to March 2020.

Event No.	Date	Onset Time UT	Duration [min]	GSM Location [ $R_E$ ]
01	18 Sep 15	07:00	180	[6.3, 6.0, -3.5]
02	21 Sep 15	10:00	90	[6.4, 7.5, -5.0]
03	21 Sep 15	12:00	60	[6.0, 8.4, -5.6]
04	24 Oct 15	04:10	120	[9.4, 2.7, -1.4]
05	29 Oct 15	04:00	120	[9.8, 2.3, -1.3]
06	02 Nov 15	03:10	120	[9.7, 1.5, -0.9]
07	30 Nov 15	23:55	125	[9.4, -2.9, -0.6]
08	30 Oct 16	13:00	180	[6.9, 8.7, -3.8]
09	02 Nov 16	14:00	120	[7.1, 8.9, -3.4]
10	03 Nov 16	14:00	120	[7.2, 8.9, -3.3]
11	08 Nov 16	08:30	150	[8.4, 5.1, -3.1]
12	16 Nov 16	15:00	75	[8.2, 8.3, -1.8]
13	28 Nov 16	17:30	30	[7.4, 7.4, 0.4]
14	04 Feb 17	22:30	50	[6.4, -6.9, -3.3]
15	09 Feb 17	08:45	120	[9.2, -4.2, 1.6]
16	14 Nov 17	14:00	120	[10.1, 5.9, -0.4]
17	25 Nov 17	20:00	210	[11.2, 4.1, 1.7]
18	28 Nov 17	14:30	210	[10.3, 2.8, 0.9]
19	23 Dec 17	12:00	180	[7.5, 9.0, 2.7]

Continued on next page



Table B.1: Continued from previous page

Event No.	Date	Onset Time UT	Duration [min]	GSM Location [ $R_E$ ]
20	07 Jan 18	01:10	170	[9.3, -4.5, 0.7]
21	20 Jan 18	18:00	120	[9.0, 3.1, 4.3]
22	18 Mar 18	02:20	60	[9.1, -5.8, 0.3]
23	15 May 18	22:00	45	[-2.7, -17.4, -2.0]
24	01 Nov 18	16:00	120	[6.0, 9.9, 1.3]
25	26 Nov 18	23:55	125	[9.1, 5.7, 4.0]
26	16 Dec 18	05:10	30	[4.7, 12.1, 1.2]
27	16 Feb 19	01:00	180	[9.0, -10.0, 1.1]
28	23 Feb 19	01:00	150	[7.2, -10.5, 0.3]
29	05 Apr 19	14:00	120	[9.5, -5.9, -1.8]
30	16 Apr 19	02:30	120	[8.0, -6.5, -3.1]
31	03 Dec 19	18:00	120	[8.6, 5.6, 5.6]
32	31 Dec 19	07:00	120	[4.2, 9.5, -3.3]
33	21 Jan 20	08:00	120	[6.7, 7.3, -2.5]

# Bibliography

- Adamson, E., K. Nykyri, and A. Otto (2016), The Kelvin-Helmholtz instability under Parker-spiral interplanetary magnetic field conditions at the magnetospheric flanks, *Advances in Space Research*, 58.
- Axford, W., and C. Hines (1961), A unifying theory of high-Latitude phenomena and geomagnetic storms, *Canadian Journal of Physics*, 39, 1433–1464.
- Baker, D. N., L. Riesberg, C. K. Pankratz, R. S. Panneton, B. L. Giles, F. D. Wilder, and R. E. Ergun (2016), Magnetospheric multiscale instrument suite operations and data system, *Space Science Reviews*, 199(1), 545–575.
- Bicknell, P. J. (1968), Did anaxagoras observe a sunspot in 467 b.c.?, *Isis*, 59(1), 87–90.
- Birn, J. (1980), Computer studies of the dynamic evolution of the geomagnetic tail, *Journal of Geophysical Research*, 85, 1214–1222.
- Biskamp, D., E. Schwarz, and J. F. Drake (1995), Ion-controlled collisionless magnetic reconnection, *Phys. Rev. Lett.*, 75, 3850–3853, doi:10.1103/PhysRevLett.75.3850.
- Burch, J. L., and J. F. Drake (2009), Reconnecting magnetic fields: The huge amounts of energy released from the relinking of magnetic fields in outer space are both mysterious and potentially destructive, *American Scientist*, 97(5), 392–399.

- Burch, J. L., and T. D. Phan (2016), Magnetic reconnection and the dayside magnetopause: advances with MMS, *Geophysical Research Letters*, *43*, 8327–8338, doi: 10.1002/2016GL069787.
- Burch, J. L., T. E. Moore, R. B. Torbert, and B. L. Giles (2016), Magnetospheric Multiscale overview and science objectives, *Space Science Reviews*, *199*, 5–21, doi: 10.1007/s11214-015-0164-9.
- Burkholder, B. L., K. Nykyri, X. Ma, R. Rice, S. A. Fuselier, K. J. Trattner, K. R. Pritchard, J. L. Burch, and S. M. Petrinec (2020), Magnetospheric multiscale observation of an electron diffusion region at high latitudes, *Geophysical Research Letters*, *47*(15), doi:10.1029/2020GL087268.
- Chandrasekhar, S. (1961), *Hydrodynamic and Hydromagnetic Stability*, Oxford University Press.
- Chaston, C. C., M. Wilber, M. Fujimoto, M. L. Goldstein, M. Acuna, H. Réme, and A. Fazakerley (2007), Mode conversion of anomalous transport in Kelvin-Helmholtz vortices and kinetic Alfvén waves at Earth’s magnetopause, *Physical Review Letters*, *99*.
- Dimmock, A. P., and K. Nykyri (2013), The statistical mapping of magnetosheath plasma properties based on THEMIS measurements in the magnetosheath interplanetary medium reference frame, *Journal of Geophysical Research*, *118*, 4963–4876.
- Dimmock, A. P., K. Nykyri, H. Karimabadi, A. Osmane, and T. I. Pulkkinen (2015), A statistical study into the spatial distribution and dawn-dusk asymmetry of dayside magnetosheath ion temperatures as a function of upstream solar wind conditions, *Journal of Geophysical Research*, *120*, 2767–2782, doi:

10.1002/2014JA020734.

- Drake, J. F., M. Swisdak, T. D. Phan, P. A. Cassak, M. A. Shay, S. T. Lepri, R. P. Lin, E. Quataert, and T. H. Zurbuchen (2009), Ion heating resulting from pickup in magnetic reconnection exhausts, *Journal of Geophysical Research: Space Physics*, *114*(A5), doi:<https://doi.org/10.1029/2008JA013701>.
- Dungey, J. W. (1961), Interplanetary magnetic field and the auroral zones, *Physical Review Letters*, *6*(2).
- Eastman, T., and E. Hones Jr (1979), Characteristics of the magnetospheric boundary layer and magnetopause layer as observed by imp 6, *Journal of Geophysical Research: Space Physics*, *84*(A5), 2019–2028.
- Ergun, R. E., S. Tucker, J. Westfall, K. A. Goodrich, D. M. Malaspina, D. Summers, J. Wallace, M. Karlsson, J. Mack, N. Brennan, B. Pyke, P. Withnell, R. Torbert, J. Macri, D. Rau, I. Dors, J. Needell, P. A. Lindqvist, G. Olsson, and C. M. Cully (2016), The axial double probe and fields signal processing for the mms mission, *Space Science Reviews*, *199*(1), 167–188, doi:[10.1007/s11214-014-0115-x](https://doi.org/10.1007/s11214-014-0115-x).
- Eriksson, S., B. Lavraud, F. D. Wilder, J. E. Stawarz, B. L. Giles, J. L. Burch, W. Baumjohann, R. E. Ergun, P.-A. Lindqvist, W. Magnes, C. J. Pollock, C. R. Russel, Y. Saito, R. J. Strangeway, R. B. Torbert, D. J. Gershmann, Y. V. Khotyaintsev, J. C. Dorelli, S. J. Schwartz, L. Avanov, E. Grimes, Y. Vernisses, A. P. Sturmer, T. D. Phan, G. T. Marklund, T. E. Moore, W. R. Paterson, and K. A. Goodrich (2016), Magnetospheric multiscale observations of magnetic reconnection associated with Kelvin-Helmholtz waves, *Geophysical Research Letters*, *43*, 5606–5615, doi:[10.1002/2016GL068783](https://doi.org/10.1002/2016GL068783).
- Fairfield, D. H., A. Otto, T. Mukai, S. Kokubun, R. P. Lepping, J. T. Steinberg, A. J.

- Lazaurs, and T. Yamamoto (2000), Geotail observations of the Kelvin-Helmholtz instability at the equatorial magnetotail boundary for parallel northward fields, *Journal of Geophysical Research*, 105.
- Foullon, C., C. J. Farrugia, A. N. Fazakerley, C. J. Owen, F. T. Gratton, and R. B. Torbert (2008), Evolution of Kelvin-Helmholtz activity on the dusk flank magnetopause, *Journal of Geophysical Research*, 113, doi:10.1029/2008JA013175.
- Gosling, J. T., M. F. Thomsen, S. J. Bame, and C. T. Russell (1986), Accelerated plasma flows at the near-tail magnetopause, *Journal of Geophysical Research: Space Physics*, 91, doi:10.1029/JA091iA03p03029.
- Hasegawa, A. (1976), Particle acceleration by mhd surface wave and formation of aurora, *Journal of Geophysical Research*, 81(28), 5083–5090.
- Hasegawa, H., M. Fujimoto, K. Maezawa, Y. Saito, and T. Mukai (2003), Geotail observation of the dayside outer boundary region: Interplanetary magnetic field control and dawn-dusk asymmetry, *Journal of Geophysical Research*, 108, doi:10.1029/2002JA009667.
- Hasegawa, H., M. Fujimoto, T.-D. Phan, H. Réme, A. Balogh, M. W. Dunlop, C. Hashimoto, and R. TanDokoro (2004), Transport of solar wind into Earth's magnetosphere through rolled-up Kelvin-Helmholtz vortices, *Nature*, 430, 755–758.
- Hasegawa, H., M. Fujimoto, K. Takagi, Y. Saito, T. Mukai, and H. Réme (2006), Single-spacecraft detection of rolled-up Kelvin-Helmholtz vortices at the flank magnetopause, *Journal of Geophysical Research*, 111, doi:10.1029/2006JA011728.
- Helmholtz, H. (1868), On discontinuous movements of fluids, translated from german by f. guthrie, *Philos. Mag*, 36, 337–346.

- Henry, Z. W., K. Nykyri, T. W. Moore, A. P. Dimmock, and X. Ma (2017), On the dawn-dusk asymmetry of the Kelvin-Helmholtz instability between 2007 and 2013, *Journal of Geophysical Research*, *122*, 11,888–11,900, doi:10.1002/2017JA024548.
- Hwang, K.-J., M. L. Goldstein, M. M. Kuznetsova, Y. Wang, A. F. Viñas, and D. G. Sibeck (2012), The first in situ observation of kelvin-helmholtz waves at high-latitude magnetopause during strongly dawnward interplanetary magnetic field conditions, *Journal of Geophysical Research: Space Physics*, *117*(A8), doi:10.1029/2011JA017256.
- Johnson, J. R., and C. Cheng (2001), Stochastic ion heating at the magnetopause due to kinetic alfvén waves, *Geophysical research letters*, *28*(23), 4421–4424.
- Johnson, J. R., C. Z. Cheng, and P. Song (2001), Signatures of mode conversion and kinetic Alfvén waves at the magnetopause, *Geophysical Research Letters*, *28*.
- Kavosi, S., and J. Reader (2015), Ubiquity of Kelvin-Helmholtz waves at the Earth’s magnetopause, *Nature Communications*.
- Kelvin, L., and W. Thomson (1871), Hydrokinetic solutions and observations, *The London, Edinburgh, and Dublin Philosophical Magazine and Journal of Science*, *42*(281), 362–377.
- Kim, S.-H., E. Agrimson, M. J. Miller, N. D’Angelo, R. L. Merlino, and G. I. Ganguli (2004), Amplification of electrostatic ion-cyclotron waves in a plasma with magnetic-field-aligned ion flow shear and no electron current, *Physics of plasmas*, *11*(9), 4501–4505.
- King, J. H., and N. E. Papitashvili (2005), Solar wind spatial scales in and comparisons of hourly wind and ACE plasma and magnetic field data, *Journal of Geophysical Research*, *110*, doi:10.1029/2004JA010649.

- Krauss-Varban, D., N. Omid, and K. Quest (1994), Mode properties of low-frequency waves: Kinetic theory versus hall-mhd, *Journal of Geophysical Research: Space Physics*, *99*(A4), 5987–6009.
- Le Contel, O., P. Leroy, A. Roux, C. Coillot, D. Alison, A. Bouabdellah, L. Mirioni, L. Meslier, A. Galic, M. C. Vassal, R. B. Torbert, J. Needell, D. Rau, I. Dors, R. E. Ergun, J. Westfall, D. Summers, J. Wallace, W. Magnes, A. Valavanoglou, G. Olsson, M. Chutter, J. Macri, S. Myers, S. Turco, J. Nolin, D. Bodet, K. Rowe, M. Tanguy, and B. de la Porte (2016), The search-coil magnetometer for mms, *Space Science Reviews*, *199*(1), 257–282, doi:10.1007/s11214-014-0096-9.
- Lembege, B., S. Ratliff, J. Dawson, and Y. Ohsawa (1983), Ion heating by strong magnetosonic waves, *Physical Review Letters*, *51*, 264.
- Lin, D., C. Wang, W. Li, B. Tang, X. Guo, and Z. Peng (2014), Properties of Kelvin-Helmholtz waves at the magnetopause under northward interplanetary magnetic field: statistical study, *Journal of Geophysical Research: Space Physics*, *119*, 7485–7494, doi:10.1002/2014JA020379.
- Lindqvist, P. A., G. Olsson, R. B. Torbert, B. King, M. Granoff, D. Rau, G. Needell, S. Turco, I. Dors, P. Beckman, J. Macri, C. Frost, J. Salwen, A. Eriksson, L. Åhlén, Y. V. Khotyaintsev, J. Porter, K. Lappalainen, R. E. Ergun, W. Vermeer, and S. Tucker (2016), The spin-plane double probe electric field instrument for mms, *Space Science Reviews*, *199*(1), 137–165, doi:10.1007/s11214-014-0116-9.
- Ma, X., A. Otto, and P. Delamere (2014a), Interaction of magnetic reconnection and Kelvin-Helmholtz modes for large magnetic shear: 1. Kelvin-Helmholtz trigger, *Journal of Geophysical Research: Space Physics*, *119*, 781–797, doi:10.1002/2013JA019224.

- Ma, X., A. Otto, and P. Delamere (2014b), Interaction of magnetic reconnection and Kelvin-Helmholtz modes for large magnetic shear: 2. reconnection trigger, *Journal of Geophysical Research: Space Physics*, *119*, 808–820, doi:10.1002/2013JA019225.
- Ma, X., A. Otto, P. A. Delamere, and H. Zhang (2016), Interaction between reconnection and Kelvin-Helmholtz at the high-latitude magnetopause, *Advances in Space Research*, *58*(2), 231–239.
- Ma, X., P. Delamere, A. Otto, and B. Burkholder (2017), Plasma transport driven by the three-dimensional Kelvin-Helmholtz instability, *Journal of Geophysical Research: Space Physics*, *122*, 10,382–10,395, doi:10.1002/2017JA024394.
- Ma, X., P. Delamere, K. Nykyri, B. Burkholder, D. Neupane, and R. Rice (2019), Comparison between fluid simulation with test particles and hybrid simulation for the Kelvin-Helmholtz instability, *Journal of Geophysical Research: Space Physics*, *124*, 6654–6668, doi:10.1029/2019JA026890.
- Mann, I. R., A. N. Wright, K. J. Mills, and V. M. Nakariakov (1999), Excitation of magnetospheric waveguide modes by magnetosheath flows, *Journal of Geophysical Research: Space Physics*, *104*(A1), 333–353, doi: <https://doi.org/10.1029/1998JA900026>.
- Merkin, V. G., J. G. Lyon, and S. G. Claudepierre (2013), Kelvin-Helmholtz instability of the magnetospheric boundary in a three-dimensional global MHD simulation during northward IMF conditions, *Journal of Geophysical Research: Space Physics*, *118*, 5478–5496, doi:10.1002/jgra.50520.
- Michael, A. T., K. A. Sorathia, V. G. Merkin, K. Nykyri, B. L. Burkholder, X. Ma, A. Y. Ukhorskiy, and J. Garretson (2021), Modeling Kelvin-Helmholtz Instability at the High-Latitude Boundary Layer in a Global Magnetosphere Simulation,



- Geophysical Research Letters*, 48(19), doi:10.1029/2021GL094002.
- Miura, A. (1984), Anomalous transport by magnetohydrodynamic Kelvin-Helmholtz instabilities in the solar wind-magnetosphere interaction, *Journal of Geophysical Research*, 89, 801–818.
- Miura, A. (1987), Simulation of the Kelvin-Helmholtz instability at the magnetospheric boundary, *Journal of Geophysical Research*, 92, 3195–3206.
- Miura, A., and P. L. Pritchett (1982), Nonlocal stability analysis of the MHD Kelvin-Helmholtz instability in a compressible plasma, *Journal of Geophysical Research*, 87, 7431–7444.
- Moore, T. W., K. Nykyri, and A. P. Dimmock (2016), Cross-scale energy transport in space plasmas, *Nature Physics*.
- Moore, T. W., K. Nykyri, and A. P. Dimmock (2017), Ion-scale wave properties and enhanced ion heating across the low-latitude boundary layer during Kelvin-Helmholtz instability, *Journal of Geophysical Research: Space Physics*, 122, 11,128–11,153, doi:10.1002/2017JA024591.
- Nicholson, D. (1983), *Introduction to Plasma Theory*, Wiley & Sons, New York.
- Nykyri, K. (2013), Impact of MHD shock physics on magnetosheath asymmetry and Kelvin-Helmholtz instability, *Journal of Geophysical Research: Space Physics*, 118, 5068–5081.
- Nykyri, K., and A. Otto (2001), Plasma transport at the magnetopause boundary due to reconnection in Kelvin-Helmholtz vortices, *Geophysical Research Letters*, 28, 3565–3568.
- Nykyri, K., and A. Otto (2004), Influence of the Hall term on KH instability and

- reconnection inside KH vortices, *Annales Geophysicae*, *22*, 935–949.
- Nykyri, K., A. Otto, J. Büchner, B. Nikutowski, W. Baumjohann, L. M. Kistler, and C. Mouikis (2003a), Equator-S observations of boundary signatures: FTE's or Kelvin-Helmholtz waves?, in *Earth's Low-Latitude Boundary Layer, Geophysical Monograph*, vol. 133, edited by P. T. Newell and R. Onsager, pp. 205–210, American Geophysical Union.
- Nykyri, K., P. J. C. E. A. Lucek, T. S. Horbury, A. Balogh, B. Lavraud, I. Dandouras, and H. Reme (2003b), Ion cyclotron waves in the high altitude cusp: CLUSTER observations and varying spacecraft separations, *Geophysical Research Letters*, *30*, doi:10.1029/2003GL018594.
- Nykyri, K., A. Otto, B. Lavraud, C. Mouikis, L. M. Kistler, A. Balogh, and H. Réme (2006a), Cluster observations of reconnection due to the Kelvin-Helmholtz instability at the dawnside magnetospheric flank, *Annales Geophysicae*, *24*, 2619–2643.
- Nykyri, K., B. Grison, P. Cargill, B. Lavraud, E. Lucek, I. Dandouras, A. Balogh, N. Cornilleau-Wehrin, and H. Rème (2006b), Origin of the turbulent spectra in the high-altitude cusp: Cluster spacecraft observations, in *Annales Geophysicae*, vol. 24, pp. 1057–1075, Copernicus GmbH.
- Nykyri, K., X. Ma, A. Dimmock, C. Foullon, A. Otto, and A. Osmane (2017), Influence of velocity fluctuations on the Kelvin-Helmholtz instability and its associated mass transport, *Journal of Geophysical Research*, *122*, 9489–9512, doi: 10.1002/2017JA024374.
- Nykyri, K., C. Chu, X. Ma, S. A. Fuselier, and R. Rice (2019), First mms observation of energetic particles trapped in high-latitude magnetic field depressions, *Journal of Geophysical Research: Space Physics*, *124*(1), 197–210, doi:

- <https://doi.org/10.1029/2018JA026131>.
- Nykyri, K., J. Johnson, E. Kronberg, D. Turner, S. Wing, I. Cohen, K. Sorathia, X. Ma, B. Burkholder, G. Reeves, and J. Fennell (2021a), Magnetospheric multi-scale observations of the source region of energetic electron microinjections along the duskside, high-latitude magnetopause boundary layer, *Geophysical Research Letters*, *48*(9), e2021GL092466, doi:<https://doi.org/10.1029/2021GL092466>.
- Nykyri, K., X. Ma, B. Burkholder, R. Rice, J. R. Johnson, E.-K. Kim, P. Delamere, A. Michael, K. Sorathia, D. Lin, S. Merkin, S. Fuselier, J. Broll, O. Le Contel, D. Gershman, I. Cohen, B. Giles, R. J. Strangeway, C. T. Russell, and J. L. Burch (2021b), MMS observations of the multiscale wave structures and parallel electron heating in the vicinity of the southern exterior cusp, *Journal of Geophysical Research: Space Physics*, *126*(3), doi:10.1029/2019JA027698.
- Nykyri, K., X. Ma, and J. Johnson (2021c), *Cross-Scale Energy Transport in Space Plasmas*, chap. 7, pp. 109–121, American Geophysical Union (AGU), doi:<https://doi.org/10.1002/9781119815624.ch7>.
- Otto, A. (1990), 3D resistive MHD computations of magnetospheric physics, *Computer Physics Communications*, *59*, 185–195.
- Otto, A., and D. H. Fairfield (2000), Kelvin-Helmholtz instability at the magnetotail boundary: MHD simulation and comparison with Geotail observations, *Journal of Geophysical Research*, *105*, 21,175–21,190.
- Parker, E. N. (1957), Sweet’s mechanism for merging magnetic fields in conducting fluids, *Journal of Geophysical Research (1896-1977)*, *62*(4), 509–520, doi:<https://doi.org/10.1029/JZ062i004p00509>.
- Parker, E. N. (1958), Dynamics of the interplanetary gas and magnetic fields., *The*

*Astrophysical Journal*, 128, 664.

Paschmann, G., B. U. Ö. Sonnerup, I. Papamastorakis, G. Haerendel, S. J. Bame, J. R. Asbridge, J. T. Gosling, C. T. Russell, and R. C. Elphric (1979), Plasma acceleration at the Earth's magnetopause: evidence for reconnection, *Nature*, 282, 243–246.

Peñano, J. R., and G. Ganguli (2002), Generation of electromagnetic ion cyclotron waves in the ionosphere by localized transverse dc electric fields, *Journal of Geophysical Research: Space Physics*, 107(A8), SIA 14–1–SIA 14–7, doi: <https://doi.org/10.1029/2001JA000279>.

Petschek, H. E. (1964), 50 magnetic field annihilation, in *AAS-NASA Symposium on the Physics of Solar Flares: Proceedings of a Symposium Held at the Goddard Space Flight Center, Greenbelt, Maryland, October 28-30, 1963*, vol. 50, p. 425, Scientific and Technical Information Division, National Aeronautics and .

Pollock, C., T. Moore, A. Jacques, J. Burch, U. Gliese, Y. Saito, T. Omoto, L. Avanov, A. Barrie, V. Coffey, J. Dorelli, D. Gershman, B. Giles, T. Rosnack, C. Salo, S. Yokota, M. Adrian, C. Aoustin, C. Auletta, S. Aung, V. Bigio, N. Cao, M. Chandler, D. Chornay, K. Christian, G. Clark, G. Collinson, T. Corris, A. D. L. Santos, R. Devlin, T. Diaz, T. Dickerson, C. Dickson, A. Diekmann, F. Diggs, C. Duncan, A. Figueroa-Vinas, C. Firman, M. Freeman, N. Galassi, K. Garcia, G. Goodhart, D. Guererro, J. Hageman, J. Hanley, E. Hemminger, M. Holland, M. Hutchins, T. James, W. Jones, S. Kreisler, J. Kujawaski, V. Lavu, J. Lobell, E. LeCompte, A. Lukemire, E. MacDonald, A. Mariano, T. Mukai, K. Narayanan, Q. Nguyen, M. Onizuka, W. Paterson, S. Persyn, B. Piepgrass, F. Cheey, A. Rager, T. Raghuram, A. Ramil, L. Reichenthal, H. Rodriguez, J. Rouzaud, A. Rucker, Y. Saito,

- M. Samara, J.-A. Sauvaud, D. Schuster, M. Shappirio, K. Shelton, D. Sher, D. Smith, K. Smith, S. Smith, D. Steinfeld, R. Szymkiewicz, K. Tanimoto, J. Taylor, C. Tucker, K. Tull, A. Uhl, J. Vloet, P. Walpole, S. Weidner, D. White, G. Winkert, P.-S. Yeh, and M. Zeuch (2016), Fast plasma investigation for Magnetospheric Multiscale, *Space Science Reviews*, *199*, 331–406, doi:10.1007/s11214-016-0245-4.
- Pollock, C. J., P. Cson-Brandt, J. L. Burch, M. G. Henderson, J. M. Jahn, D. J. McComas, S. B. Mende, D. G. Mitchell, G. D. Reeves, E. E. Scime, R. M. Skoug, M. Thomsen, and P. Valek (2003), The role and contributions of energetic neutral atom (ena) imaging in magnetospheric substorm research, *Space Science Reviews*, *109*(1), 155–182, doi:10.1023/B:SPAC.0000007518.93331.d5.
- Potter, D. (1973), *Computational Physics*, John Wiley and Sons.
- Rice, R. C., K. Nykyri, X. Ma, and B. L. Burkholder (2022), Characteristics of kelvin-helmholtz waves as observed by the mms from september 2015 to march 2020, *Journal of Geophysical Research: Space Physics*, *127*(3), doi:10.1029/2021JA029685.
- Rönmark, K. (1982), Whamp - waves in homogeneous, anisotropic, multicomponent plasmas, *Report 179*, Kiruna Geophysical Institute University of Umeå.
- Russell, C. T., B. J. Anderson, W. Baumjohann, K. R. Bromund, D. Dearborn, D. Fischer, G. Le, H. K. Leinweber, D. Lenema, W. Magnes, J. D. Means, M. B. Moldwin, R. Nakamura, D. Pierce, F. Plaschke, K. M. Rowe, J. A. Slavin, R. J. Strangeway, R. Torbet, C. Hagen, I. Jernej, A. Valavanoglou, and I. Richter (2016), The Magnetospheric Multiscale magnetometers, *Space Science Reviews*, *199*, 189–256, doi:10.1007/s11214-014-0057-3.
- Sakurai, K. (1980), The solar activity in the time of galileo, *Journal for the History*

- of Astronomy*, 11(3), 164–173.
- Sarton, G. (1947), Early observations of sunspots, *Isis*, 37, 69–71.
- Sonnerup, B. U. Ö., and M. Scheible (1998), *Analysis Methods for Multi-Spacecraft Data*, chap. Minimum and Maximum Variance Analysis, pp. 185–220, International Space Science Institute.
- Sonnerup, B. U. Ö., G. Paschmann, I. Papamastorakis, N. Sckopke, G. Haerendel, S. J. Bame, J. R. Asbridge, J. T. Gosling, and C. T. Russell (1981), Evidence for magnetic field reconnection at the Earth’s magnetopause, *Journal of Geophysical Research: Space Physics*, 86, doi:10.1029/JA086iA12p10049.
- Sorathia, K. A., V. G. Merkin, A. Y. Ukhorskiy, R. C. Allen, K. Nykyri, and S. Wing (2019), Solar wind ion entry into the magnetosphere during northward IMF, *Journal of Geophysical Research: Space Physics*, 124, doi:doi.org/10.1029/2019JA026728.
- Stawarz, J. E., S. Eriksson, F. D. Wilder, R. E. Ergun, S. J. Schwartz, A. Pouquet, J. L. Burch, B. L. Giles, Y. Khotyaintsev, O. L. Contel, P.-A. Lindqvist, W. Magnes, C. J. Pollock, C. T. Russell, R. J. Strangeway, R. B. Torbert, L. A. Avanov, J. C. Dorelli, J. P. Eastwood, D. J. Gershman, K. A. Goodrich, D. M. Malaspina, G. T. Marklund, L. Mirioni, and A. P. Sturmer (2016), Observations of turbulence in a Kelvin-Helmholtz event on 8 September 2015 by the Magnetospheric Multiscale mission, *Journal of Geophysical Research*, 121, 11,021–11,034, doi:10.1002/10JA023458.
- Sweet, P. (1958), The neutral point theory of solar flares, *Electromagnetic phenomena in cosmical physics*, 6(1), 123.
- Taylor, M. G. G. T., B. Lavraud, C. P. Escoubet, S. E. Milan, K. Nykyri, M. W.

- Dunlop, J. A. Davies, R. H. W. Friedel, H. Frey, Y. V. Bogdanova, A. Asnes, H. Laasko, P. Trvincek, A. Masson, H. Opgenoorth, C. Vallat, A. N. Fazakerley, A. D. Lahiff, C. J. Owen, F. Pitout, Z. Pu, C. Shen, Q. G. Zong, H. Rme, J. Scudder, and T. L. Zhang (2008), The plasma sheet and boundary layers under northward IMF: a multi-point and multi-instrument perspective, *Advances in Space Research*, *41*, 1619–1629.
- Terasawa, T., and M. Nambu (1989), Ion heating and acceleration by magnetosonic waves via cyclotron subharmonic resonance, *Geophysical research letters*, *16*(5), 357–360.
- Torbert, R. B., H. Vaith, M. Granoff, M. Widholm, J. A. Gaidos, B. H. Briggs, I. G. Dors, M. W. Chutter, J. Macri, M. Argall, D. Bodet, J. Needell, M. B. Steller, W. Baumjohann, R. Nakamura, F. Plaschke, H. Ottacher, J. Hasiba, K. Hofmann, C. A. Kletzing, S. R. Bounds, R. T. Dvorsky, K. Sigsbee, and V. Kooi (2016a), The electron drift instrument for mms, *Space Science Reviews*, *199*(1), 283–305, doi:10.1007/s11214-015-0182-7.
- Torbert, R. B., C. T. Russell, w. Magnes, R. E. Ergun, P.-A. Lindqvist, O. LeContel, H. Vaith, J. Macri, S. Myers, D. Rau, J. Needell, B. King, M. Granoff, M. Chutter, I. Dors, G. Olsson, Y. V. Khotyaintsev, A. Eriksson, C. A. Kletzing, S. Bounds, B. Anderson, W. Baumjohann, M. Steller, K. Bromund, G. Le, R. Nakamura, R. J. Strangeway, H. K. Leinweber, S. Tucker, J. Westfell, D. Fisher, F. Plaschke, J. Porter, and K. Lappalainen (2016b), The FIELDS instrument suite on MMS: scientific objectives, measurements, and data products, *Space Science Reviews*, *199*, 105–135, doi:10.1007/s11214=014-0109-8.
- Wilder, F. D., R. E. Ergun, S. J. Schwartz, D. L. Newman, S. Eriksson, J. E.

- Stawarz, M. V. Goldman, K. A. Goodrich, D. J. Gershman, D. M. Malaspina, J. C. Holmes, A. P. Sturmer, J. L. Burch, R. B. Torbert, P.-A. Lindqvist, G. T. Marklund, Y. Khotyaintsev, R. J. Strangeway, C. T. Russel, C. J. Pollock, B. L. Giles, J. C. Dorelli, L. A. Avanov, W. R. Patterson, F. Plaschke, and W. Magnes (2016), Observations of large-amplitude, parallel, electrostatic waves associated with the Kelvin-Helmholtz instability by the Magnetospheric Multiscale mission, *Geophysical Research Letters*, *43*, 8859–8866, doi:10.1002/2016GL070404.
- Wing, S., J. R. Johnson, P. T. Newell, and C.-I. Meng (2005), Dawn-dusk asymmetries, ion spectra, and sources in the northward interplanetary magnetic field plasma sheet, *Journal of Geophysical Research*, *110*, doi:10.1029//2005JA011086.
- Young, D. T., J. L. Burch, R. G. Gomez, A. De Los Santos, G. P. Miller, P. Wilson, N. Paschalidis, S. A. Fuselier, K. Pickens, E. Hertzberg, C. J. Pollock, J. Scherrer, P. B. Wood, E. T. Donald, D. Aaron, J. Furman, D. George, R. S. Gurnee, R. S. Hourani, A. Jacques, T. Johnson, T. Orr, K. S. Pan, S. Persyn, S. Pope, J. Roberts, M. R. Stokes, K. J. Trattner, and J. M. Webster (2016), Hot plasma composition analyzer for the magnetospheric multiscale mission, *Space Science Reviews*, *199*(1), 407–470, doi:10.1007/s11214-014-0119-6.
- Zhang, J., V. N. Coffey, M. O. Chandler, S. A. Boardsen, A. A. Saikin, E. M. Mello, C. T. Russell, R. B. Torbert, S. A. Fuselier, B. L. Giles, et al. (2017), Properties, propagation, and excitation of emic waves observed by mms: A case study, *Marshall Space Flight Center Faculty Fellowship Program*, p. 213.
- Zhao, C., C. T. Russell, R. J. Strangeway, S. M. Petrinec, W. R. Paterson, M. Zhou, B. J. Anderson, W. Baumjohann, K. R. Bromund, M. Chutter, D. Fischer, G. Le, R. Nakamura, F. Plaschke, J. A. Slavin, R. B. Torbert, and H. Y.



Wei (2016), Force balance at the magnetopause determined with MMS: application to flux transfer events, *Geophysical Research Letters*, 43, 11,941–11,947, doi: 10.1002/2016GL071568.